Numerical Investigation of The 2D Vortex Whip

Khang D. Nguyen

A dissertation
submitted in partial fulfillment of the
requirements for the degree of

Doctor of Philosophy

University of Washington

2021

Reading Committee:

Robert Breidenthal, Chair

Jason Detwiler

Mo Li

Program Authorized to Offer Degree:
Department of Physics

University of Washington

Abstract

Numerical Investigation of The 2D Vortex Whip

Khang D. Nguyen

Chair of the Supervisory Committee:
Professor Robert Breidenthal
Department of Aeronautics and Astronautics

The concept of a “vortex whip” refers to an idea to improve the performance of vortex generators in inhibiting boundary layer separation. If fluid separation from the surface of a body can be delayed, it is possible to reduce the drag on the body. To implement a vortex whip, an array of vortices of progressively decreasing strengths is set up, all initially the same distance above a flat surface. The strongest vortex induces the next weaker one toward the surface, and it induces the next weakest one even closer to the surface. If all the vortices originated at the edge of the boundary layer, then they would tend to carry high-momentum fluid toward the surface, thereby inhibiting separation.

This thesis reports on numerical investigations into the 2D vortex whip problem. Code was written to calculate the vortex trajectories of an array of three vortices of progressively decreasing strengths under potential flow conditions. Calculating these vortex trajectories will be key to answering deeper and more interesting questions about vortex whip dynamics. The significance of this project and the fundamental physics studied has important implications for controlling drag and airflow separation, with direct applications to improving lift of aircraft and turbine power output. Over 25000 simulations of different configurations of the 2D vortex whip were performed. This intensive study led to several profound discoveries, paving the way for future work into the vortex whip and its applications in fluid mechanics.

TABLE OF CONTENTS

LIST OF FIGURES

LIST OF TABLES

Table Number Page

GLOSSARY

AOA: Angle of attack

BB: Baby Bear

CCW: Counter-clockwise

CFD: Computational fluid dynamics

CW: Clockwise

DNS: Direct numerical simulation

DO: Direct optimization

FD: Finite difference

FDM: Finite difference method

FEM: Finite element method

FVM: Finite volume method

LES: Large-eddy simulation

LHS: Left-hand side

MB: Mama Bear

PB: Papa Bear

PDE: Partial differential equation

RHS: Ride-hand side

RSM: Response Surface Methodology

SOR: Sense of rotation

VG: Vortex generator

ACKNOWLEDGMENTS

What an incredible journey it has been. I would not be here today without the support of so many individuals, and I would like to express all my gratitude and appreciation for these special people in the following pages. Words cannot fully express how much you all have made a difference in my life. If you are reading this, I bow my head with utmost respect and thank you from the bottom of my heart.

The first person I would like to express my sincere thanks to is my advisor, Bob. I appreciate all of the discussions we had. You have been such an invaluable source of knowledge and support. You have also set a high bar for me to aim for in the field of fluid mechanics, one I am always in awe of when I look at you. For me, the most important difference you made in my graduate studies was simply this: you believed in me. Thank you for having faith in me and going to bat for me when it mattered. I am forever indebted to your generosity and mentorship.

Next I would like to thank the members of my committee: Mo, Jason, Silas, and Jessica. Mo, thank you for agreeing to be my faculty mentor and overseeing the final years of my graduate studies. I would not be able to pursue research in fluid mechanics without your supervision. Silas, thank you for being the nice person that you are, for serving on my committee, and for giving me feedback on my work. And Jessica, I just want to let you know that you are my savior. Without hesitation, you stepped in and happily filled the GSR role on my committee so that I can move forward. Having a supportive person like you on my committee has been one of the blessings of my graduate life.

Jason, words truly cannot express how much I appreciate you for everything you have done for me. There is no doubt that you are one of the reasons why I am here today. Thank you for taking a chance on a college graduate with no programming experience whatsoever. Thank you for teaching me how to program. Thank you for all of your advice and guidance. Thank you for giving it to me straight. And thank you for sticking around all these years. You are the best mentor any student could ask for.

One of the nice things about working with others is that you can bounce ideas off of one another and help each other out when you are stuck. I would like to thank all of the members of my research lab for making me feel welcome and helping me with my research problems. Special thanks to Giovanni and Janna for their help with my CFD questions!

I would like to thank the teachers I have had the pleasure of working with as their TA. Special thanks to David Pengra, who is another great mentor a lucky guy like me had the honor of learning from. David, you are one of the most passionate teachers that I have met. You truly care about teaching, but more importantly, you truly care about the students. Thank you for all of your help throughout the years. Another person I would like to spotlight is Amal al-Wahish. Thank you, Amal, for all of the times you advocated for me. It was my pleasure to serve as your TA! You serve as a role model for how all professors should be.

Along the same line, I want to express my appreciation for the physics department for supporting my education all of these years. I have learned and grown so much from teaching.

A special thank you to Sheh Lit for all of his help, support, and time. I appreciate all the times you have been there for me.

My life outside of physics was enriched these past years by several amazing people (and organizations) I would like to acknowledge. A special thank you to Cheryl, Nasrin, Paul, Michelle, and the other wonderful staff from the KAUST program. Thank you for giving me the opportunity to teach and work with so many talented high school students! A place in my heart is also reserved for the amazing staff at UW STEMsub, including Dave, Michael, Jana, Huy, and Helen. Thank you guys for giving me the opportunity to work with the students in so many roles! And thank you for supporting me outside of work with my graduate studies as well.

I want to thank my family for their enduring and patient support. I know it has been a while, but I am ready to close this chapter on school and move ahead with my life. Thank you for taking care of me all of these years. Now it is my turn to take care of you guys.

And last but certainty not least, I want to thank my beautiful wife for her sacrifice, her love, and her support. You truly are my better half. You are my wife...you are my life.

DEDICATION

To my dear family, my incredible wife,
and to everyone out there with a dream.
Don’t believe it when someone tells you it’s a sunken cause.

Chapter 1

INTRODUCTION

The vortex whip is a relatively novel concept that has seen no precedent[1]. Undertaking a research venture into something so original—to uncover the basic physics of its dynamics and how to use that understanding to improve flow control—has been a daunting task, to say the least. How do we know if the answer we eventually stumble upon is correct? What if there is more than one solution? And what does the solution tell us about how to optimize a vortex whip? This is the reality of research. Not knowing the answer and feeling overwhelmed by the gravity of a given problem is not unusual. Fortunately, sometimes there is a reward at the end of the tunnel for those who persevere and push forward. Before I share with you the fruits of my labor investigating the 2D vortex whip, let me begin by laying the foundations on which I started. These foundations helped me design the tools that I needed to better understand how we can use a vortex whip to inhibit boundary layer separation, thereby reducing drag for many types of applications.

This chapter reviews the fundamental equations of fluid motion, defines relevant terms and definitions important to understand the thesis, provides an introduction to boundary layer theory, potential flow theory, and flow control principles, gives an overview of computational fluid dynamics, explains what drag and lift are in more exact terms, describes how vortex generators work, elucidates the motivation behind the research questions that drive this dissertation, and outlines the rest of the thesis. The extent to which I cover each of these topics is far from exhaustive and certainly does not do them justice. It is my hope, however, to give you a glimpse of the beauty of fluid mechanics and how we can apply it to numerically investigate the vortex whip problem.

---

[1] At the time of this writing, the author knew of no notable literature published on the subject.

1.1 Fundamental Equations of Fluid Motion

In classical fluid dynamics, a fluid is generally treated as a continuous, homogeneous substance with no holes—a continuum. The continuum approximation allows us to treat properties of a fluid as continuous functions in space and time. This approximation is valid as long as the size of the system we deal with is large compared to the mean free path of the molecules.

All classical fluid phenomena where the continuum approximation is valid obey the Navier-Stokes equations, the fundamental equations of fluid motion. The Navier-Stokes equations are nothing more than mathematical statements of three physical principles applied to a particular model[2] of a fluid. These three physical principles are:

1. Mass is conserved.
2. Newton's second law, $\mathbf{F} = m\mathbf{a}$.
3. Energy is conserved.

In conservation form[3], the governing equations for an unsteady, three-dimensional, compressible[4], viscous[5] flow are:

Continuity equation

$$\frac{\partial \rho}{\partial t} + \nabla \cdot (\rho \mathbf{V}) = 0 \tag{1.1}$$

---

[2] There are four commonly used models of a fluid: (1) a finite control volume fixed in space with fluid moving through it; (2) a finite control volume moving with the fluid; (3) an infinitesimal fluid element fixed in space with fluid moving through it; and (4) an infinitesimal fluid element moving with the fluid. See Anderson [16] for more details.

[3] The equations of fluid motion can be written in *conservation form* or *nonconservation form*, depending on which model of a fluid the three physical principles of conservation of mass, Newton's second law, and conservation of energy are applied to. See Anderson [16] for more details.

[4] Flows in which variations in density are significant are called **compressible** flows.

[5] **Viscosity** is a fluid property that is a measure of the internal stickiness of the fluid—its internal friction.

Momentum equations

x component:

$$\frac{\partial(\rho u)}{\partial t} + \nabla \cdot (\rho u \mathbf{V}) = -\frac{\partial p}{\partial x} + \frac{\partial \tau_{xx}}{\partial x} + \frac{\partial \tau_{yx}}{\partial y} + \frac{\partial \tau_{zx}}{\partial z} + \rho f_x \tag{1.2}$$

y component:

$$\frac{\partial(\rho v)}{\partial t} + \nabla \cdot (\rho v \mathbf{V}) = -\frac{\partial p}{\partial y} + \frac{\partial \tau_{xy}}{\partial x} + \frac{\partial \tau_{yy}}{\partial y} + \frac{\partial \tau_{zy}}{\partial z} + \rho f_y \tag{1.3}$$

z component:

$$\frac{\partial(\rho w)}{\partial t} + \nabla \cdot (\rho w \mathbf{V}) = -\frac{\partial p}{\partial z} + \frac{\partial \tau_{xz}}{\partial x} + \frac{\partial \tau_{yz}}{\partial y} + \frac{\partial \tau_{zz}}{\partial z} + \rho f_z \tag{1.4}$$

Energy equation

$$\begin{aligned}\frac{\partial}{\partial t}\left[\rho\left(e + \frac{V^2}{2}\right)\right] + \nabla \cdot \left[\rho\left(e + \frac{V^2}{2}\right)\mathbf{V}\right] &= \rho \dot{q} + \frac{\partial}{\partial x}\left(k\frac{\partial T}{\partial x}\right) + \frac{\partial}{\partial y}\left(k\frac{\partial T}{\partial y}\right) \\ &+ \frac{\partial}{\partial z}\left(k\frac{\partial T}{\partial z}\right) - \frac{\partial(up)}{\partial x} - \frac{\partial(vp)}{\partial y} - \frac{\partial(wp)}{\partial z} + \frac{\partial(u\tau_{xx})}{\partial x} \\ &+ \frac{\partial(u\tau_{yx})}{\partial y} + \frac{\partial(u\tau_{zx})}{\partial z} + \frac{\partial(v\tau_{xy})}{\partial x} + \frac{\partial(v\tau_{yy})}{\partial y} \\ &+ \frac{\partial(v\tau_{zy})}{\partial z} + \frac{\partial(w\tau_{xz})}{\partial x} + \frac{\partial(w\tau_{yy})}{\partial y} + \frac{\partial(w\tau_{zy})}{\partial z} + \rho\mathbf{f} \cdot \mathbf{V}\end{aligned} \tag{1.5}$$

where ρ is the fluid density, p is the pressure, u is the x-component of fluid velocity, v is the y-component of fluid velocity, w is the z-component of fluid velocity, e is the energy per unit mass, $\dot{q}$ is the rate of volumetric heat addition per unit mass, τ_{ij} is the stress tensor with the index i designating the plane on which the stress acts and the second index j designating the direction in which the stress acts, T is the temperature, $\mathbf{V}$ is the fluid velocity vector, and $\mathbf{f}$ is the body force per unit mass.

1.1.1 Equations for Inviscid Flow (the Euler Equations)

For the case of inviscid[6] flow, where the dissipative, transport phenomena of viscosity, mass diffusion, and thermal conductivity are neglected, the Navier-Stokes equations simplify considerably to the Euler Equations. The equations for an unsteady, three-dimensional, compressible inviscid flow are given as follows.

Continuity equation

$$\frac{\partial \rho}{\partial t} + \nabla \cdot (\rho \mathbf{V}) = 0 \tag{1.6}$$

Momentum equations

x component:

$$\frac{\partial (\rho u)}{\partial t} + \nabla \cdot (\rho u \mathbf{V}) = -\frac{\partial p}{\partial x} + \rho f_x \tag{1.7}$$

y component:

$$\frac{\partial (\rho v)}{\partial t} + \nabla \cdot (\rho v \mathbf{V}) = -\frac{\partial p}{\partial y} + \rho f_y \tag{1.8}$$

z component:

$$\frac{\partial (\rho w)}{\partial t} + \nabla \cdot (\rho w \mathbf{V}) = -\frac{\partial p}{\partial z} + \rho f_z \tag{1.9}$$

Energy equation

$$\frac{\partial}{\partial t}\left[\rho\left(e + \frac{V^2}{2}\right)\right] + \nabla \cdot \left[\rho\left(e + \frac{V^2}{2}\right)\mathbf{V}\right] = \rho\dot{q} - \frac{\partial (up)}{\partial x} - \frac{\partial (vp)}{\partial y} - \frac{\partial (wp)}{\partial z} + \rho \mathbf{f} \cdot \mathbf{V} \tag{1.10}$$

Two special cases of the continuity equation are worthy to note. The first case is when the flow is steady; that is, when partial derivative terms with respect to time, $\partial/\partial t$, are zero. Thus $\partial\rho/\partial t = 0$ and at most $\rho = \rho(x, y, z)$. It follows that Eq. (1.6) can be reduced to

$$\nabla \cdot (\rho \mathbf{V}) = \frac{\partial \rho u}{\partial x} + \frac{\partial \rho v}{\partial y} + \frac{\partial \rho w}{\partial z} = 0 \tag{1.11}$$

---

[6] An **inviscid** flow is one where viscous forces are negligibly small so that all dissipative terms in the Navier-Stokes equations involving transport phenomena (e.g. viscosity, mass diffusion, and thermal conductivity) can be ignored.

The second special case is for an incompressible flow, $\rho =$ constant; density is neither a function of space coordinates nor a function of time. For an incompressible fluid, the continuity equation, Eq. (1.6), simplifies to

$$\nabla \cdot \mathbf{V} = \frac{\partial u}{\partial x} + \frac{\partial v}{\partial y} + \frac{\partial w}{\partial z} = 0 \tag{1.12}$$

In some textbooks, the Euler equations refer only the momentum equations and is written in compact vector form as

$$\rho \left[\frac{\partial \mathbf{V}}{\partial t} + (\mathbf{V} \cdot \nabla)\mathbf{V} \right] = -\nabla P + \rho \mathbf{g} \tag{1.13}$$

where **g** is the acceleration of gravity vector and is taken to point downward in a coordinate system where z points upward. We will use Eq. (1.13) to refer to the Euler equation, if necessary.

1.1.2 The Bernoulli Equation

The famous Bernoulli equation can be derived from the Euler equation, Eq. (1.13). Assuming steady incompressible flow, the Bernoulli equation in inviscid regions of flow is

$$\frac{P}{\rho} + \frac{V^2}{2} + gz = C = \text{constant along streamlines} \tag{1.14}$$

The “constant” C in Eq. (1.14) is constant only along a streamline; the constant may change from streamline to streamline.

The Bernoulli equation is simply an expression of mechanical energy balance. In words, it states that the sum of the kinetic, potential, and flow energies of a fluid particle is constant along a streamline during steady flow when compressibility and frictional effects are negligible. An important insight from the Bernoulli equation is that the pressure is low where the fluid velocity is high and the pressure is high where the fluid velocity is low.

1.1.3 Nondimensionalized Equations of Motion

It is possible to rewrite the Navier-Stokes equations in nondimensional form[7]. One of the benefits of doing this is to allow us to properly compare the orders of magnitude of the various terms in the equations. We begin with the incompressible continuity equation,

$$\nabla \cdot \mathbf{V} = 0 \tag{1.15}$$

and the vector form of the Navier-Stokes equation for incompressible flow of a Newtonian fluid with constant properties,

$$\rho \frac{D\mathbf{V}}{Dt} = \rho \left[\frac{\partial V}{\partial t} + (\mathbf{V} \cdot \nabla)\mathbf{V} \right] = -\nabla P + \rho \mathbf{g} + \mu \nabla^2 \mathbf{V} \tag{1.16}$$

Let us define the following nondimensional variables and one nondimensional operator:

$$t^* = ft \qquad \mathbf{x}^* = \frac{\mathbf{x}}{L} \qquad \mathbf{V}^* = \frac{\mathbf{V}}{V} \tag{1.17}$$

$$P^* = \frac{P - P_\infty}{P_0 - P_\infty} \qquad \mathbf{g}^* = \frac{\mathbf{g}}{g} \qquad \nabla^* = L\nabla \tag{1.18}$$

where f is a characteristic frequency, L is a characteristic length, V is a characteristic speed, and $P_0 - P_\infty$ is a reference pressure difference. After much algebra, the original continuity equation and the momentum equation can be written in the following form where only starred (nondimensional) quantities appear:

$$\nabla^* \cdot \mathbf{V}^* = 0 \tag{1.19}$$

$$\left[\frac{fL}{V}\right] \frac{\partial \mathbf{V}^*}{\partial t^*} + \left(\mathbf{V}^* \cdot \nabla^*\right) \mathbf{V}^* = -\left[\frac{P_0 - P_\infty}{\rho V^2}\right] \nabla^* P^* + \left[\frac{gL}{V^2}\right] \mathbf{g}^* + \left[\frac{\mu}{\rho V L}\right] \nabla^{*2} \mathbf{V}^* \tag{1.20}$$

Each of the terms in square brackets in Eq. (1.20) is a nondimensional grouping of parameters. The one on the left is the *Strouhal number*, $\mathrm{St} = fL/V$; the first one on the right is the *Euler number*, $\mathrm{Eu} = (P_0 - P_\infty)/\rho V^2$; the second one on the right is the reciprocal

---

[7] Adapted from Cengel [49].

of the square of the *Froude number*, $\mathrm{Fr}^2 = V^2/gL$; and the last one is the reciprocal of the *Reynolds number*, $\mathrm{Re} = \rho V L/\mu$. Equation (1.20) thus becomes

$$[\mathrm{St}]\,\frac{\partial \mathbf{V}^*}{\partial t^*} + (\mathbf{V}^* \cdot \nabla^*)\,\mathbf{V}^* = -\,[\mathrm{Eu}]\,\nabla^* P^* + \left[\frac{1}{\mathrm{Fr}^2}\right]\mathbf{g}^* + \left[\frac{1}{\mathrm{Re}}\right]\nabla^{*2}\mathbf{V}^* \qquad (1.21)$$

It is important to note that the relative importance of the terms in Eq. (1.21) depends only on the relative magnitudes of the dimensionless parameters St, Eu, Fr, and Re. For example, if St and Eu are of order 1, but Fr and Re are very large, then it is justifiable to ignore the gravitational and viscous terms in the Navier-Stokes equation. In addition, if the flow is steady, then $f = 0$ and the Strouhal number becomes zero so can be dropped out. Finally, the effect of gravity is usually significant only in flows with free-surface effects like ship motion or flow of rivers.

Various useful approximations can be made to simplify analysis of a fluid flow problem where we eliminate one or more of the terms in Eq. (1.20) by comparing the relative magnitudes of the dimensionless parameters associated with the corresponding terms in Eq. (1.21). We have already seen a case where an approximation is made if net viscous forces are very small compared to inertial and/or pressure forces—the Euler equation. The Euler equation is simply the Navier-Stokes equation with the viscous term neglected; it is an *approximation* of the Navier-Stokes equation. Figure 1.1 shows a drawing of fluid flowing over an airfoil, with labels indicating which regions of the flow where applying the Euler equation would be valid and not valid. The orange area in the drawing which surrounds the airfoil and extends beyond its trailing edge is called the boundary layer, a very thin layer of fluid where viscosity cannot be ignored. More about the boundary layer concept will be explained in later sections of this chapter.

The term that is neglected in the Euler approximation ($\mu\nabla^2\mathbf{V}$) is the term that contains the highest-order derivatives of velocity. Mathematically, losing this term means that the number of boundary conditions is effectively reduced. It turns out that when we use the Euler equation approximation, we cannot specify the no-slip boundary condition at solid walls. In other words, fluid *can* slip at solid walls in the Euler approximation; the tangential

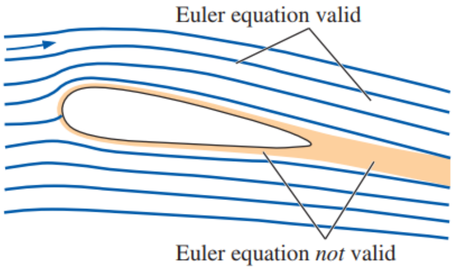

Figure 1.1: The Euler equation is an approximation of the Navier-Stokes equation for regions of flow where the Reynolds number is large and where net viscous forces are negligible compared to inertial and/or pressure forces. Image from Cengel [49].

component of velocity need not be zero, but we still specify that fluid cannot flow through the wall (the normal component of velocity must be zero). Solutions of the Euler equation are therefore not physically meaningful near solid walls! This is an important consequence to keep in mind when the results of this dissertation are presented and analyzed.

We will refer back to the nondimensionalized Navier-Stokes equation when we discuss the boundary layer equations of motion.

1.1.4 Comments about the Navier-Stokes Equations

Some comments about the Navier-Stokes equations are in order before we proceed[8].

1. They are a coupled system of nonlinear partial differential equations, and hence are very difficult to solve analytically. Only a small collection of flow problems have closed-form solutions.

2. For the momentum and energy equations, the difference between the nonconservation and conservation forms of the equations is just the left-hand side. The right-hand side of the equations in the two different forms is the same.

---

[8] Adapted from Anderson [16].

3. The conservation form of the governing equations is sometimes called the *divergence form*. This is because the conservation forms contain terms on the left-hand side which include the divergence of some quantity, such as $\nabla \cdot (\rho \mathbf{V})$ or $\nabla \cdot (\rho u \mathbf{V})$.

4. Historically, the momentum equations for a viscous flow were identified as the Navier-Stokes equations. In modern computational fluid dynamics (CFD) literature, the Navier-Stokes equations include the entire system of flow equations for the solution of a viscous flow—continuity and energy as well as momentum.

1.2 Vorticity and Circulation

Two additional terms from fluid mechanics whose definition are important to understand are vorticity and circulation. The **vorticity**, $\vec{\zeta}$, is a measure of the rotation of a fluid element as it moves in the flow field. Mathematically, it is defined as

$$\vec{\zeta} = \nabla \times \vec{V} \tag{1.22}$$

In cylindrical coordinates, the vorticity is written as:

$$\nabla \times \vec{V} = \hat{e}_r \left(\frac{1}{r} \frac{\partial V_z}{\partial \theta} - \frac{\partial V_\theta}{\partial z} \right) + \hat{e}_\theta \left(\frac{\partial V_r}{\partial z} - \frac{\partial V_z}{\partial r} \right) + \hat{k} \left(\frac{1}{r} \frac{\partial r V_\theta}{\partial r} - \frac{1}{r} \frac{\partial V_r}{\partial \theta} \right) \tag{1.23}$$

In two dimensions, for a flow where the fluid particles do not rotate as they translate (also known as irrotational flow, $\vec{\zeta} = 0$), the particles satisfy the condition of irrotationality, expressed in cylindrical coordinates as

$$\frac{1}{r} \frac{\partial r V_\theta}{\partial r} - \frac{1}{r} \frac{\partial V_r}{\partial \theta} = 0 \tag{1.24}$$

In Cartesian coordinates, the irrotationality condition for two dimensions is given by

$$\frac{\partial v}{\partial x} - \frac{\partial u}{\partial y} = 0 \tag{1.25}$$

The **circulation**, Γ, is defined as the line integral of the tangential velocity component about any closed curve fixed in the flow,

$$\Gamma = \oint_c \vec{V} \cdot d\vec{s}, \tag{1.26}$$

where $d\vec{s}$ is an elemental vector tangent to the curve. Applying Stokes Theorem reveals the close connection between circulation and vorticity:

$$\Gamma = \oint_c \vec{V} \cdot d\vec{s} = \int_A (\nabla \times \vec{V})_z dA \tag{1.27}$$

The above result states that the circulation around a closed contour is equal to the total vorticity enclosed within it.

1.3 Stream Function

For a two-dimensional incompressible flow, the notion of a stream function ψ is extremely useful. It allows us to represent two entities—the velocity components $u(x, y, t)$ and $v(x, y, t)$ of a two-dimensional incompressible flow—with a single function $\psi(x, y, t)$:

$$u \equiv \frac{\partial \psi}{\partial y} \text{ and } v \equiv -\frac{\partial \psi}{\partial x} \tag{1.28}$$

There is a reason why u and v are defined in this way. If one takes the partial derivative of u with respect to x and the partial derivative of v with respect to y, and add the two expressions together, one gets

$$\frac{\partial u}{\partial x} + \frac{\partial v}{\partial y} = \frac{\partial^2 \psi}{\partial x \partial y} - \frac{\partial^2 \psi}{\partial y \partial x} = 0$$

which is exactly the two-dimensional version of the continuity equation for incompressible flow, Eq. (1.12)!

1.4 Velocity Potential

For irrotational flow, the velocity potential function ϕ can be introduced, defined by

$$\vec{V} = -\nabla \phi \tag{1.29}$$

Defining the velocity potential this way guarantees that any continuous scalar function $\phi(x, y, z, t)$ automatically satisfies the irrotationality condition because of a fundamental vector identity[9]:

$$\nabla \times \vec{V} = -\nabla \times \nabla\phi \equiv 0 \tag{1.30}$$

The minus sign is used in the definition so that ϕ decreases in the flow direction, analogous to how temperature decreases in the direction of heat flow in heat conduction. From Eq. (1.29), it follows that

$$u = -\frac{\partial \phi}{\partial x}, v = -\frac{\partial \phi}{\partial y}, \text{ and } w = -\frac{\partial \phi}{\partial z} \tag{1.31}$$

The velocity potential is the companion to the stream function. It only exists for irrotational flow. Irrotationality is often a valid assumption for those regions of a flow in which viscous forces are negligible. The theory for irrotational flow is also referred to as potential flow theory since the velocity field may be defined by the potential function ϕ. More on potential flow theory will be discussed later.

1.5 Basics of Boundary Layer Theory

In this section, we motivate the necessity of boundary layer theory by first considering a classic example. Consider the inviscid flow over a cylinder in two dimensions, as depicted in Fig. 1.2a. Notice that the streamlines around the cylinder are symmetric from front-to-back. Since the mass flow between any two streamlines is constant, wherever streamlines come closer together, the velocity of the fluid must increase. Likewise, wherever streamlines open up, the velocity of the fluid must decrease. Hence, the velocity of the fluid must be relatively low at points A and C, and really high at point B. In fact, the air comes to rest at points A and C—they are called *stagnation points*. Point B turns out to be where the fluid velocity on the surface of the cylinder is greatest.

It can be shown[10] that wherever the velocity is high in a flow field, the pressure is low, and vice versa. It follows that points A and C have relatively large (and equal) pressures; point B will be a point of low pressure. The fact that the streamlines around the cylinder are

---

[9] The identity $\nabla \times \nabla(\ ) \equiv 0$ can easily be demonstrated by expanding into components.

[10] One straightforward way to see this is to study the implications of the Bernoulli Equation, arguably the most well-known (and misused) equation in fluid mechanics.

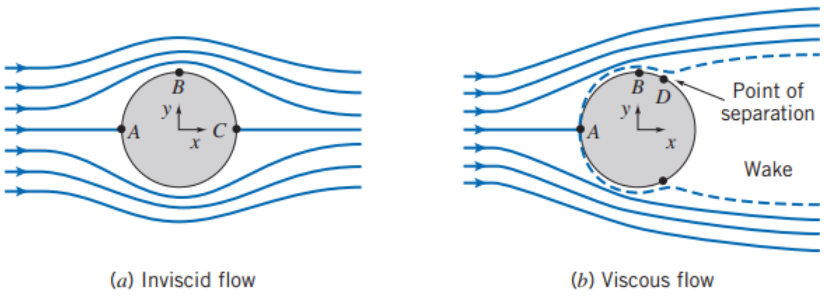

Figure 1.2: (a) Qualitative picture of incompressible flow over a cylinder. (b) Qualitative picture of actual flow over a cylinder. Image from Fox [41].

symmetric hints at the conclusion that the pressure distribution on the cylinder is symmetric as well. This means there is no net drag force due to pressure. Since we are also assuming inviscid flow, there can be no drag due to friction either. These conclusions are obviously unrealistic; we know a golf ball experiences drag when it flies through the air. The result that a body experiences no drag whatsoever in inviscid flow is known as d'Alembert's paradox of 1752.

The failure of inviscid theory to predict any drag on a cylinder immersed in an airflow was finally resolved in 1904, over 150 years later. The answer was found by a German engineer by the name of Ludwig Prandtl. Prandtl was aware of the no-slip condition in fluid mechanics, an experimental fact that a fluid moves at the same velocity as the surface of a solid interface. For a surface at rest, the fluid velocity must therefore be zero at the solid surface. As mentioned above, inviscid theory predicted that point B on the cylinder had the highest velocity; it should be zero due to the no-slip condition instead. Prandtl suggested that even though friction is negligible for certain flows, there will always be a thin **boundary layer** in which friction *is* significant and cannot be ignored. Across the width of the boundary layer, the velocity increases rapidly from zero at the surface to the value that inviscid theory predicts on the outer edge of the boundary layer. This is shown in Fig. 1.2b from point A to point B, and in more detail in Fig. 1.3.

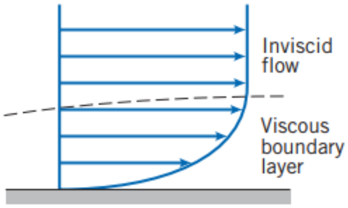

Figure 1.3: Schematic of a boundary layer. Image from Fox [41].

Boundary layer theory was the missing link between inviscid theory and experimental observations. The boundary layer approximation corrects some of the major deficiencies of the Euler equation by providing a way to enforce the no-slip condition at solid walls. As a consequence, viscous forces can exist along walls and bodies immersed in a free stream can experience aerodynamic drag. In addition to reconciling theory and experiment, the concept of a boundary layer led to another important consequence: bodies immersed in a flow often have a *wake*, as shown in Fig. 1.2b from point D onward. Point D is called a separation point, where fluid particles are pushed off the cylinder and cause a wake to develop.

It is important to emphasize that boundary layer theory gives only approximate solutions of the full Navier-Stokes equations for specific regions of fluid flow like near solid surfaces. As with any approximation, care must be exercised with respect to when and where we apply it to solve problems. The key to successful application of the boundary layer approximation is the assumption that the boundary layer is very thin.

A more complete picture can now be attained to understand the airflow over a cylinder. Referring back to Fig. 1.2a, as a fluid particle moves along the surface from point B to C, it moves from a region of low to high pressure. This kind of change in pressure is known as an *adverse pressure gradient*[11] because it will cause fluid particles in the boundary-layer to slow down at a greater rate than that due to boundary-layer friction alone. If the adverse pressure

---

[11] This is in contrast to a *favorable pressure gradient* in which the pressure decreases in the flow direction. It is called favorable because it tends to overcome the slowing of fluid particles caused by friction in the boundary layer.

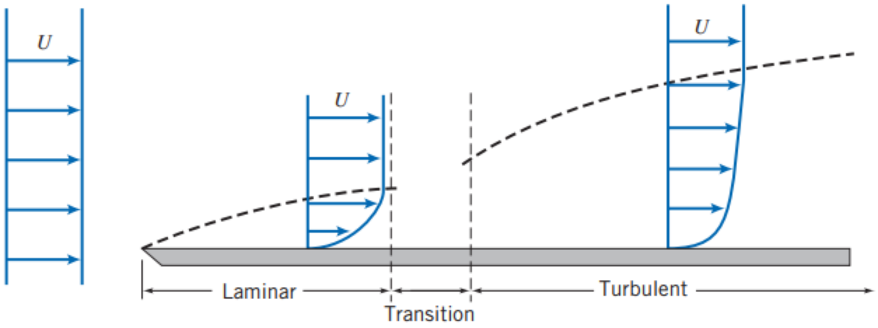

Figure 1.4: Boundary layer on a flat plate. The vertical thickness has been greatly exaggerated for clarity. Image from Fox [41].

gradient is strong enough, the fluid particles in the boundary layer will actually be brought to rest. When this happens, the particles will be forced away from the cylinder surface (i.e., there is flow separation, indicated by point D in Fig. 1.2b) as they make room for trailing fluid particles. This behavior results in a wake in which flow is turbulent. It turns out that the wake will always be relatively low in pressure, but the front of the cylinder will be at a relatively high pressure. Therefore the cylinder now experiences a pressure drag due to this pressure difference.[12]

1.5.1 Boundary-Layer Thicknesses

The thickness of the boundary layer is an important parameter to keep in the back of our mind in this thesis, so let us define it here. It turns out that the location of the edge of the boundary layer—its thickness—is not as obvious as one would think. To see why this is so, refer to Fig. 1.4. This figure shows a typical boundary layer formed over a flat plate for laminar as well as turbulent flow. The difficulty in identifying the edge of the boundary layer lies in the fact that within the boundary layer, the velocity gradients only asymptotically

---

[12] It is interesting to note that although the boundary layer is necessary to explain the drag on the cylinder, the drag is actually due mostly to the asymmetric pressure distribution created by the boundary layer separation. Drag due directly to friction is still negligible [41].

approach zero as we reach the edge of the boundary layer for both laminar and turbulent flow. We cannot simply define the edge to be where the boundary-layer velocity u equals the free stream velocity U because it would take an infinite amount of time to approach U! Because of this, several boundary-layer definitions have been developed: the disturbance thickness δ, the displacement thickness δ^*, and the momentum thickness θ. For our purposes, we will only consider the disturbance thickness δ definition. It is defined as the distance from the surface at which the velocity is within 1 percent of the free stream velocity, $u \approx 0.99U$.

It turns out that for a given fluid and plate, the higher the free-stream speed U, the thinner the boundary layer. In nondimensional terms, the Reynolds number based on distance x along the plate is defined as

$$\mathrm{Re}_x = \frac{\rho U x}{\mu} = \frac{Ux}{\nu} \tag{1.32}$$

At a given x-location, the higher the Reynolds number, the thinner the boundary layer. Since the accuracy of the boundary layer approximation improves when the boundary layer is very thin ($\delta \ll x$), another way to interpret the previous statement is the higher the Reynolds number, all else being equal, the more reliable the boundary layer approximation.

For a laminar boundary layer growing over a flat plate, as in Fig. 1.4, the boundary layer thickness δ is at most a function of U, x, and fluid properties ρ and μ. It turns out that δ is proportional to the square root of x. As we move down the plate to larger and larger values of x, Re_x increases linearly with x. At some point, infinitesimal disturbances in the flow begin to grow, and the boundary layer cannot remain laminar. This marks the start of a transition process toward turbulent flow. For a smooth flat plate with a uniform free stream as pictured in Fig. 1.4, the transition process begins at a critical Reynolds number, $\mathrm{Re}_{x,\,\text{critical}} \cong 1 \times 10^5$, and continues until the boundary layer is fully turbulent at the transition Reynolds number, $\mathrm{Re}_{x,\,\text{transition}} \cong 3 \times 10^6$.

Please note that in Fig. 1.4, the vertical scale has been greatly exaggerated and the horizontal scale has been shortened. In actuality, since $\mathrm{Re}_{x,\,\text{transition}} \cong 30$ times $\mathrm{Re}_{x,\,\text{critical}}$, the transitional region is much longer than shown in the figure. If drawn to scale, the boundary layer on a flat plate will be visibly thin.

In real-life engineering flows, transition to turbulent flow usually happens abruptly and much earlier (at a lower value of Re_x than the values given previously for a smooth flat plate with a calm free stream). Factors such as surface roughness, free-stream disturbances, flow unsteadiness, and curvature of the wall can lead to an earlier transition location. Because of this, there is an engineering critical Reynolds number, $\mathrm{Re}_{x,\,\mathrm{cr}} = 5 \times 10^5$, that is often used to determine whether a boundary layer is most likely laminar or most likely turbulent. If a boundary layer is most likely laminar, $\mathrm{Re}_x < \mathrm{Re}_{x,\,\mathrm{cr}}$. If a boundary layer is most likely turbulent, $\mathrm{Re}_x > \mathrm{Re}_{x,\,\mathrm{cr}}$. In practice, one often ignores transition by treating the first part of transition as laminar and the remaining part as turbulent.

The transition process is unsteady and is difficult to predict, even with modern computational fluid dynamics (CFD) software[13]. In some cases, engineers intentionally place rough sandpaper or trip wires along the surface in order to force transition at a specific location. Doing this leads to the creation of vortices that enhance local mixing and create disturbances to progress to a turbulent boundary layer more quickly. This is desirable in certain applications like putting dimples on golf balls to increase their range of flight.

1.5.2 Boundary Layer Equations

Recall that the Euler equation is an approximation of the Navier-Stokes equation that is applicable to regions of a flow field where net viscous forces are negligible compared to inertial and/or pressure forces. Refer back to Fig. 1.1. This figure shows where the Euler equation would be valid and where it would not be valid for the case of fluid flow over an airfoil. The natural question to ask is: how do we handle flow regions where the Euler equation is not valid? Now that we have a better understanding of the boundary layer, we can answer this question in a more satisfying manner. In practice, the Euler equation is often used as the first step in a boundary layer approximation. Namely, the Euler equation is applied over the whole flow field, including regions close to walls and wakes, where we

---

[13] A basic introduction to CFD is given in a later section of this chapter.

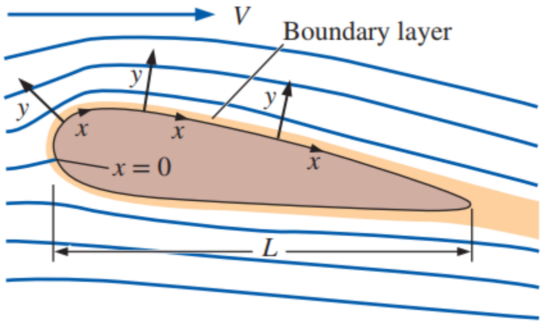

Figure 1.5: The boundary layer coordinate system for flow over a body. The x coordinate follows the surface and is typically set to zero at the front stagnation point of the body, and y is everywhere normal to the surface locally. Image from Cengel [49].

know the approximation is not appropriate. Then, a thin boundary layer is inserted in these regions as a correction to account for viscous effects.

The equations of motion to be used in boundary layer calculations are known as the **boundary layer equations**. For simplicity, only the case of steady, two-dimensional flow in the xy-plane is presented here. We neglect gravity since we are not dealing with free surfaces where gravitational effects are dominant, and we consider only laminar boundary layers. A convenient coordinate system to use is where x is everywhere parallel to the wall and y is everywhere normal to the wall (Fig. 1.5). Such a coordinate system is called a boundary layer coordinate system; it is locally orthogonal. When one solves the boundary layer equations, one does so at one x-location at a time, using this coordinate system locally. It is not critical where we define $x = 0$, but for flow over a body, as in Fig. 1.5, we typically set $x = 0$ at the front stagnation point.

For a full derivation of the boundary layer equations, the reader is encouraged to consult a fluid mechanics textbook such as the one by Cengel and Cimbala [49]. We will only highlight the main points here in the interest of brevity and time. One approach is to begin with the nondimensionalized Navier-Stokes equation, Eq. (1.21), reproduced here for convenience:

$$[\mathrm{St}]\,\frac{\partial \mathbf{V}^*}{\partial t^*} + \left(\mathbf{V}^* \cdot \nabla^*\right)\mathbf{V}^* = -\,[\mathrm{Eu}]\,\nabla^* P^* + \left[\frac{1}{\mathrm{Fr}^2}\right]\mathbf{g}^* + \left[\frac{1}{\mathrm{Re}}\right]\nabla^{*2}\mathbf{V}^* \tag{1.33}$$

After neglecting the unsteady term and the gravity term, the above equation reduces to

$$\left(\mathbf{V}^* \cdot \nabla^*\right)\mathbf{V}^* = -\,[\mathrm{Eu}]\,\nabla^* P^* + \left[\frac{1}{\mathrm{Re}}\right]\nabla^{*2}\mathbf{V}^* \tag{1.34}$$

For boundary layers, x is of order of magnitude L, and the Reynolds number in Eq. (1.34) can be thought of as Re_x, Eq. (1.32). Re_x is very large in typical applications of the boundary layer approximation. This would seem to imply that we could neglect the last term in Eq. (1.34) in boundary layers. Doing so, however, would result in the Euler equation, with all of its deficiencies. Thus it is necessary to keep at least *some* of the viscous terms in Eq. (1.34). How do we decide which terms to keep and which to neglect? The key lies in realizing what the appropriate length scales and velocity scale are in boundary layers. For instance, it makes more sense to use the boundary layer height δ instead of L as the length scale for distances normal to the streamwise direction and for derivatives with respect to y. Furthermore, while the free stream velocity V is a characteristic scale for the whole flow field, it is more appropriate to use the component of velocity that is parallel to the wall at the location just above the boundary layer (we will call it U). These realizations lead to the redefinition of nondimensional variables that are normalized by the appropriate characteristic parameters relevant to the problem.

The logic sequence just presented illustrates just how useful working with a nondimensionalized form of an equation can be. Of course, it is always possible to revert back to the original (physical) variables if desired.

We summarize here the most important results from a boundary layer analysis. The first important result is

$$\frac{\partial P}{\partial y} \cong 0 \tag{1.35}$$

In words, Eq. (1.35) says that there is negligible change in pressure in the direction normal to the wall in a boundary layer, although pressure may vary along the wall in the x-direction.

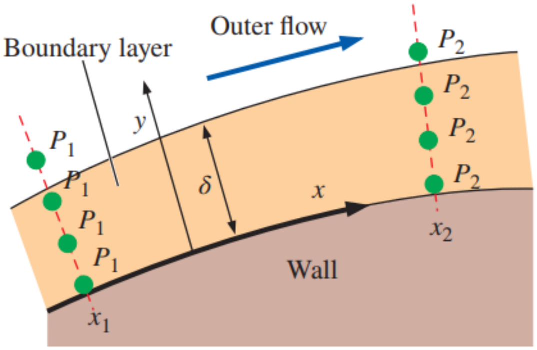

Figure 1.6: Pressure may change along a boundary layer in the x-direction, but any change in pressure across the boundary layer in the y-direction is negligible. Image from Cengel [49].

This is illustrated in Fig. 1.6. At $x = x_1$, $P = P_1$ for all values of y across the boundary layer from the wall all the way to the outer edge. At some other x-location, $x = x_2$, the pressure may take on a different value, but $P = P_2$ for all values of y across that section of the boundary layer.

The first result comes from a y-momentum equation analysis of the boundary layer. Since the pressure across the boundary layer has been shown to be the same as that outside the boundary layer, we can apply the Bernoulli equation to the outer flow region. If we ignore any change in elevation (this is justified since the boundary layer is very thin), differentiating Eq. (1.14) with respect to x gives

$$\frac{P}{\rho} + \frac{1}{2}U^2 = \text{constant} \qquad \rightarrow \qquad \frac{1}{\rho}\frac{dP}{dx} = -U\frac{dU}{dx} \tag{1.36}$$

Recall that $U(x)$ here represents the outer flow speed parallel to the wall. Equation (1.36) is very useful to help understand the relationship between pressure gradient and velocity gradient in the boundary layer.

The second important result from a boundary layer analysis is

$$\frac{\delta}{L} \sim \frac{1}{\sqrt{\mathrm{Re}_L}} \tag{1.37}$$

This result says that at a given streamwise location along the wall, the larger the Reynolds number, the thinner the boundary layer. If we substitute x for L in Eq. (1.37), we arrive at the conclusion that for a laminar boundary layer on a flat plate, where $U(x) = V =$ constant, δ grows like the square root of x.

Finally, we now summarize the set of equations of motion for a steady, incompressible, laminar boundary layer in the xy-plane with negligible gravitational effects:

$$\frac{\partial u}{\partial x} + \frac{\partial v}{\partial y} = 0 \tag{1.38}$$

$$u\frac{\partial u}{\partial x} + v\frac{\partial u}{\partial y} = U\frac{dU}{dx} + \nu\frac{\partial^2 u}{\partial y^2} \tag{1.39}$$

The *form* of the boundary layer equations, specifically the x-momentum boundary layer equation—Eq. (1.39)—is of especial importance to note. Mathematically, the full Navier-Stokes equation is elliptic in space. This means that boundary conditions are required over the entire boundary of the flow domain. Physically, flow information is passed in all directions, both upstream and downstream. On the contrary, the x-momentum boundary layer equation is parabolic in space. This means that we only need to specify boundary conditions on three sides of the (two-dimensional) flow domain. For a typical boundary layer problem along a wall, then, we need only specify boundary conditions upstream and on the top and bottom of the flow domain; boundary conditions downstream are not needed. Physically, this implies that flow information is not passed in the direction opposite to the flow from downstream.

A few comments about the boundary layer equations are in order.

1. When the Reynolds number is too high, the boundary layer is no longer laminar. If the flow is transitional or fully turbulent, Eqs. (1.38) and (1.39) are not valid.

2. If flow separation occurs, the boundary layer approximation is not appropriate in the separated flow region. This is because a separated flow region contains reverse flow, and the parabolic nature of the boundary layer equations is lost.

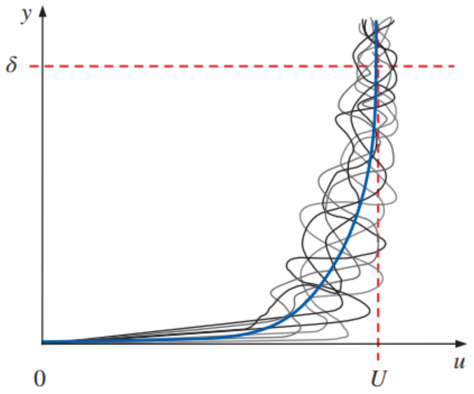

Figure 1.7: The velocity profile of a turbulent boundary layer is unsteady. The thin, wavy lines are instantaneous profiles, and the blue line is a time-averaged profile. Image from Cengel [49].

1.5.3 Laminar vs. Turbulent Flat Plate Boundary Layer

Boundary layer equations for turbulent flow are much more complex than their laminar counterparts. In fact, expressions for the boundary layer profile shape and other properties are obtained empirically or semi-empirically at best, since it is not possible to solve the boundary layer equations analytically for turbulent flow. A defining characteristic of turbulent flows is that they are inherently unsteady; the instantaneous velocity profile shape varies with time, as shown in Fig. 1.7. Because of this, turbulent expressions are often represented by time-averaged values. A commonly used empirical approximation for the time-average velocity profile of a turbulent flat plate boundary layer is the **one-seventh-power law**,

$$\frac{u}{U} \cong \left(\frac{y}{\delta}\right)^{1/7} \text{ for } y \leq \delta, \qquad \frac{u}{U} \cong 1 \text{ for } y > \delta \tag{1.40}$$

In the above approximation, δ is not the 99 percent boundary layer thickness, but rather the actual edge of the boundary layer. Equation (1.40) is plotted in Fig. 1.8, where the laminar flat plate boundary layer profile is also plotted for comparison. If the laminar and turbulent boundary layers were the same thickness, notice that the turbulent one is much fuller than the laminar one. This indicates that a turbulent boundary layer contains higher-

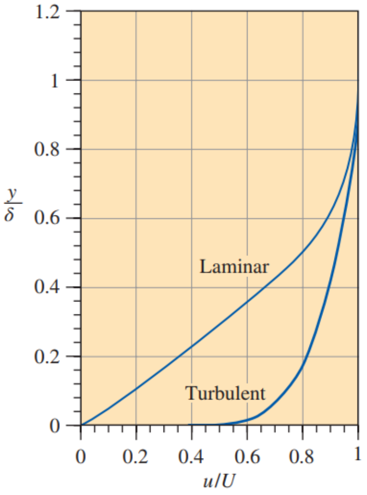

Figure 1.8: Comparison of laminar and turbulent flat plate boundary layer velocity profiles. The vertical axis is nondimensionalized by boundary layer thickness. Image from Cengel [49].

speed flow close to the wall due to large turbulent eddies that transport high-speed fluid from the outer part of the boundary layer down to the lower parts of the boundary layer (and vice versa). The large eddies promote more rapid and thorough mixing as compared to how fluid mixes in a laminar boundary layer where mixing is driven mainly by viscous dissipation—a much slower process.

Please note that very close to the wall ($y \to 0$), the one-seventh-power law is not physically meaningful because it predicts that the slope ($\partial u/\partial y$) is infinite at $y = 0$. While it is true that the slope at the wall is very large for a turbulent boundary layer, it is nevertheless finite. This observation illustrates the limitation(s) that many empirical models of turbulent boundary layers like the one-seventh-power law have in terms of its range of applicability.

1.5.4 Boundary Layers with Pressure Gradients

The boundary layer of a flat plate is often called a zero pressure gradient boundary layer because the outer flow is a uniform free stream of constant velocity, $U(x) = V =$ constant.

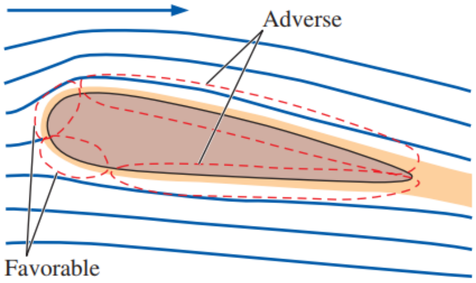

Figure 1.9: The boundary layer along an airfoil immersed in a free stream flow. A favorable pressure gradient appears at the front portion of the airfoil, and an adverse pressure gradient appears at the rear portion of the airfoil. Image from Cengel [49].

Thus $dU/dx = 0$ in Eq. (1.39) and there is no pressure gradient term in the x-momentum boundary layer equation. The flat plat boundary layer is often used as ballpark estimates for such things as location of transition to turbulence, boundary layer thickness, etc.

In more practical flows, however, the boundary layers on walls of arbitrary shape have *nonzero* pressure gradients. In the situation where the flow in the inviscid and/or irrotational outer flow region (outside of the boundary layer) accelerates, $U(x)$ increases and $P(x)$ decreases[14]. We call this a **favorable pressure gradient** because the boundary layer in such an accelerating flow is usually thin, hugs closely to the wall, and therefore is not likely to separate from the wall. When the outer flow decelerates, $U(x)$ decreases, $P(x)$ increases, and the situation is called an **unfavorable** or **adverse pressure gradient** because the boundary layer is usually thicker, does not hug closely to the wall, and is much more likely to separate from the wall. The thickness of the boundary layer, therefore, can be used as a coarse indication of the local pressure gradient at a given location.

Figure 1.9 shows external flow over an airplane wing. The boundary layer in the front portion of the wing is subjected to a favorable pressure gradient, while the rear portion is subjected to an adverse pressure gradient. If the adverse pressure gradient is strong

---

[14] Refer to Eq. (1.36).

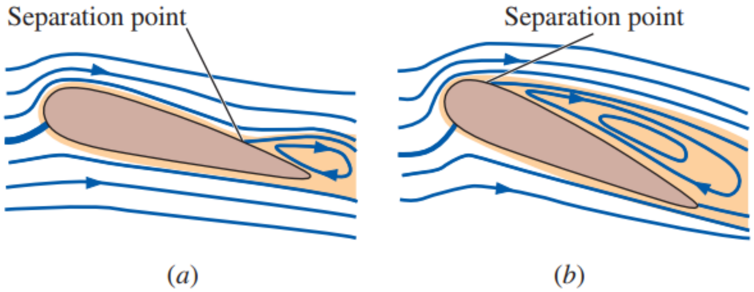

Figure 1.10: Examples of boundary layer flow separation in regions of adverse pressure gradient: (a) an airplane wing at a moderate angle of attack and (b) the same wing at a high angle of attack. Adapted from Cengel [49].

enough ($dP/dx = -UdU/dx$ is large), the boundary layer is likely to separate off the wall. Flow separation in regions of adverse pressure gradient is demonstrated in Fig. 1.10. In Fig. 1.10a, an airfoil wing is positioned at a moderate angle of attack. Notice that the boundary layer remains attached over the entire lower surface of the airfoil, but it separates somewhere near the rear of the upper surface. The closed streamline sketched in the figure indicates a region of recirculating flow called a separation bubble. Since the boundary layer equations are parabolic in space (meaning that no information can be passed upstream from the downstream boundary), this reverse flow cannot be described accurately by the boundary layer equations. In other words, the boundary layer equations are not valid downstream of a separation point due to reverse flow in the separation bubble.

In Fig. 1.10b, the same airfoil is positioned at a higher an angle of attack. Notice in this case how the separation point has moved closer to the front of the airfoil and the separation bubble covers nearly the entire upper surface of the airfoil. This condition is known as stall, and is accompanied by a loss of lift and an increase in drag. Many flight accidents are caused by stalling conditions.

Boundary layers with nonzero pressure gradients can be laminar or turbulent. The mean velocity profile of a turbulent boundary layer is much fuller than a laminar boundary layer under similar conditions. Consequently, a stronger adverse pressure gradient is required to separate a turbulent boundary layer. It follows, then, that turbulent boundary layers are more resistant to flow separation than laminar boundary layers when subject to the same adverse pressure gradient.

1.5.5 Delaying Boundary Layer Separation

We have seen that flow separation occurs when flow reversal occurs. This is usually a bad thing because it causes increased drag, caused by the pressure differential between the front and rear surfaces of the object. The physics of boundary layers helps us understand how to delay boundary layer separation: delay flow reversal. When a boundary layer finds itself in an adverse pressure gradient, there is a competition between the pressure gradient pushing the fluid backwards and momentum diffusing from the free stream into the boundary layer. If the pressure gradient is strong or the momentum diffuses down slowly, the boundary layer velocity profile reverses and separation occurs. The flow detaches from the surface and instead takes the forms of eddies and vortices. However, if we increase the rate of momentum transfer from the free stream into the boundary layer just enough, it is possible to force all the fluid to move forwards and the flow to reattach. One way to do this for a given flow speed is to increase the viscosity of the fluid. When the viscosity increases, the rate of momentum transfer increases. However, increasing the viscosity of the fluid is usually not possible in practical situations. For example, if one is flying in an airplane, it is simply not possible to increase the viscosity of the air that the plane is flying through. There are other techniques, one of which is to inject high-momentum fluid just upstream of the separation point. When we do that, the boundary layer is pushed downstream and the flow reattaches. This is part of the principle behind leading edge slats on airplane wings [46]. Another method is to use passive flow control devices like vortex generators (VGs). The basic operating principle behind VGs will be described in greater detail later in this chapter. In essence, VGs help delay boundary layer separation by inducing streamwise vortices that draw high-momentum fluid in the outer flow into the lower-momentum boundary layer. This transfer of momentum to fluid elements in the boundary layer increases their overall velocity so they can work their way “uphill” against an adverse pressure gradient [26].

1.6 Potential Flow Theory

We have seen how the Navier-Stokes equations can be reduced to the Euler Equations when viscosity is ignored. It turns out that the Euler Equations themselves can be further simplified by making some additional assumptions:

- the flow is steady;
- the velocity remains smaller than the speed of sound (incompressible flow);
- there is no vorticity (irrotational flow).

These simplifications of the Navier-Stokes equations form the basis of **potential flow theory**. Much of classical aerodynamics was built upon potential theory because it was found that many phenomena can be approximated this way. Viscous effects are normally confined to a very thin boundary layer and many flows are effectively irrotational (except for isolated points, lines or sheets). Furthermore, most applications of interest in aerodynamics are subsonic. But probably the most pleasant aspect about potential flow theory is its mathematical nature: it is *linear*. This means that the principle of superposition applies, and we can construct new solutions by adding known solutions together. The ability to combine simple solutions together is truly a powerful thing. Complicated flow patterns can be constructed from some simple flow patterns as building blocks, and the solutions of these complex flows are simply sums of simpler solutions.

For a two-dimensional, incompressible, irrotational flow, the velocity components u and v expressed in terms of both the stream function ψ and velocity potential ϕ are given by[15]:

$$u = \frac{\partial \psi}{\partial y} \qquad v = -\frac{\partial \psi}{\partial x} \tag{1.41}$$

---

[15] Adapted from Fox [41].

$$u = -\frac{\partial \phi}{\partial x} \qquad v = -\frac{\partial \phi}{\partial y} \tag{1.42}$$

Substituting for u and v from Eq. (1.41) into the irrotationality condition,

$$\frac{\partial v}{\partial x} - \frac{\partial u}{\partial y} = 0$$

we obtain

$$\frac{\partial^2 \psi}{\partial x^2} + \frac{\partial^2 \psi}{\partial y^2} = \nabla^2 \psi = 0 \tag{1.43}$$

Substituting for u and v from Eq. (1.42) into the continuity equation,

$$\frac{\partial u}{\partial x} + \frac{\partial v}{\partial y} = 0 \tag{1.44}$$

leads to

$$\frac{\partial^2 \phi}{\partial x^2} + \frac{\partial^2 \phi}{\partial y^2} = \nabla^2 \phi = 0 \tag{1.45}$$

Notice that Eqs. (1.43) and (1.45) have the form of Laplace's equation. Therefore, we have shown that any function ψ or ϕ that represents a possible two-dimensional, incompressible, irrotational flow field must satisfy Laplace's equation.

1.7 The Vortex Two-Dimensional Flow

In potential flow theory, there is a collection of elementary two-dimensional flows that form the basis for more complex flow patterns: a uniform flow, a source, a sink, a vortex, and a doublet. The most important two-dimensional flow for this thesis is the vortex. A **vortex** is a flow pattern in which the streamlines are concentric circles. A potentially confusing point about vortices is that the fluid particles rotate as they go around in circles; this is not necessarily the case at all. It is quite possible to have a situation where the fluid particles move in concentric circles without rotating at all! This is called a *free (irrotational) vortex*, where the fluid particles do not rotate as they translate in circular paths around a common center. The irrotational vortex is the type that concerns us most in this thesis.

When the vortex is irrotational, the velocity field components are $V_r = 0$ and $V_\theta = f(\theta)$ only. Substituting these components into the condition of irrotationality in cylindrical coordinates, Eq. (1.24), leads to

$$\frac{1}{r}\frac{d(rV_\theta)}{dr} = 0.$$

Integrating this equation yields

$$V_\theta r = \text{constant}$$

or

$$V_\theta = f(r) = \frac{C}{r} \tag{1.46}$$

Notice that for an irrotational flow, the origin is a singular point where $V_\theta \to \infty$. The circulation for any contour enclosing the origin is

$$\Gamma = \oint_c \vec{V} \cdot d\vec{s} = \int_0^{2\pi} \frac{C}{r} r d\theta = 2\pi C \tag{1.47}$$

Combining the two results above gives

$$V_\theta = \frac{\Gamma}{2\pi r} \tag{1.48}$$

where Γ is defined to be the strength of the vortex. The result above is also known as the Biot-Savart law; it is the velocity field that an irrotational vortex produces in its surrounding. The velocity field of any other vortex in the vicinity of this source vortex will be induced by this field.

The stream function for an irrotational vortex can be obtained by integrating the velocity components, giving

$$\psi(r,\theta) = \frac{\Gamma}{2\pi} \ln r \tag{1.49}$$

In Cartesian coordinates, the stream function is given by

$$\psi(x,y) = \frac{\Gamma}{4\pi} \ln(x^2 + y^2) \tag{1.50}$$

and the velocity components are:

$$u(x,y) = \frac{\Gamma}{2\pi} \frac{y}{x^2 + y^2} \qquad v(x,y) = -\frac{\Gamma}{2\pi} \frac{x}{x^2 + y^2} \tag{1.51}$$

1.8 Basics of Computational Fluid Dynamics

Recall that the Navier-Stokes equations governing the motion of fluids are non-linear, second-order partial differential equations (PDEs). Exact solutions only exist for a small class of simple flows (e.g., laminar flow past a flat plate). In general, we must resort to numerical methods for more complex flows and geometries. This is where computational fluid dynamics (CFD) comes to the rescue. CFD is today an equal partner with pure theory and pure experiment in the analysis and solution of fluid dynamic problems. It is important to emphasize that CFD complements theory and experiment—it does not replace it!

What does a typical CFD simulation workflow look like? The starting point of every CFD workflow is the creation of the geometry for the problem using a computer-aided design software. Next we proceed to generate a mesh for the geometry and assign to the boundaries of the computational domain appropriate surface patches. A mesh subdivides the geometry into discrete cells that approximate its entire composition. The type and quality of mesh one uses can greatly influence the accuracy of the CFD solutions obtained. After we have a valid mesh, we proceed to setting up the simulation case on a particular CFD software and we launch/monitor the simulation. At the end, we do the post-processing and analyze the results of the simulation qualitatively and quantitatively, if necessary.

In order to solve the equations of fluid motion, one must convert the equations from continuous form to discrete form. This is necessary because computers cannot solve PDEs! But they *can* do basic arithmetic: $+$, $-$, $\times$, and $\div$. There are many discretization methods available. Some more popular methods are the finite difference method (FDM), the finite volume method (FVM), and the finite element method (FEM). We will only discuss the finite difference method due to its simplicity.

1.8.1 Finite Difference Method

The finite difference method is the easiest to understand in regards to how the equations of fluid motion are discretized. Shown in Fig. 1.11 is a two-dimensional grid labeled by indices

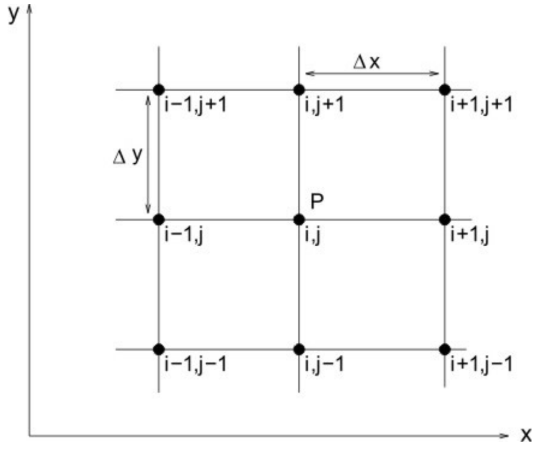

Figure 1.11: Discrete grid points for two dimensions.

i and j. The index i is another label for the x position; the index j is another label for the y position.

The finite difference method is based on the Taylor's series expansion about a point (i, j). If $u_{i,j}$ denotes the x component of velocity at a point (i, j), then the velocity $u_{i+1,j}$ at point $(i+1, j)$ can be expressed in terms of a Taylor series expanded about point (i, j) as follows:

$$u_{i+1,j} = u_{i,j} + \left(\frac{\partial u}{\partial x}\right)_{i,j} \Delta x + \left(\frac{\partial^2 u}{\partial x^2}\right)_{i,j} \frac{(\Delta x)^2}{2} + \left(\frac{\partial^3 u}{\partial x^3}\right)_{i,j} \frac{(\Delta x)^3}{6} + \cdots \tag{1.52}$$

Solving Eq. (1.52) for $(\partial u/\partial x)_{i,j}$, we obtain

$$\left(\frac{\partial u}{\partial x}\right)_{i,j} = \underbrace{\frac{u_{i+1,j} - u_{i,j}}{\Delta x}}_{\text{Finite-difference representation}} \underbrace{- \left(\frac{\partial^2 u}{\partial x^2}\right)_{i,j} \frac{(\Delta x)}{2} - \left(\frac{\partial^3 u}{\partial x^3}\right)_{i,j} \frac{(\Delta x)^2}{6} + \cdots}_{\text{Truncation error}} \tag{1.53}$$

The first term on the right-hand side of Eq. (1.53) is a finite-difference representation of the partial derivative. The remaining terms on the right make up what is called the *truncation error.* In other words, we can approximate the partial derivative with the expression,

$$\left(\frac{\partial u}{\partial x}\right)_{i,j} \approx \frac{u_{i+1,j} - u_{i,j}}{\Delta x} \tag{1.54}$$

and the error associated with using this approximation is given by the truncation error. Since the lowest-order term in the truncation error involves Δx to the first power, the finite-

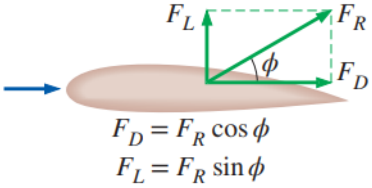

Figure 1.12: Drag and lift forces on a 2D body are simply component forces of the net resultant force on the body due to pressure and viscous forces. The blue arrow indicates the direction of fluid flow relative to the airfoil. Adapted from Cengel [49].

difference expression in Eq. (1.54) is called *first-order-accurate.* Formally, we write Eq. (1.53) as

$$\left(\frac{\partial u}{\partial x}\right)_{i,j} = \frac{u_{i+1,j} - u_{i,j}}{\Delta x} + \mathcal{O}(\Delta x) \tag{1.55}$$

where the symbol $\mathcal{O}(\Delta x)$ is a formal mathematical notation that stands for "terms of order Δx."

Referring to Fig. 1.11, note that the finite-difference expression in Eq. (1.55) uses information to the right of grid point (i, j) but not information to its left; that is, it uses $u_{i+1,j}$ as well as $u_{i,j}$, but not $u_{i-1,j}$. For this reason, Eq. (1.55) is also referred to as a *first-order forward difference* representation for the derivative $(\partial u/\partial x)_{i,j}$.

We can continue to follow this strategy of applying the Taylor series expansion about the point (i, j) using other neighboring grid points. The result will be other finite-difference approximations of specific partial derivatives of interest. Table 1.1 summarizes some of the more common finite-difference schemes encountered in CFD.

1.9 Drag and Lift

The concepts of drag and lift are extremely important in external flows, so let us spend some time defining them in more exact terms. When a fluid moves over a solid body in two-dimensional flows, it exerts pressure forces normal to the body surface and shear forces parallel to the body surface. The *resultant* of the pressure and shear forces acting on the body

FD scheme	**Expression**	**FD scheme**	**Expression**
First-order forward difference with respect to x	$\left(\frac{\partial u}{\partial x}\right)_{i,j} = \frac{u_{i+1,j}-u_{i,j}}{\Delta x}$	First-order forward difference with respect to y	$\left(\frac{\partial u}{\partial y}\right)_{i,j} = \frac{u_{i,j+1}-u_{i,j}}{\Delta y}$
First-order rearward difference with respect to x	$\left(\frac{\partial u}{\partial x}\right)_{i,j} = \frac{u_{i,j}-u_{i-1,j}}{\Delta x}$	First-order rearward difference with respect to y	$\left(\frac{\partial u}{\partial y}\right)_{i,j} = \frac{u_{i,j}-u_{i,j-1}}{\Delta y}$
Second-order central difference with respect to x	$\left(\frac{\partial u}{\partial x}\right)_{i,j} = \frac{u_{i+1,j}-u_{i-1,j}}{2\Delta x}$	Second-order central difference with respect to y	$\left(\frac{\partial u}{\partial y}\right)_{i,j} = \frac{u_{i,j+1}-u_{i,j-1}}{2\Delta y}$
Second-order central second difference with respect to x	$\left(\frac{\partial^2 u}{\partial x^2}\right)_{i,j} = \frac{u_{i+1,j}-2u_{i,j}+u_{i-1,j}}{(\Delta x)^2}$	Second-order central second difference with respect to y	$\left(\frac{\partial^2 u}{\partial y^2}\right)_{i,j} = \frac{u_{i,j+1}-2u_{i,j}+u_{i,j-1}}{(\Delta y)^2}$

Table 1.1: Common finite-difference (FD) schemes and their expressions. Adapted from Anderson [16].

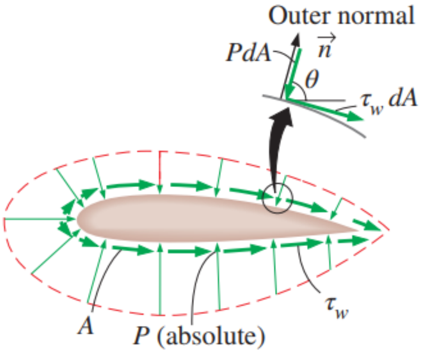

Figure 1.13: The pressure and viscous forces acting on a 2D body like an airfoil. Adapted from Cengel [49].

is often what engineers are most interested in knowing. The component of the resultant force that acts in the flow direction is called **drag force**, F_D, and the component of the resultant force that acts perpendicular to the flow direction is called the **lift force**, F_L (see Fig. 1.12). For three-dimensional flows, there is an additional side force component. We will only discuss two-dimensional flows here.

Refer to Fig. 1.13. It shows pressure and shear forces acting on a differential area dA of an airfoil surface. The relations for differential drag force and lift force acting on dA in this two-dimensional flow can be derived from the figure,

$$dF_D = -P \, dA \, \cos\theta + \tau_w \, dA \, \sin\theta \tag{1.56}$$

and

$$dF_L = -P \, dA \, \sin\theta - \tau_w \, dA \, \cos\theta \tag{1.57}$$

where θ is the angle that the outer normal of dA makes with the positive flow direction. The total drag and lift forces on the body can be determined by integrating the above equations over the entire surface of the body:

$$F_D = \int_A dF_D = \int_A (-P\cos\theta + \tau_w \sin\theta) \, dA \tag{1.58}$$

and

$$F_L = \int_A dF_L = \int_A (-P\sin\theta - \tau_w \cos\theta)\, dA \tag{1.59}$$

Equations (1.56) and (1.57) show that, in general, both the wall shear and pressure contribute to the drag and the lift. For illustrative purposes, let us briefly consider a thin flat plate placed in a fluid. There are two special cases to note in regards to the orientation of the thin plate with respect to the flow. The first case is when the thin flat plate is aligned exactly parallel to the flow direction. In this case, the drag force depends on the wall shear only and is independent of pressure. The second case is when the flat plate is placed normal to the flow. Now the drag force depends on the pressure only and is independent of wall shear. If the flat plate is tilted at an angle relative to the incoming flow, then the drag force depends on both the pressure and the shear stress—like for an airfoil.

Drag and lift forces depend on many factors such as the density ρ of the fluid, the upstream velocity V, and the size, shape, and orientation of the body. Because of this, it is more practical to use dimensionless numbers that represent the drag and lift characteristics of a body. These numbers are the **drag coefficient** C_D and the **lift coefficient** C_F, defined respectively as:

$$C_D = \frac{F_D}{\frac{1}{2}\rho V^2 A} \tag{1.60}$$

$$C_L = \frac{F_L}{\frac{1}{2}\rho V^2 A} \tag{1.61}$$

where A is typically the frontal area of the body, the area projected on a plane normal to the direction of flow. In drag and lift calculations of airfoils, A is taken to be the planform area. This is the area a person sees when looking at the airfoil from above in a direction normal to the body. The local drag and lift coefficients typically vary along the surface of a body due to changes in the velocity boundary layer in the flow direction. Scientists are usually more interested in the drag and lift over the entire surface, which can be determined using the *average* drag and lift coefficients. The equations relating local drag and lift coefficients (identified with a subscript x) to average drag and lift coefficients for a surface of length L are

$$C_D = \frac{1}{L}\int_0^L C_{D,\,x}\,dx \tag{1.62}$$

and

$$C_L = \frac{1}{L}\int_0^L C_{L,\,x}\,dx \tag{1.63}$$

More generally, if the local friction coefficient $C_{f,\,x}$ along a surface is known, the average friction coefficient for the entire surface can be determined by integration as

$$C_f = \frac{1}{L}\int_0^L C_{f,\,x}\,dx \tag{1.64}$$

For a flat plate, the friction coefficient for laminar flow can be determined theoretically by solving the conservation of mass and linear momentum equations numerically. For turbulent flow, however, the friction coefficient must be determined experimentally. The boundary layer thickness and the local friction coefficient at a location x along the plate for laminar flow are related by

$$\textit{Laminar}: \qquad \delta = \frac{4.91x}{{Re_x}^{1/2}} \quad \text{and} \quad C_{f,\,x} = \frac{0.664}{{Re_x}^{1/2}} \qquad Re_x \lesssim 5\times 10^5 \tag{1.65}$$

The corresponding relations for turbulent flow are

$$\textit{Turbulent}: \qquad \delta = \frac{0.38x}{{Re_x}^{1/5}} \quad \text{and} \quad C_{f,\,x} = \frac{0.059}{{Re_x}^{1/5}} \qquad 5\times 10^5 \lesssim Re_x \lesssim 10^7 \tag{1.66}$$

From the above relations, one can deduce that the local friction coefficient is directly proportional to the height of the boundary layer at a given location x along the plate:

$$C_{f,\,x} \sim \delta \tag{1.67}$$

1.9.1 Friction and Pressure Drag

Recall that drag is the net force exerted by a fluid on a body in the direction of the flow due to the combined effects of pressure forces and wall shear forces. It is beneficial to isolate and study the two effects separately because any reduction in one effect reduces the overall drag. This is always desirable in applications of the automobile, submarine, and aircraft industry.

Skin friction drag (or just *friction drag* $F_{D,\text{ friction}}$) is the part of drag due directly to the wall shear stress τ_w[16]. It is caused by friction effects. The part of drag that is due directly to pressure P is called the **pressure drag** (also referred to as *form drag* because of its strong dependence on the form or shape of the body). The friction and pressure drag coefficients are defined as

$$C_{D,\text{ friction}} = \frac{F_{D,\text{ friction}}}{\frac{1}{2}\rho V^2 A} \qquad \text{and} \qquad C_{D,\text{ pressure}} = \frac{F_{D,\text{ pressure}}}{\frac{1}{2}\rho V^2 A} \tag{1.68}$$

For the same area A, the total drag coefficient or drag force is simply their sum,

$$C_D = C_{D,\text{ friction}} + C_{D,\text{ pressure}} \qquad \text{and} \qquad F_D = F_{D,\text{ friction}} + F_{D,\text{ pressure}} \tag{1.69}$$

Friction drag depends on the orientation of a body relative to the fluid flow. It is zero for a flat surface placed perpendicular to the flow and is maximum for a flat surface placed parallel to the flow. In addition, friction drag increases with increasing viscosity. Since the Reynolds number is inversely proportional to the viscosity of the fluid, this implies that the contribution of friction drag to total drag for blunt bodies is less at higher Reynolds number and may be negligible at very high Reynolds numbers. At low Reynolds number, it turns out that most drag is due to friction drag for highly streamlined bodies like airfoils. Friction drag is also proportional to the surface area of a body. This is why large commercial airplanes have retractable wing extensions to reduce the total surface area of the plane, thereby reducing drag to save fuel.

Pressure drag is proportional to frontal area and to the *difference* between the pressures acting on the front and back of the immersed body. It is responsible for most of the total drag for blunt bodies. For streamlined bodies like airfoils, the pressure drag is small. The pressure drag is most substantial when the velocity of the fluid is too great for the fluid to be able to follow the curvature of the body. In this situation, the fluid separates from the

---

[16] The wall shear stress is defined for a Newtonian fluid as $\tau_w = \mu(\partial u/\partial y)_{y=0}$.

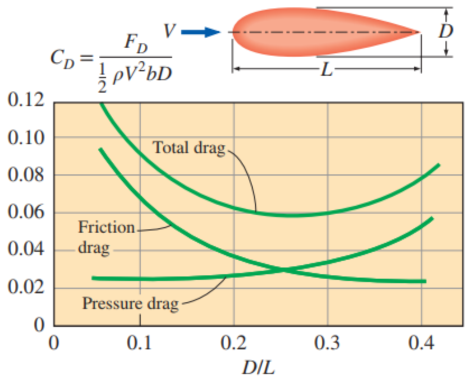

Figure 1.14: Variation of friction, pressure, and total drag coefficient of a 2D streamlined strut with respect to thickness-to-chord length ratio for Re $= 4 \times 10^4$. Image from Cengel [49].

body at some location and creates a very low pressure region in the back of the body. The large pressure difference that results between the front and back sides of the body is what is responsible for the pressure drag in this case.

Streamlining a body has obvious advantages for objects like cars and airplane wings, but there is more to the story. Streamlining has opposite effects on pressure and friction drag forces. While it decreases pressure drag by delaying boundary layer separation (thereby reducing the pressure difference between the front and back of the body), the streamlining procedure also increases the friction drag because the body's surface area is greater. The end result depends on which effect wins over the other. Consequently, to reduce the drag of a body requires that we consider both effects and figure out how to minimize the *sum* of the two. Figure 1.14 shows the variation of friction, pressure, and total drag coefficient of a 2D streamlined strut with respect to thickness-to-chord length ratio for Re $= 4 \times 10^4$. For airfoils and other thin bodies, C_D is based on planform area bL rather than frontal area bD, where b is the width of the 2D body into the page.

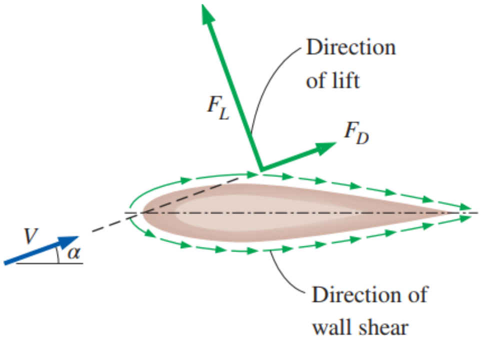

Figure 1.15: Viscous effects on lift for airfoils are usually negligible because wall shear is parallel to the surfaces and thus nearly perpendicular to the direction of lift. α represents the angle of attack and V is the free stream velocity of the fluid. Image from Cengel [49].

1.9.2 Lift

Recall that lift is the component of the net force (due to viscous and pressure forces) that is normal to the flow direction. For devices whose function is to generate lift such as airfoils, the lift can be approximated to be due entirely to the pressure distribution on the surfaces of the body. Viscous effects on lift are usually negligible when the body is streamlined since the wall shear acts parallel to the surfaces of the body, nearly perpendicular to the direction of lift (Fig. 1.15).

The primary objective in the design of airfoils, then, is to minimize the average pressure at the upper surface while maximizing it at the lower surface. Bernoulli's equation, Eq. (1.14), tells us that this is synonymous to wanting higher velocity fluid flowing over the upper surface and lower velocity fluid over the bottom. This situation is exactly why using vortex generators and the extended concept of a vortex whip on airfoils is such a great idea. More on this later.

1.10 Introduction to Flow Control

Improving aerodynamic performance can be accomplished by two principal means: (1) by optimizing the design of vehicles; and (2) by controlling and optimizing the flow around vehicles. After a century of development of the modern aircraft, it has become more and more difficult to reduce drag and noise by optimizing aircraft design only. Flow control provides an approach to further improve aircraft performance.

Flow control refers to any attempt to introduce perturbations into a flow field to alter its original flow development. There are many reasons why one would want to control a flow, including to enhance lift on an airfoil, to reduce drag, and to suppress vibrations. The benefits of these desired goals can be tremendous, and a significant amount of data exists that confirm the effectiveness of flow control devices. For instance, it has been found that a 1% reduction in the cruise drag of a large passenger aircraft could lead to about 1600 kilograms reduction of airplane empty weight or an increase of about 10 more passengers [39]. In particular, a 1% drag reduction is equivalent to saving 57,000 liters of aviation fuel for a Boeing 737 and 380,000 liters for a Boeing 747 per year [27]. Thus, flow control has attracted much attention by many research institutions. Many significant research projects have been conducted to advance the understanding and applications of flow control.

1.10.1 Classification of Flow Control Techniques

Many different techniques are applied to implement flow control. One way to classify these flow control techniques is shown in Fig. 1.16. In general, flow control can be broadly identified as either passive control or active control. Passive control techniques require no energy input. They are easy to implement, but the outcome cannot be changed during the control process. They function by extending surfaces into the flow to augment the primary flow characteristics. In addition to low operating and maintenance costs, passive enhancement methods can also be easily integrated into any existing manufacturing process. Active control techniques, however, do require energy input. They usually rely on flow pulsations, electromagnetic

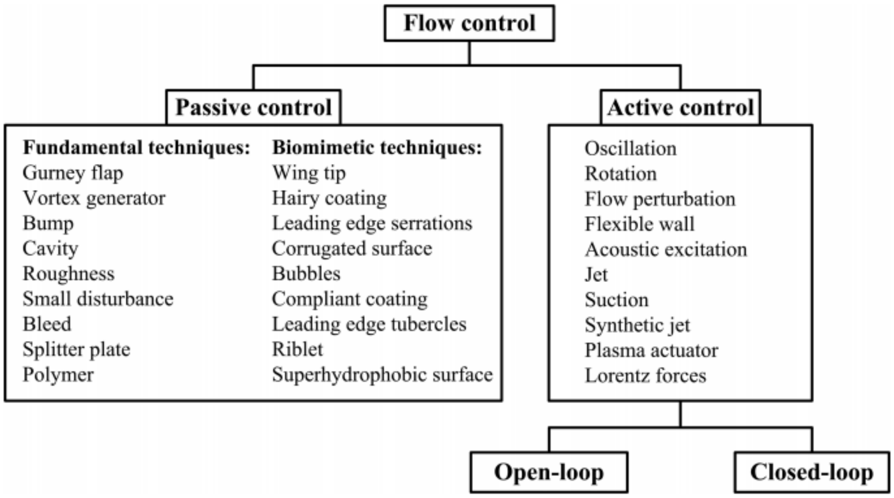

Figure 1.16: Categorization of flow control techniques. Image from Wang [51].

fields, or jet injection to provide mechanical mixing. Furthermore, the outcome can be adjusted during the control process. In this thesis, we only concentrate on passive flow control techniques.

Under passive control, we can further distinguish passive control techniques based on their origin. Passive techniques developed based on an understanding of flow physics belong to the fundamental techniques group. In comparison, the biomimetic techniques group describes passive techniques derived from nature—from animals and plants. Through the process of natural selection, living organisms developed their own shapes and organs with specific features that help them survive in certain environments. By mimicking these features in man-made systems, humans can take advantage of the results of millions of years of evolution. The most important passive control device relevant to this research is the vortex generator. More details about how vortex generators work will be explained in the next section.

1.11 Vortex Generators

A vortex generator (VG) is a passive flow control device used to manage flow separation through the introduction of a streamwise vortex. This vortex is created by placing a VG on

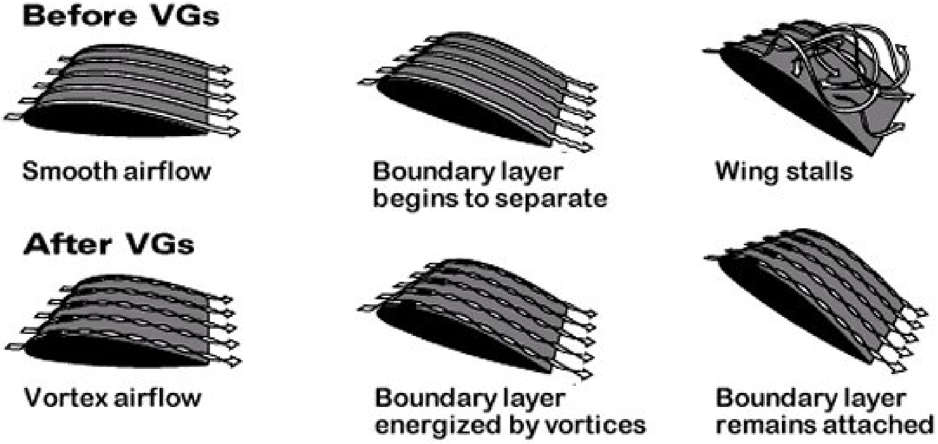

Figure 1.17: Benefits of using vortex generators on airfoils to delay flow separation and wing stall. Image from [37].

the surface of an entity whose flow field we wish to control. The strength of the vortices a VG creates is proportional to its angle of attack relative to the incoming flow. It is also possible to achieve a proportionate vortex strength by adjusting the VG chord. A VG is typically designed to be comparable in height to the local boundary layer height for flow moving over the surface of interest. Due to the pressure differences between the two sides of the VG and its finite height, the incoming boundary layer rolls up into a single streamwise vortex downstream. This allows high-momentum fluid in the outer flow to be drawn into the lower-momentum boundary layer. The resulting transfer of momentum makes the boundary layer more resistant to flow reversal in adverse pressure gradients. This method of flow control has proven to be effective in the presence of flow separation (e.g. at high angles of attack). However, due to the nature of a passive flow control device, an associated drag penalty is always present.

Figure 1.17 compares how air flows over an airfoil before VGs are installed and after VGs are installed. During takeoff and landing, planes generally operate at high angles of attack and relatively low speeds. These conditions can cause the flow of air around the wings to become erratic, leading to early separation and thus increased drag, indirectly causing the loss of lift as well. The powerful vortices that VGs create help mitigate the erratic flow behaviour by speeding up the flow of air close to the wings. The flow of air now has more energy to maintain its motion over the surface of the wings, resulting in higher lift due to a decrease in pressure on the upper surface of the airfoil compared to without VGs at the low speeds characteristic of takeoff and landing. Devices like vortex generators make it possible for planes to take off and land at lower speeds and in shorter distances than would be feasible without them. Flying at lower speeds improves passenger safety. Shorter distances needed for takeoff and landing maneuvers allow planes to operate with less runway [37].

Vortex generators come in many designs and shapes. Conventional VGs are shaped like vanes or wedges and protrude into the flow. There are four main types of conventional vortex generators: 1) vanes and airfoils, 2) ramps and wedges, 3) slots and jets, 4) steps, channels, and grooves. Figure 1.18 shows the basic shapes of the vane vortex generators that are most commonly used. Figure 1.19 shows the general shape of wedge (also known as "wheeler") and ramp vortex generators. It turns out that slot and jet vortex generators as well as steps, channels, and groove vortex generators are inferior to the other designs.

Other VG designs are shown in Fig. 1.20. Some of these designs will be discussed in the "Literature Review" section, so please refer back to this page for reference if the need arises.

Vortex generators are often arranged in a row along the spanwise direction in two configurations, shown in Fig. 1.21. When two VGs are arranged in the same direction, they produce co-rotating vortices. When the VGs are arranged in opposite directions, they produce counter-rotating vortices. These vortices are observed to persist far downstream of the vortex generators and dissipate slowly due to their interaction with the boundary layer.

Depending upon the height of the undisturbed boundary layer, vortex generators can be classified as micro- or macro-vortex generators. If the height of the undisturbed boundary layer is higher than the VG, then that particular configuration is a micro-vortex generator. Similarly, if the height of the vortex generator is higher than the undisturbed boundary layer, then the configuration is called a macro-vortex generator. Macro-vortex generators are

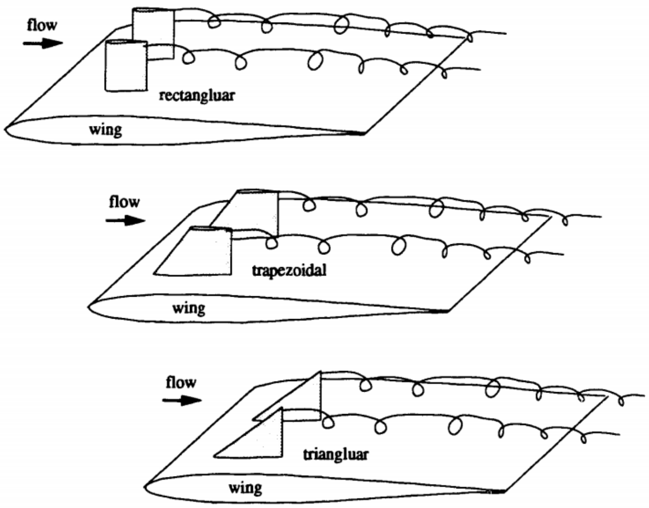

Figure 1.18: Various configurations of vane vortex generators. Image from Barrett [15].

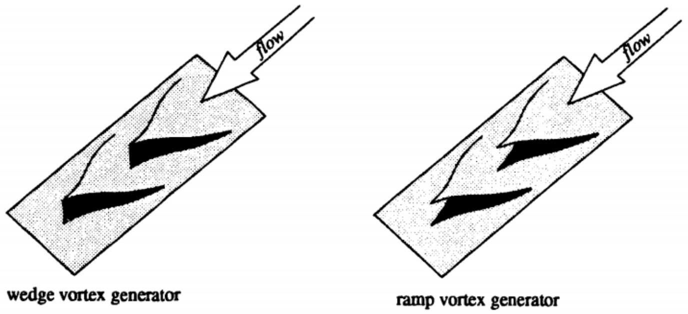

Figure 1.19: Wedge and ramp type vortex generators. Image from Barrett [15].

commonly used for heat transfer enhancements while micro-vortex generators are commonly used for flow separation delay.

1.12 Literature Review of Vortex Generators

Vortex generators were designed in 1947 by H. D. Taylor [1] in the form of small lifting surfaces that were applied normal to wind-tunnel diffuser walls to reduce separation losses. Schubauer and Spangenberg [2] studied forced mixing of boundary layers using different

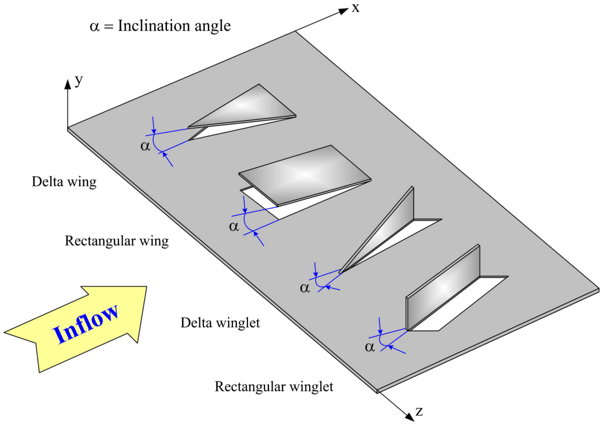

Figure 1.20: Schematic diagram of other types of VGs. Image from Skullong [48].

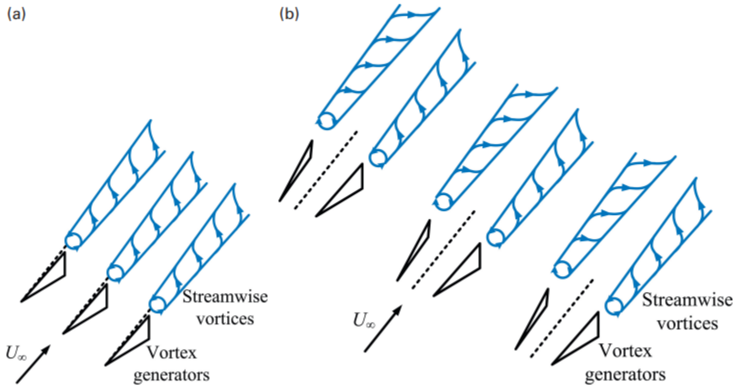

Figure 1.21: Vortex generators aligned (a) in the same direction produce co-rotating vortices, and (b) in opposite directions produce counter-rotating vortices. Image from Wang [51].

types of generators. They concluded that forced mixing has essentially the same effect on the boundary layer as a general reduction in pressure gradient. Brown *et al.* [4] used rectangular-vane type VGs with 1.2δ to improve the performance of subsonic diffusers. A study by Pearcey [3] represented the first systematic attempt to understand and optimize the performance of vortex generators. The design rules he came up with for preventing flow separation in high speed flows were based on measurement of mean streamwise velocities for different strengths and positions of vortex arrays, including both counter-rotating and co-rotating vortices. These design rules specified what the minimum pair separation should be, optimum ratios of generator spacing to generator height, and optimum aspect ratio and angle of attack for vortex generators. Unfortunately, many of these results turned out to be inaccurate due to inadequate understanding of the secondary flows present in the vicinity of the vortices. Nevertheless, his work pioneered subsequent research into understanding and optimizing vortex generator configurations for practical applications.

Since then, VGs have been the subject of extensive experimental and numerical investigations in both internal and external flows. Internal flows refer to flows in inlet ducts and diffusers. Here, VGs are used to prevent flow separation and reduce total pressure distortion. Most of the time, however, VGs are used in external flow applications such as on airfoils. In this case, the VGs are used to delay flow separation over a surface in order to indirectly enhance lift. This is achieved by controlling the boundary layer by redirecting the outer flow towards the wall using the streamwise vortices created by vortex generators [2].

Even though VGs are efficient at transporting high-momentum fluid from the free stream towards the lower-momentum region near the wall, there is always some amount of parasitic drag associated with them. In an effort to reduce this drag while still improving aerodynamic efficiency, different heights of VGs were studied. Bragg and Gregorek showed that vortex generators can increase the lift and reduce the drag of airfoils [6]. This reduction in drag was also found by others, such as Kerho *et al.* [14]. In the late 1980s, Rao and Kariya performed a comparative study of submerged and vane VGs in controlling the separation of a flat-plate turbulent boundary layer entering a region of steep adverse pressure gradient [7]. Different configurations were tested with a VG height h on the order of 60% of the boundary layer thickness δ. It was reported that the smaller VGs were most effective in a counter-rotating configuration, and even smaller sizes should be investigated. Lin *et al.* showed that a VG with a height of 10% the boundary layer thickness was as effective as conventional vane-type VGs with a height an order-of-magnitude higher at controlling turbulent flow separation [8]. By comparing small submerged vortex generators with different heights, they concluded that the vortex generator with $h/\delta \approx 0.8$ provided the largest pressure recovery but was associated with the largest device-drag penalty. Meanwhile, at smaller device height, the one with $h/\delta \approx 0.1$ performed as well as the larger one with $h/\delta \approx 0.4$. They also suggested the vortex generators be placed no more than 2δ upstream of the baseline separation position [9, 10].

In a study the following year, Lin and his collaborators compared several devices for controlling turbulent separated flow at low speeds, including VGs, and reported that transferring momentum from the outer region of a turbulent boundary layer by embedded streamwise vortices was more effective than by transverse vortices for separation control applications [11]. Sub-boundary layer VGs mounted on a multi-element airfoil in a landing configuration have also been shown to substantially increase the lift-to-drag ratio for a given angle of attack [17]. Klausmeyer *et al.* also applied VGs on multi-element airfoils and studied their effects [19]. The effectiveness of using micro-vortex generators was again reaffirmed years later in 1999 with Lin's synopsis of flow separation control using micro-vortex generators and their advantages for high-lift application. Lin reviewed the studies on low-profile vortex generators to control boundary layer separation, and concluded that, when flow-separation locations are fixed and when the generators are placed within $100h$ upstream of the baseline separation, the low-profile vortex generators with $0.1 \leq h/\delta \leq 0.5$ can be as effective as conventional ones with height greater or equal to the boundary layer thickness [20]. Other applications to flow control over a back-facing ramp include the works of Gardarin *et al.* [38] and Serakawi and Ahmad [43].

Several years later, Jenkins *et al.* evaluated the effectiveness of several active and passive devices to control flow using surface static pressures, flow visualization, and 3D Stereo Digital Particle Image Velocimetry. They found that micro-vortex generators were very effective in controlling the flow environment for an adverse pressure gradient [23].

In a detailed parametric study of triangular passive vortex generators, Godard and Stanislas showed that arranging the VGs in a counter-rotating configuration was more effective than a co-rotating one. They also found that the optimum skew angle is around 18° and that the VGs aspect ratio (l/h) is not very sensitive in the range tested but recommended to be at least 2 [25].

A comprehensive review of past work on vortex generators with particular relevance to heat exchange enhancement was conducted by Jacobi and Shah [18]. Ahmed *et al.* provided a more recent review of this field [44]. Fiebig *et al.* [12] studied triangular and rectangular longitudinal vortex generators formed by punching small pieces out of flat plate fins so that they stuck out of the plates at a certain angle of attack relative to the main flow—a developing laminar channel flow. They found that the heat transfer enhancement per unit vortex generator area was highest for delta wings followed by delta winglets and delta winglet pairs. The performance of rectangular wings and rectangular winglets were much less effective. Drag induced by the VGs was found to be proportional to the projected area and independent of the shape.

Tiggelbeck *et al.* [13] investigated flow structure, heat transfer, and drag due to longitudinal vortices created by double rows of delta winglets in transition channel flow. They looked at aligned and staggered double-row configurations of delta winglet pairs. Aligned delta winglet double rows showed higher heat transfer enhancement than staggered ones. They also reported that the wake flow structure strongly depends on the flow Reynolds number and the angle of attack of the VG. For really high angles of attack, vortices did not form downstream of the VG. The critical angle above which vortices do not form is approximately 70 degrees.

Gentry and Jacobi [21] performed studies on heat transfer enhancement by placing delta-wing vortex generators on a flat plate. Their data suggested a 50% to 60% enhancement of average heat and mass transfer at low Reynolds numbers. A general design guideline for optimal delta-wing VG geometries they stated in their paper was to place the VGs in such a fashion so that streamwise vortices are strong and near the edge of the boundary layer. In a later study, Gentry and Jacobi [24] performed vortex measurements to measure the strength of the longitudinal vortices produced and found that it increases with Reynolds number, aspect ratio, and angle of attack. They also observed that vortex strength decays as vortices get carried downstream.

Sohankar used large-eddy simulations (LES) and Direct Numerical Simulations (DNS) to study unsteady flow and heat transfer for a channel with two angled ribs as a vee-shaped vortex generator. The study found that flow and heat transfer became steady at lower Reynolds numbers while they were unsteady at higher Reynolds number. Furthermore, the results showed that the pressure coefficient, bulk temperature, and friction factor changed significantly with increasing Reynolds number and angle of attack. These changes were brought about by horse-shoe and longitudinal vortices generated by the VG [28].

Inspired by group locomotion of animals in nature as observed in bird migration, He *et al.* explored a new vortex generator array deployed in a "V" designed to create constructive interference between vortices. The array consisted of two delta-winglet pairs placed at an angle of attack of 10° or 30°. It was found that the 30° array performed better at heat enhancement than the former, with a 25%-55% increase in the average heat transfer.

Fiebig [22] conducted a survey on delta and rectangular vortex generators and their associated vortices and heat transfer characteristics in flat plate boundary layers. Some of the main conclusions include longitudinal vortices outperform transverse vortices when it comes to enhancing heat transfer, and heat transfer enhancement is higher in laminar flow than in turbulent flow. Abdollahi and Shams [31] performed a three-dimensional numerical simulation to study the effects of shape and angle of attack of the winglet vortex generator on heat transfer and flow characteristics in a rectangular heat sink. They used the Pareto optimal strategy in order to find optimal values of parameters that achieve maximum heat transfer enhancement and minimum pressure drop. Salviano *et al.* [32] used two different approaches for optimizing the position and angles of a vortex generator: Response Surface Methodology (RSM) and Direct Optimization (DO). It was shown that DO resulted in a better performance than RSM for all objective functions considered in the study. An additional input variable, roll angle, was also proposed and shown to be an important parameter in VG design optimization.

Javier and Parviz [33] performed direct numerical simulations of unsteady channel flow at low and moderate Reynolds numbers to study near-wall turbulence. They intentionally selected a small enough computational domain in order to isolate the basic flow unit to study its morphology and dynamics, and evaluate its contribution to turbulence in fully developed channels. They found that the thin layers of spanwise vorticity is lifted away from the wall and the intermittent regeneration of turbulence consisted of the wrapping of the wall-layer vorticity around a single inclined longitudinal vortex. Ashilf *et al.* showed that vortex circulation increases with an increase in vortex generator height [34]. But the circulation reaches a convergent value, which was consequently nearly independent of the VG height. Marshall [35] carried out a computational study examining the unsteady cross-stream vorticity structures that form when one or more streamwise vortices are immersed in boundary-layer flows. He used a model with vanishing gradients in the streamwise direction, a quasi-2D approach. He reported that at sufficiently high Reynolds numbers, the cross-stream vorticity sheets formed near the wall are ejected outward and wrap around the vortices.

Wendt [36] performed a detailed parametric study of vortices shed from the tips of airfoil vortex generators and found that the Lamb (ideal viscous) vortex model gives excellent qualitative agreement with the observed behavior of low-aspect ratio airfoils. He also observed that circulation and peak vorticity are proportional to the freestream Mach number, the angle of attack of the vortex generator, and the VG span-to-boundary-layer-thickness ratio. Seshagiri *et al.* [40] tested various arrangements of vortex generators to investigate their control effects on an airfoil at low Reynolds numbers. Jukes and Choi [45] studied the formation of streamwise vortices created by plasma vortex generators and found that these vortices were similar to those produced by delta-shaped, vane-type vortex generators. The main difference was the enhanced circulation by the addition of vorticity in the plasma jet. They also observed that the plasma vortex had greater wall-ward entrainment which leads to a stronger downwash.

Up to date, vortex generators have already been applied in many different fields for flow control, ranging from low-speed to high-speed fields. A review was recently conducted by Lu *et al.* [42].

1.13 Vortex Whip

The concept of a "vortex whip" refers to an idea to improve the performance of vortex generators in inhibiting boundary layer separation. If we can delay when fluid separates from the surface of a body, we can reduce the drag on the body because the wake which forms behind the body has been effectively diminished. To implement a vortex whip, an array of vortices of progressively decreasing strengths is set up (either by using VGs, created in simulation using the Biot-Savart law, or by other means), all initially the same distance above a flat plate. In this dissertation, the array is taken to be composed of three point vortices created spontaneously in simulation. There is nothing magical about this number. Pairs of VGs have already been studied quite extensively in the literature, and from the Biot-Savart law, we know three vortices are better than two because the additional third vortex will contribute to a greater induced velocity under the right conditions. We also know that VGs have an associated drag penalty when they are used, so the more VGs we use, the greater the drag. Hence the array of vortices should not include too many vortices. Finally, for a fixed distance, the greater the number of vortices in an array, the closer they would have to be relative to one another. The closer vortices get together, the greater the instabilities are. Thus an array of three vortices is a judicious choice in a pioneering study. The strongest vortex induces the next weaker one toward the surface, and it induces the next weakest one even closer to the surface. If all the vortices originated at the edge of the boundary layer, then they would tend to carry high-momentum fluid toward the surface, thereby inhibiting separation.

The best way to assess how much better a vortex whip performs compared to a standard VG array is to measure its performance in a lab. This is a great topic to explore for future researchers. Recall that even a small improvement of 1% in drag reduction can have immense consequence in terms of fuel savings [27].

There are two versions of the vortex whip problem: the 2D version and the 3D version. In both problems, the central theme is to consider many different configurations and arrangements of the vortices so that we can narrow in on the near optimal configuration of vortices that will most effectively send the weakest vortex as close to the surface as possible and stay there for as long as possible. There are important differences between the two problems, however. In the 2D problem, the initial distance of all three vortices above the wall is not a parameter since there is no boundary layer for potential flow problems. Thus the parameter space to explore in searching for a local optimum is smaller than the 3D case. It is important to also point out that in the 2D problem, no explicit vortex generators are modeled or simulated. Rather, the vortices that would be created by vortex generators are simulated directly themselves. In the 3D problem, the arrangement of vortices is replaced by actual VGs placed at different angles of attack (AOA) relative to the incoming flow. By placing the VGs at different angles relative to the flow, each VG creates a vortex whose strength is dependent upon the VG's angle of attack (and the VG's height above the boundary layer to some extent). Furthermore, the 3D problem does take into account viscosity and the presence of a boundary layer. There are more parameters in the parameter space to search for a local optimum as well.

It was realized that attacking the 3D vortex whip problem head-on was like shooting darts in the dark. The vast parameter space that one would need to investigate in order to find a near optimal configuration of VGs was an obvious challenge, but the real and inevitable hurdle one faced was the intense computation involved. Solving the 3D vortex whip problem using direct numerical simulation via CFD software requires an extremely fine mesh to calculate the dynamics correctly due to the scale of the problem. At a Reynolds number of approximately 500, it is estimated that a typical simulation could take at least three months to complete on a supercomputer, and that is just one simulation. Many simulations are required to gather enough data points to just even get a glimpse of where the local minimum could be. If there was a mistake in the code somewhere, one would have to wait at least three months after the results come back to find out!

Because of these difficulties associated with the 3D vortex whip problem, it is believed that the most reasonable thing to do is to the solve the 2D vortex whip problem first. Solving the 2D problem will contribute significant insights into the 3D problem. These insights can narrow down the parameter space one should investigate in the 3D problem, therefore eliminating the need to look in places that we know will not work. Make no mistake, the 2D vortex whip is a challenging problem in its own right, featuring a large parameter space in and of itself.

1.14 Research Objectives and Significance

Most of the previous work on vortex generators up to this point have focused on studying the behavior of a single VG or an array of VGs in some fixed, symmetrical arrangement. A few design optimization studies can also be found, but a quantitative description of how induced vortices interact with the boundary layer is still lacking. Hence the vortex whip is a relatively novel construct and very little is known about it according to the author's knowledge.

This thesis deals with the 2D problem. Instead of using actual, physical VGs to create vortices, we will program the vortex cores directly in computer simulations. We wish to implement a code that calculates the vortex trajectories of an array of three point vortices of progressively decreasing strengths under potential flow conditions. Calculating these vortex trajectories will be key to answering deeper and more interesting questions about vortex whip dynamics.

As explained in the previous section, there is the 2D vortex whip problem and there is the 3D one. This dissertation serves as a significant stepping stone for investigating the behavior of the three-dimensional vortex whip, whether that might be through direct numerical simulation at low Reynolds number or through experimentation in a wind tunnel. By considering many different configurations and arrangements of three vortices on a flat surface, the objective of this research is to find a near optimal configuration of vortices that will most effectively serve as a vortex whip in order to send the weakest vortex closest to the wall as possible and stay there for as long as possible. What this behavior imitates is the transfer of high-momentum fluid to the bottom of the boundary layer, thereby inhibiting flow separation. In addition, this research seeks to answer the following questions:

1. What happens when we vary the inter-separation distances of the vortices?
2. What happens when we vary the relative strengths of the vortices?
3. What are the vortex trajectories and how do we get the smallest primary vortex closest to the wall for the longest time?
4. Is there only one local minimum for the optimal configuration, or are there many depending on certain factors?
5. If so, what are those factors?

The 2D simulations conducted in this thesis are really meant to provide guidance for solving the viscous, 3D case. Ultimately, the significance of this project and the fundamental physics studied has important implications for controlling drag and airflow separation using vortex generators, with direct applications to improving lift of aircraft and turbine power output. Simulations, computations, and analysis will be performed predominantly using the Python programming language.

1.15 Organization of Dissertation

This thesis is divided into five chapters. Chapter 1 (Introduction) lays the ground work for the rest of the thesis, giving a brief overview of essential concepts needed to understand the research. In Chapter 2 (The 2D Vortex Whip), the two-dimensional vortex whip problem is explained in full detail. This chapter also talks about how the code was implemented and designed to model the dynamics of the vortex whip. In addition, an optimization strategy is laid out and many initial test runs are performed to gain further insight into how a vortex whip behaves. In Chapter 3 (Results and Discussion), the results of over 7980 simulations performed for this dissertation will be discussed and analyzed. These results will be extended in Chapter 4 (Extension of the Results) by comparing them to findings from an additional 7980 simulations. Finally, in Chapter 5 (Conclusions), some concluding remarks are made and suggestions are offered for future work.

Chapter 2

THE 2D VORTEX WHIP

This chapter describes the 2D vortex whip problem in full detail. We begin with the method of images, then proceed to explaining how the code that models the dynamics of the 2D vortex whip was implemented and the various considerations that went into its design. Then we proceed to a discussion of the important dimensionless parameters of the problem. An optimization strategy is subsequently laid out that is intended to narrow down the immense parameter space of the 2D vortex whip problem. Insights gained from these preliminary investigations are summarized and synthesized into a set of guidelines that ultimately drive the search for a local optimum configuration for the 2D vortex whip.

A brief discussion of the naming conventions that will be used for the remainder of the thesis is in order at this point. In addition to referring to the array of vortices of progressively increasing strengths as the weakest vortex, intermediate vortex, and strongest vortex, we will also use the convention that Baby Bear (BB) refers to the weakest vortex, Mama Bear (MB) refers to the intermediate strength vortex, and Papa Bear (PB) refers to the strongest vortex. These conventions will save us a lot of typing without loss of specificity as well as give us a varied vocabulary to refer to the same thing.

2.1 Code Design and Implementation

We begin this chapter by describing the method of images then move on to explain some of the considerations and challenges that went into writing the code that simulates a 2D vortex whip.

In order to simulate flow along a horizontal wall for a set of three vortices, the method of images is used. The basic idea behind the method of images is to simulate the presence of a wall by placing a real vortex above an imaginary line—this is the wall we are simulating—and an image vortex of opposite strength at a mirror position below its real vortex counterpart. The method of images works for the following reason. If a vortex is placed near a wall, we know that the flow pattern will be distorted. Imagine placing a vortex at $y = y_{source}$ next to a wall at $y = 0$. The boundary condition at the wall requires the flow to be tangent there. By placing an image vortex of opposite strength—but equal in magnitude—to the real vortex at $y = -y_{source}$, we can achieve the same effect in simulation as having a real physical wall.

Recall that all three vortices in a vortex whip induce velocities V on each other according to the Biot-Savart law:

$$V = \frac{\Gamma}{2\pi r}, \tag{2.1}$$

where Γ is the strength of the vortex and r is the separation distance from the vortex center. In Cartesian coordinates, the velocity components are given by [50]:

$$u(x, y) = \frac{\Gamma}{2\pi} \frac{x - x_{source}}{(x - x_{source})^2 + (y - y_{source})^2} \tag{2.2}$$

$$v(x, y) = \frac{\Gamma}{2\pi} \frac{y - y_{source}}{(x - x_{source})^2 + (y - y_{source})^2} \tag{2.3}$$

The induced velocity vector is perpendicular to the separation vector. It is important to also note that a vortex cannot induce any velocity on itself.

The trajectories of the point vortices can be computed at least two ways. The first way is to multiply their velocities by a small time interval Δt to get their displacements, and then recalculate their new induced velocities from their new positions. The procedure is then repeated for any desired length of time. This is also known as the Euler method. Another way is to use the powerful integration routines available in the SciPy library to integrate the induced velocities forward in time. Specifically, the SciPy library has a function called odeint which integrates a system of ordinary different equations for a specified sequence of time points. The second way is the chosen method in this thesis because it proved to be more reliable when put through the two test cases to be described shortly.

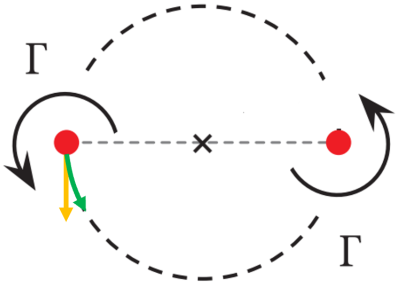

Figure 2.1: To correct for a numerical artifact, vortices should be made to move along a chord line (green path) rather than a tangent line (orange path). Shown here are two vortices of the same strength and same sense of rotation. The vortex on the right should induce the vortex on the left to follow the green path rather than the orange path in one time step. Distances have been exaggerated for clarity. Image modified from Leweke [47].

A subtle numerical trick is required when implementing the dynamics of the three vortices. Because the induced velocity is perpendicular to the radius vector, after the next time step Δt, the new computed radius vector will tend to be a little longer. For example, consider two identical vortices of the same sign of rotation. In the case of inviscid flow, they should rotate about each other forever at constant separation, conserving energy. However, without compensating for the numerical artifact that tends to increase the radius vector with finite Δt, their calculated separation will tend to grow. The vortices should move along chord lines rather than tangent lines in the calculations (see Fig. 2.1). A good test of a numerical scheme that implements the dynamics of the vortex whip is to try this vortex pair test.

Another test to see if the code is working properly is to consider the case of two vortices of the same strength, but opposite sense of rotation. In principle, we expect the two vortices to move downwards while maintaining a constant separation.

These two test cases will be used not only to test the validity of the code, but also to calibrate the numerical errors associated with choosing specific values of Δt and how long the simulation runs for. The value of Δt used in the simulation will undoubtedly affect the accuracy of the results, since it is expected that a smaller Δt should increase the numerical accuracy. This comes at a price, obviously, and that is increased computation time per simulation. Furthermore, we would have to run the simulation for a longer period of time to capture any interesting behavior if each time step is so small. The objective, then, is to use a Δt suitable enough that we have results we can trust without having to use such a long simulation window. There are disadvantages for running a simulation for too long, the most prominent being the continued accumulation of numerical errors the longer the code runs. More on choosing Δt will be discussed in later sections.

An important issue to consider is how to deal with the smallest vertical position achievable by the weakest vortex. As the real vortex comes closer and closer to the wall, a consequence of the method of images is that its image vortex will also come closer and closer to the wall. The influence of the image vortex grows stronger on the real vortex, but in real life, the image vortex should have never been there in the first place; it was only used as a trick to simulate the presence of a physical wall! Hence very close to the wall, the simulation yields nonphysical results. This problem is addressed by using a threshold value to assess whether the weakest vortex was able to come close to the wall or not. It was arbitrarily decided to claim that a given configuration of three vortices succeeded in bringing the weakest vortex close to the wall if the weakest vortex crosses a line that is $0.1H$; that is, 10% of its initial height H above the wall.

Using this threshold of $0.1H$, what distinguishes two configurations, then, if both configurations lead to the weakest vortex crossing this line? The answer is how fast the weakest vortex crosses this line *and* how long it stays below the line[1].

2.1.1 Anatomy of a Typical Simulation Run Image

Figure 2.2 labels many of the naming conventions used in this thesis. Recall that BB is shorthand for Baby Bear, which is the weakest vortex with strength Γ_1. MB is shorthand for

---

[1] We will occasionally refer to the time BB spends below the threshold line as its residence time.

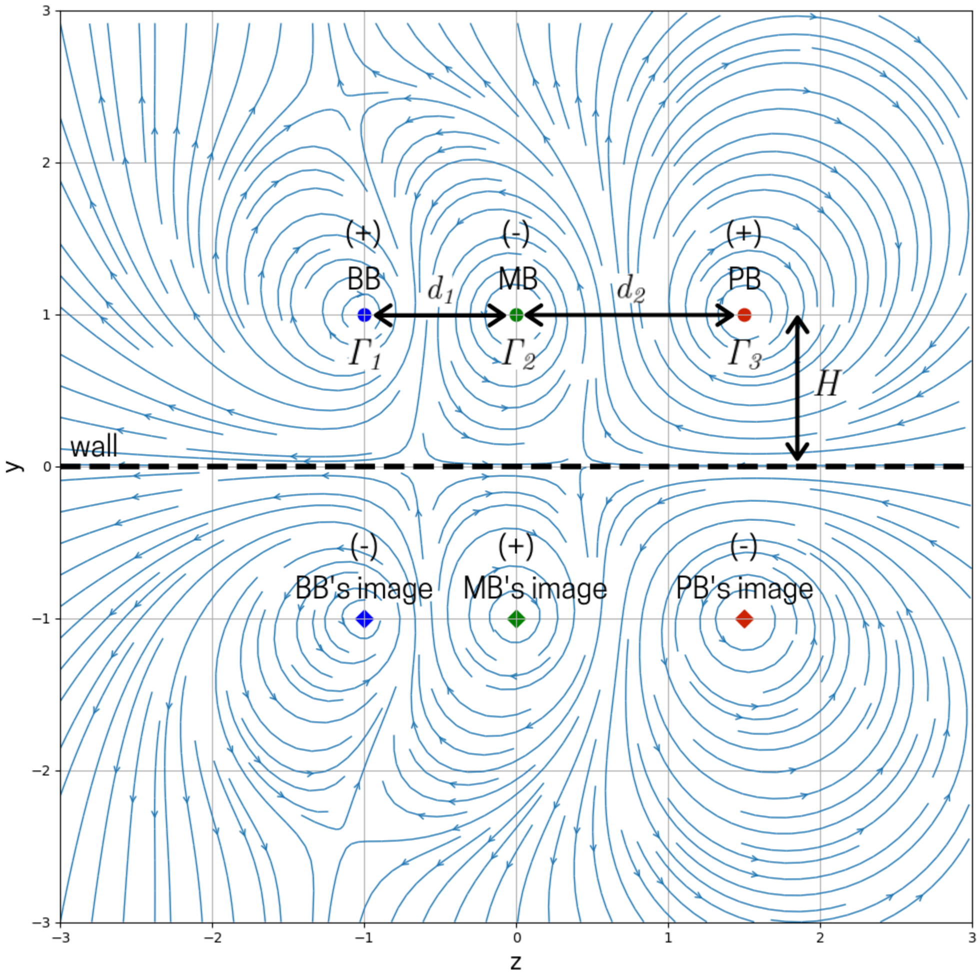

Figure 2.2: Naming conventions used in this thesis for a typical simulation run. Please refer to the text for a more detailed description of all the labels.

Mama Bear, which is the intermediate strength vortex with strength Γ_2. PB is shorthand for Papa Bear, which is the strongest vortex with strength Γ_3. The strength values are always chosen such that $\Gamma_1 < \Gamma_2 < \Gamma_3$. d_1 is the separation distance between BB and MB. d_2 is the separation distance between MB and PB. Finally, H^2 is the height of each vortex above the wall, represented by the thick dashed black line at $y = 0$. All vortices always start at the

---

[2] We will be using H and H_0 interchangeably to refer to the initial height of each vortex above the wall.

same initial height H above the wall.

To help track the movements of BB, MB, and PB, each vortex has been color-coded. Red is used to label PB, green is used to label MB, and blue is used to label BB. Furthermore, a real vortex is marked with a filled-in circle, whereas an image vortex is marked with a filled-in diamond. The starting positions of all three vortices will always be displayed on a figure such as this to allow for easy comparison of how the vortices moved over time.

A vortex can have either a positive sense of rotation or a negative sense of rotation. A (+) symbol is placed above BB to show that it has a positive sense of rotation, which physically means that it is rotating clockwise (CW). A (–) symbol is placed above MB to that that it has a negative sense of rotation, which physically means that it is rotating counter-clockwise (CCW).

Since the method of images is used to simulate flow near a wall, each vortex has a corresponding image vortex in a mirror position below the wall, as can be seen on the bottom half of Figure 2.2. Each image vortex has the same strength as its real counterpart, but the opposite sense of rotation.

2.2 Normalization and Dimensionless Variables

Having established the labels and conventions used, let us now take a moment to discuss the variables in more detail and various dimensionless parameters we can construct that will be useful to our work. One of the most important quantities we want to measure is BB's lowest height above the wall. We will use H, the initial height of each vortex above the wall, to normalize measurements of BB's vertical position. H is the characteristic height of a 2D vortex array configuration. For simplicity, we set $H = 1.0$ and keep it constant for all simulation runs.

From H and the vortex strength Γ, we can define a characteristic time for a given 2D vortex whip configuration:

$$t_0 = \frac{H^2}{\Gamma}$$

But there are three possible values of Γ, one for each vortex, so which one do we use? Although there is some degree of arbitrariness, it was decided to define the characteristic time as

$$t_0 = \frac{H^2}{\Gamma_3} \tag{2.4}$$

motivated by the fact that $\Gamma_1 < \Gamma_2 < \Gamma_3$ so that Eq. (2.4) yields the smallest time scale.

For every simulation run, a finite time step Δt must be chosen as well as the total number of iterations[3] (or frames). This "computer time" will be normalized by the characteristic time we defined in Eq. (2.4).

From d_1, d_2, and H, several possible dimensionless parameters that we can construct are:

$$\frac{d_1}{d_2}, \frac{d_2}{d_1}, \frac{d_1}{H}, \frac{d_2}{H}$$

For reasons to be revealed later in this thesis, it was decided to use $\frac{d_1}{H}$ and $\frac{d_2}{H}$.

Finally, we can construct several possible dimensionless parameters from Γ_1, Γ_2, and Γ_3:

$$\frac{\Gamma_2}{\Gamma_1}, \frac{\Gamma_3}{\Gamma_2}$$

These two combinations are the most relevant to the thesis. Recall that there is a condition imposed on the strengths in a vortex whip: $\Gamma_1 < \Gamma_2 < \Gamma_3$. For the remainder of the thesis, it is also imposed that

$$\frac{\Gamma_2}{\Gamma_1} = \frac{\Gamma_3}{\Gamma_2}$$

This assumption helps narrow the parameter space we have to search. The more general case,

$$\frac{\Gamma_2}{\Gamma_1} \neq \frac{\Gamma_3}{\Gamma_2}$$

is a possible extension to this work in future studies.

---

[3] In this thesis, the number of iterations is also referred to as the number of frames.

2.3 Optimization Strategy

In the 2D vortex whip, the relevant parameters that can be varied are:

1. sense of rotation;
2. strength of rotation;
3. separation distance between Baby Bear and Mama Bear; and
4. separation distance between Mama Bear and Papa Bear.

To iterate through all four of the above parameters in order to search for a local extrema is an extremely time-consuming and daunting computing task. Furthermore, approaching the problem from such a brute-force approach of grinding through all of the possible combinations of the parameter space is ineffective, since some parameters should not work at all no matter how we try to optimize them in relation to the other parameters. The sensible and more practical thing to do, then, is to build some physical intuition on what parameters will work better than others from the outset, before performing an intensive dive into the large parameter space. In other words, the strategy is to narrow down the possible ranges of values each parameter in the list above can take *before* we iterate over many combinations.

In the following sections, we will explore how changing one of the above parameters at a time—while holding all of the others fixed—affects the weakest vortex. Recall that the goal is to send the weakest vortex as close to the wall as possible. As explained above, due to the accumulation of numerical errors and the difficulties encountered when a vortex and its image come closer and closer together, a threshold of $0.1H$ is arbitrarily used as a measure of success. In addition to achieving a minimum distance above the wall, we are also interested in two other factors: (1) how *fast* the weakest vortex reaches this minimal distance; and (2) how *long* it stays below the threshold. All of these factors, taken together, will allow us to crown two champions at the end of the thesis. The first champion is the configuration that sends the weakest vortex as close to the wall as possible and as fast as possible. The second champion is the configuration that sends that weakest vortex as close to the wall as possible and stays there for as long as possible.

2.4 The End Goals: Contour Plots of Minimum Heights and Residence Times

The goals of the thesis have already been laid out. What is uncertain at this point, however, is what the solution for the local optimum looks like. Perhaps there is no one single answer. What if there are multiple configurations that are effective at sending the weakest vortex closest to the wall? Or perhaps, what if the local optimal configuration depends on certain conditions? These are all valid possibilities that we have to be aware of.

At the end of the day, we want to have as detailed of a picture of the potential solution(s) as we can possibly get. To this end, the end goals of this thesis are two kinds of contour plots. The first contour plot is a plot of BB's minimum height above the wall, with $\frac{d_1}{H}$ on the y-axis and $\frac{\Gamma_2}{\Gamma_1}$ on the x-axis. The second contour plot is a plot of how long BB stayed below the threshold line after it crosses it, with the same set of axes. This second plot gives us additional information about the configurations, and will help further narrow down the local optimum or optima.

It was mentioned in the "Normalization and Dimensionless Parameters" section that we will be using $\frac{d_1}{H}$ and $\frac{d_2}{H}$ in this thesis. Here we elaborate more on these parameters. The first dimensionless parameter, $\frac{d_1}{H}$, is used for the contour plots we wish to obtain from the results of simulations, as described above. The second dimensionless parameter, $\frac{d_2}{H}$, is held fixed for each contour plot of $\frac{d_1}{H}$ versus $\frac{\Gamma_2}{\Gamma_1}$. It might turn out what the same value of the ratio $\frac{d_1}{d_2}$ can lead to entirely different outcomes, depending on whether we adjust d_1 or d_2. By obtaining contour plots of $\frac{d_1}{H}$ versus $\frac{\Gamma_2}{\Gamma_1}$ for several values of $\frac{d_2}{H}$, we can detect if there is any sensitivity of a configuration to the separation between MB and PB (the d_2 variable).

2.5 Calibration

Before we start varying each of the parameters in our parameter space individually to get a sense of their influence on the weakest vortex, it is necessary to choose an acceptable Δt and the number of frames for each simulation. It is not necessary to obtain extremely accurate results at this point, since the goal is simply to build physical intuition about which configurations should not work, thereby helping us narrow down the parameter space we have to investigate later. Choosing $\Delta t = 1.0$ and number of frames to be 25, we will run the code for the two test cases of two vortices of equal and opposite strengths. This section summarizes the results of these calibration tests.

For all of the calibration tests performed in this dissertation, it is expected that the separation distance between the two vortices remain nearly the same at the beginning and at the end of the simulation run. A percentage error of more than 10 percent is deemed unacceptable for these tests. This percentage is commonly used to assess variation between experimental and CFD simulation results.

The code will be validated in the following manner. We set BB's strength to be equal to PB, and set MB's strength equal to 0. The initial height H of all of the real vortices is set to a very large value (we used $H = 1e6$) so that the image vortices are so far away from their real counterparts that they practically do not induce any appreciable velocity on any of the real vortices. With these settings, the written code should produce the behavior that is expected for two vortices of the equal and opposite strengths. The results of these tests will be demonstrated in the following sections.

2.5.1 Two Vortices of Equal Strength

For this test, BB is assigned a strength of 10, MB is assigned a strength of 0, and PB is assigned a strength of 10. This setup essentially mimics only having two vortices. BB is positioned at $(z, y) = (-1.0, 1.0e6)$, MB at $(0.0, 1.0e6)$, and PB at $(1.0, 1.0e6)$. This way, the influence of the image vortices on the real vortices is negligible. The separation distance between BB and PB is 2.0. Using $\Delta t = 1.0$ and number of frames to be 25 for this configuration produces Figure 2.3. Recall that the starting positions of each vortex is always included in a static snapshot of the simulation such as this one to reference how the vortices moved.

Figure 2.4 shows a graph of BB's normalized height above the wall versus the normalized time. The captions in this figure indicate that the time taken to reach the $0.1H^4$ threshold line (horizontal dashed line in magenta color) is infinity, which means that BB never crossed the threshold line in the entire duration of the simulation. Another caption on the figure states that the time spent below the $0.1H$ line is 0.0, which is indeed true since it did not spend any time below the line at all during the time scale of the simulation.

We know that BB and PB are initially 2.0 units apart. With $\Delta t = 1.0$ and the number of frames set to 25, at the end of the simulation run, the separation distance is calculated to be 2.002348953304673. The associated percentage error is about 0.114% (0.1135067925% to be exact). This is definitely acceptable for the purposes of rough runs in order to build physical intuition on how the array of vortices interact.

Using the Euler method, at the end of the simulation, the separation distance is determined to be 2.002348953304673. The percentage error is about 0.117% (0.1174476652% to be exact). Because of this slightly larger error, the SciPy function odeint was adopted to calculate the trajectories of the vortices.

These results validate that the written code is working properly since the separation distance is close to 2.0 at the beginning and end of the simulation.

Before we proceed to the rough performance runs, let us run the code on one more test case to see how the choice of $\Delta t = 1.0$ and number of frames set to 25 hold up.

---

[4] Recall that H and H_0 are used interchangeably in this thesis to refer to the initial of all vortices above the wall.

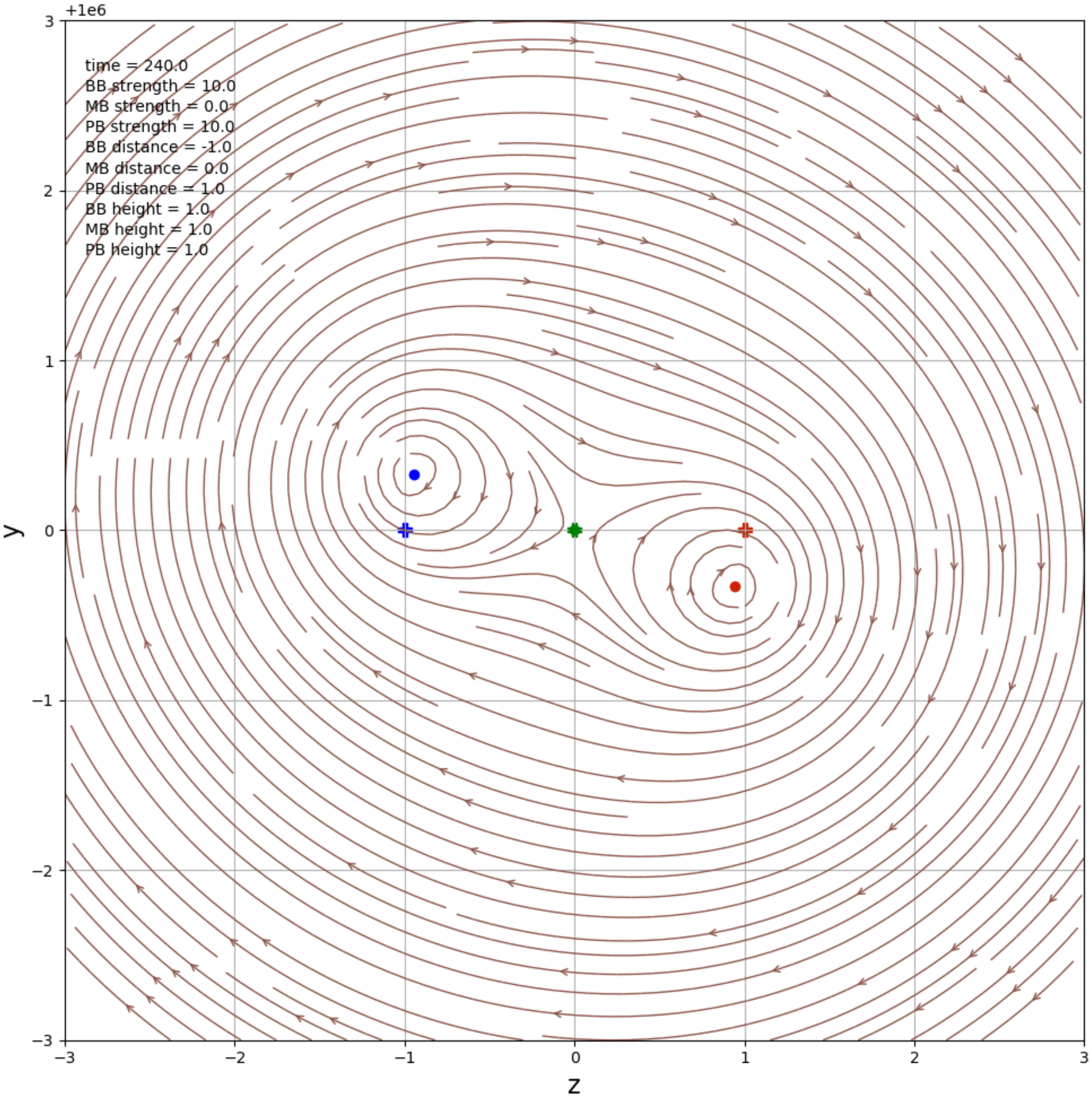

Figure 2.3: Calibration test for case of two vortices of same strength, with $H = 1e6$. Notice that the BB (blue circle) and PB (red circle) rotate about each other about the central point, which in this case is the location of MB (the green dot). This behavior is exactly what we expect.

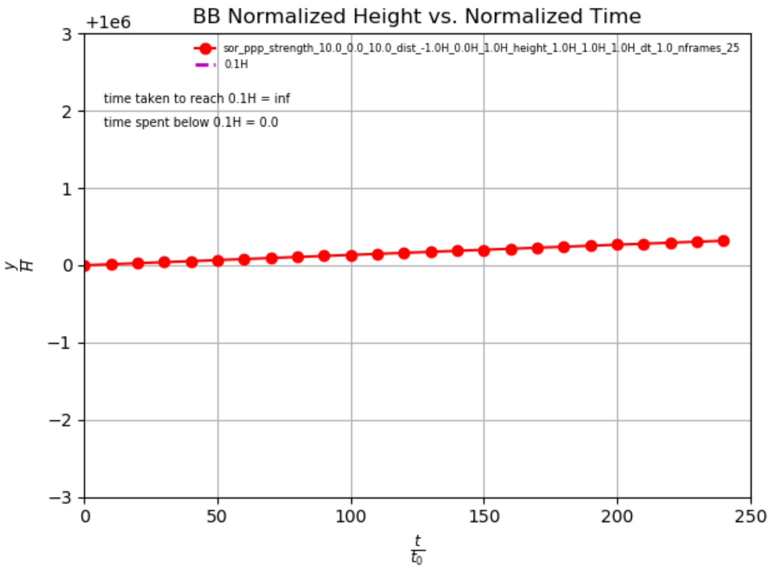

Figure 2.4: Calibration test for case of two vortices of same strength, with $H = 1e6$. Graph shows BB's normalized height above the surface versus the normalized time.

2.5.2 Two Vortices of Opposite Strength

For this test case, BB is assigned a strength of 10, MB is assigned a strength of 0, and PB is assigned a strength of -10. Again we are essentially setting up just two vortices. BB is positioned at $(z, y) = (-1.0, 1.0e6)$, MB at $(0.0, 1.0e6)$, and PB at $(1.0, 1.0e6)$. Thus the separation distance between BB and PB is 2.0. Using $\Delta t = 1.0$ and number of frames to be 25 again for this configuration produces Figure 2.5.

Figure 2.6 shows a graph of BB's normalized height above the wall versus the normalized time. We know that BB and PB are initially 2.0 units apart. With $\Delta t = 1.0$ and the number of frames set to 25, at the end of the simulation run, the separation distance is calculated to be 1.9977223659020882. The associated percentage error is about 0.113%. These calculations are very close to 2.0, a good indication of reliable accuracy. We expected the separation distance to be close to 2.0 at the beginning and end of the simulation.

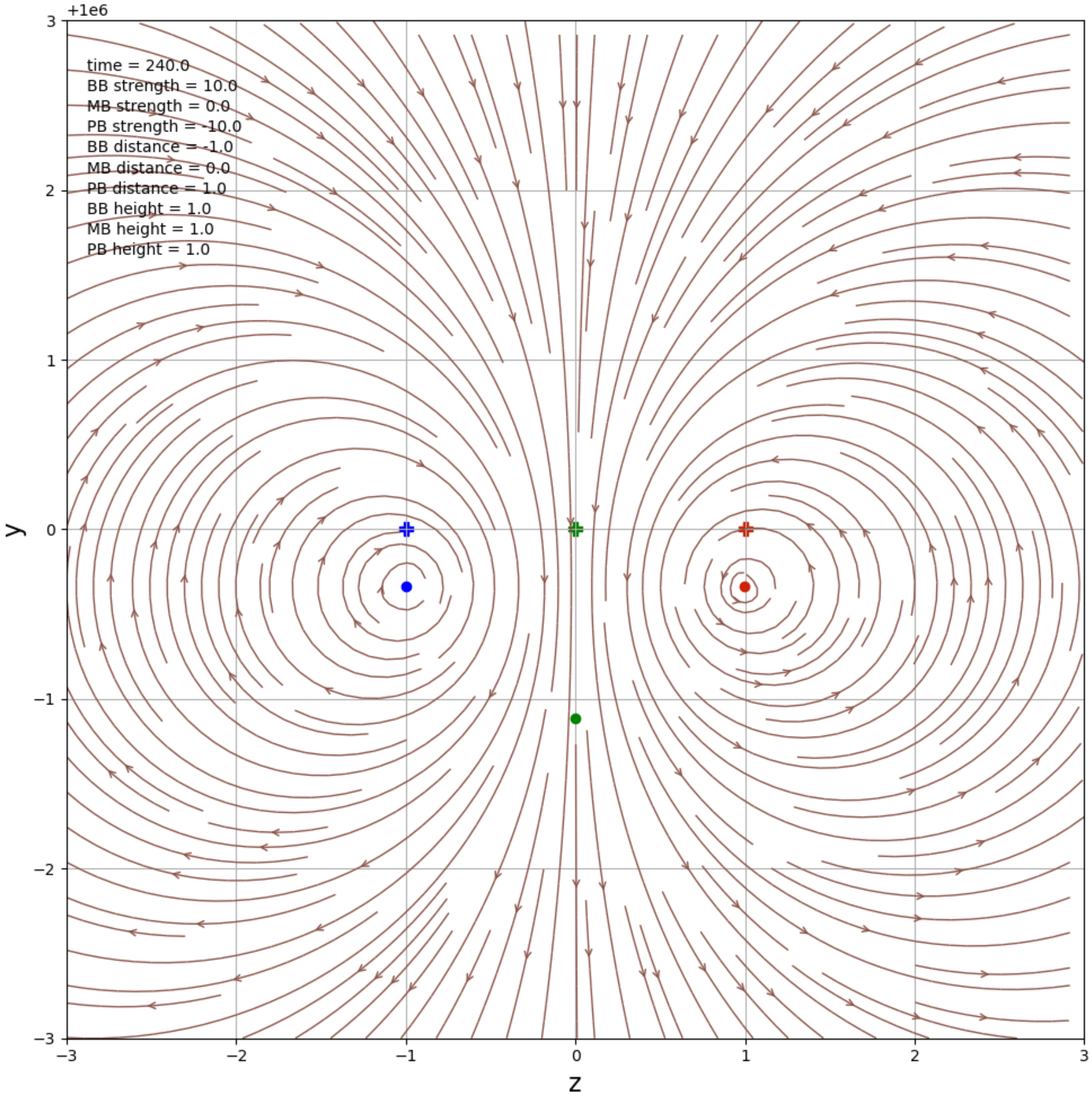

Figure 2.5: Calibration test for case of two vortices of opposite strength, with $H = 1e6$. Notice that the BB (blue circle) and PB (red circle) maintain a nearly constant separation as time progresses, exactly as we expect.

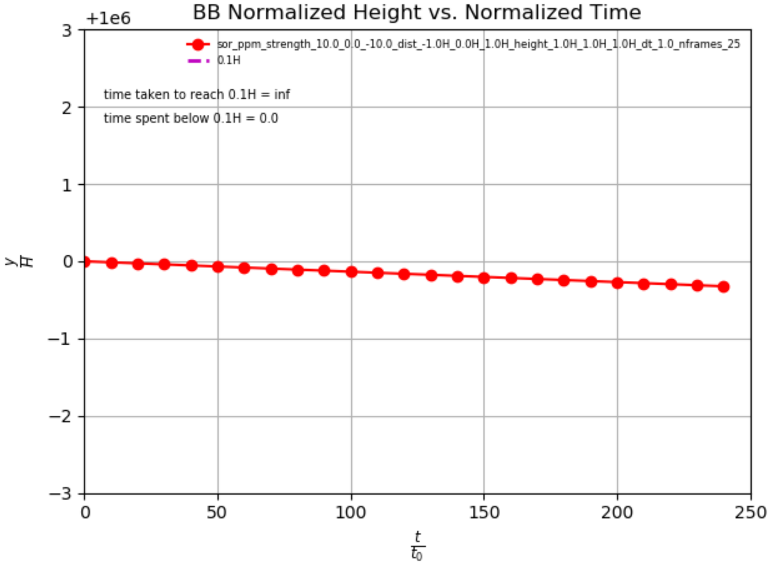

Figure 2.6: Calibration test for case of two vortices of opposite strength, with $H = 1e6$. Graph shows BB's normalized height above the surface versus the normalized time.

2.6 Vortex Sense of Rotation

The sense of rotation (SOR) of a vortex refers to which direction it is rotating. There are two possibilities for the 2D problem. A positive (+) sense of rotation designates that a vortex is rotating clockwise (CW), and a negative (–) sense of rotation designates that a vortex is rotating counter-clockwise (CCW). With an array of three vortices, (BB MB PB), there are eight total possible combinations for senses of rotation. This can be seen in Table 2.1, along with results of these simulation runs.

Table 2.1 tells us several things. One of the things it tells us is that there are four combinations of senses of rotation that will not work since they send BB upwards instead of downwards. These combinations are $(+ + +)$, $(+ - +)$, $(- + +)$, and $(- - +)$. This leaves four remaining combinations that are possible candidates worthy of further investigation. Upon closer inspection, however, even though $(+ + -)$ and $(- + -)$ send BB downwards,

BB	**MB**	**PB**	**BB up or down**	**Time taken to reach 0.1H**	**Time spent below 0.1H**
+	+	+	up	inf	0.0
+	+	−	down	inf	0.0
+	−	+	up	inf	0.0
+	−	−	down	363.9	636.1
−	+	+	up	inf	0.0
−	+	−	down	inf	0.0
−	−	+	up	inf	0.0
−	−	−	down	369.7	630.3

Table 2.1: All possible combinations of senses of rotation for an array of three vortices. BB=Baby Bear, MB=Mama Bear, PB=Papa Bear.

these combinations would require a much longer time to achieve the desired outcome. Of course, it is not surprising that the longer we wait and the more time we simulate for, these combinations will eventually succeed in sending BB downwards. But at this rough estimate stage, we can clearly rule these combinations out since there exists other combinations that do send BB close to the wall within the time frame used for these simulations. This leaves us with two very qualified candidates: $(+--)$ and $(---)$.

Of the remaining two possible combinations, the results appear to indicate that the combination $(+--)$ is the most effective at sending BB closest to the surface, while holding all other parameters fixed. This is based upon the time taken for BB to reach the $0.1H$ threshold line, as well as how long BB stayed below this line after it crossed it. Even though the times it takes BB to reach the $0.1H$ line for $(+--)$ and $(---)$ seem very close to each other, the difference is significant enough based on the calibration we obtained at the beginning.

Moving forward, we will use the $(+--)$ combination of senses of rotation for BB, MB, and PB, respectively, to search for the local extrema.

2.7 Vortex Strength

The vortex strength is the Γ term in the Biot-Savart law, $V = \frac{\Gamma}{2\pi r}$. In the following, Γ_1 refers to the strength of BB, Γ_2 is the vortex strength of MB, and Γ_3 is the vortex strength of PB. Recall that in a vortex whip, the array of three vortices have progressively increasing strengths; that is, $\Gamma_1 < \Gamma_2 < \Gamma_3$. As it stands, the previous inequality statement is too broad. In this thesis, the condition of the relative strengths of the vortices is further refined such that

$$\frac{\Gamma_2}{\Gamma_1} = \frac{\Gamma_3}{\Gamma_2} \tag{2.5}$$

The Biot-Savart law tells us that the greater the strength of a vortex, the greater the velocity it induces on another vortex because the induced velocity is proportional to the strength. After many trial runs with various baseline values for Γ_1 in conjunction with $\Delta t = 1.0$ and the number of frames equal to 25, it was finally decided that using $\Gamma_1 = 10.0$ induces the vortices to move fast enough to see results in the specified time frame. Table 2.2 summarizes the findings when varying only the strength ratio $\frac{\Gamma_2}{\Gamma_1}$ while keeping all other parameters fixed. The value of Γ_3 is chosen accordingly to maintain condition (2.5).

Based on Table 2.2, it is not surprising that the greater the strength ratio, the faster BB gets pulled downward to the surface. The reasonable thing to do in this case is to select a smaller range of strength ratios to investigate first to search for potential patterns, and extend the range if necessary.

Moving forward, we will use the range $1.1 \leq \frac{\Gamma_2}{\Gamma_1} = \frac{\Gamma_3}{\Gamma_2} \leq 3.0$ to probe the 2D vortex whip parameter space.

2.8 Separation Distance Between Baby Bear and Mama Bear

Let d_1 be the separation distance between BB and MB, and d_2 be the separation distance between MB and PB. In this section, we vary d_1 while holding all other parameters constant to see what effect it has on BB. Table 2.3 summarizes the results of these runs.

Γ_1	Γ_2	Γ_3	**Time taken to reach 0.1H**	**Time spent below 0.1H**
10.0	20.0	40.0	363.9	636.1
10.0	30.0	90.0	435.3	1814.7
10.0	40.0	160.0	478.6	3521.4
10.0	50.0	250.0	525.2	5724.8
10.0	60.0	369.0	622.3	8377.7
10.0	70.0	490.0	717.9	11532.1
10.0	80.0	640.0	576.0	15424.0

Table 2.2: Summary of simulation runs varying only the strength ratio such that $\frac{\Gamma_2}{\Gamma_1} = \frac{\Gamma_3}{\Gamma_2}$ and all other parameters are fixed.

BB zpos	**MB zpos**	**PB zpos**	**Time taken to reach 0.1H**	**Time spent below 0.1H**
-0.2	0.0	1.0	400.0	306.4
-0.3	0.0	1.0	276.9	1064.3
-0.4	0.0	1.0	242.9	2007.1
-0.5	0.0	1.0	269.9	1980.1
-0.6	0.0	1.0	312.4	1937.6
-0.8	0.0	1.0	378.0	1872.0
-1.0	0.0	1.0	435.3	1814.7
-1.6	0.0	1.0	603.0	1647.0
-2.0	0.0	1.0	706.1	1543.9
-3.0	0.0	1.0	953.0	1297.0

Table 2.3: Summary of simulation runs varying only the separation distance between BB and MB, d_1, while holding all other parameters fixed.

BB zpos	MB zpos	PB zpos	Time taken to reach 0.1H	Time spent below 0.1H
-1.0	0.0	0.2	335.8	532.7
-1.0	0.0	0.3	356.7	1893.3
-1.0	0.0	0.4	377.2	1872.8
-1.0	0.0	0.5	390.0	1860.0
-1.0	0.0	0.6	399.4	1850.6
-1.0	0.0	0.8	419.3	1830.7
-1.0	0.0	1.0	435.3	1814.7
-1.0	0.0	1.6	481.4	1768.6
-1.0	0.0	2.0	510.7	1739.3
-1.0	0.0	3.0	577.0	1673.0

Table 2.4: Summary of simulation runs varying only the separation distance between MB and PB, d_2, while holding all other parameters fixed.

According to the table, if we want to send BB to the surface as quickly as possible, a configuration where BB is placed too far away from MB is not effective. This is what we expect, since the influence of MB and PB on BB diminishes the further BB is away. Table 2.3 shows that placing BB at 0.4 leads to optimal performance in both columns 4 and 5. But before we decide what ranges to use for d_1, let us look at how varying the separation distance between MB and PB, d_2, affects the behavior of BB.

2.9 Separation Distance Between Mama Bear and Papa Bear

In this section, we vary d_2 while holding all other parameters constant to see what effect it has on BB. Table 2.4 summarizes the results of these runs.

Comparing Tables 2.3 and 2.4, notice that shorter time periods can be achieved in order to send BB to the wall if we vary BB's position (or equivalently, vary d_1) as compared to varying PB's position (varying d_2). The lowest times taken for BB to reach the $0.1H$

threshold line is in the 200s if we vary d_1, while the lowest times achieved by varying d_2 are in the 300s.

Moving forward, we will vary d_1 while keeping mostly d_2 constant. To be exact, we will vary $\frac{d_1}{H}$ for a given value of $\frac{d_2}{H}$. The range of $\frac{d_2}{H}$ we will consider is from 0.4 to 2.8.

2.10 Summary of Lessons Learned

In this section, we combine together in one place all of the lessons learned from running independent studies of each variable parameter by itself. It serves as a summary of the insights we have worked hard to gain to help guide the simulations we will perform.

These are the things we learned from implementing the optimization strategy:

1. The $(+--)$ combination of senses of rotation for BB, MB, and PB, respectively, is the most effective at sending BB to the wall compared to other possible combinations.

2. The greater the strength a vortex has, the more effective it is at inducing BB towards the wall. For practical reasons, we will restrict the range of our investigation to $1.1 \leq \frac{\Gamma_2}{\Gamma_1} = \frac{\Gamma_3}{\Gamma_2} \leq 3.0$.

3. Varying d_1 while holding d_2 fixed seems to be more effective than the other way around. Thus we will vary $\frac{d_1}{H}$ for a given value of $\frac{d_2}{H}$. We will investigate different values of $\frac{d_2}{H}$ for the same $\frac{d_1}{H}$ range.

Chapter 3

RESULTS AND DISCUSSION

In total, the author made over 16000 simulation attempts to numerically investigate the 2D problem. So many results had to be discarded due to bugs discovered later in the code, such as normalization mistakes, which required reruns of thousands of simulations. Although less than half of the total number of attempts resulted in valid results and will get time in the limelight in this chapter, all of the other unsuccessful attempts certainly paved the way for the successful completion of this dissertation.

In this chapter, the results of over 7980 simulations of different configurations of the 2D vortex whip synthesized into contour plots are presented and analyzed. All of the simulations were performed using a time step $\Delta t = 0.2$ and the number of total iterations set to 125. We begin by discussing the more thorough calibration tests performed before proceeding with the exhaustive search. Then we present the results and elaborate on the findings. Indeed, the search for a local optimum was quite intensive and tedious with such a large number of simulations performed. But it was all worth it because several profound discoveries have been unveiled!

3.1 Calibration

It is necessary to perform the same calibration tests as shown in Chapter 2, but this time with $\Delta t = 0.2$ and the number of frames for each simulation set to 125. We run the code for the two test cases of two vortices of equal and opposite strengths. The calibration done here is more thorough than before, however. This is because varying the strength of a vortex affects its dynamics, which inevitably affects how it interacts with other vortices. Since the strength of a vortex is allowed to vary from 10 to 90 in the planned simulations, calibration

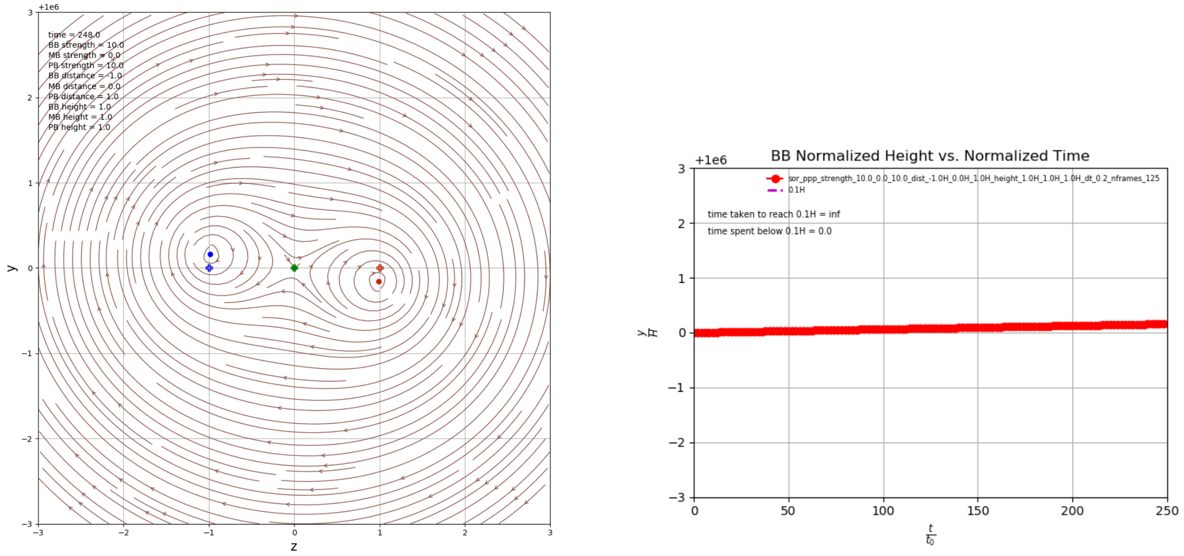

(a) (b)

Figure 3.1: Final calibration test for case of two vortices with same strength of 10. (a) Notice that the BB (blue circle) and PB (red circle) rotate about each other about the central point, which in this case is the location of MB (the green dot). This behavior is exactly what we expect. (b) Graph shows BB's normalized height above the surface versus the normalized time.

tests will be done for these extreme limits.

3.1.1 Two Vortices of Equal Strength

Strength of 10

For this test, BB is assigned a strength of 10, MB is assigned a strength of 0, and PB is assigned a strength of 10. Once again, we are essentially setting up an arrangement of just two vortices. BB is positioned at $(z, y) = (-1.0, 1.0e6)$, MB at $(0.0, 1.0e6)$, and PB at $(1.0, 1.0e6)$. Thus the separation distance between BB and PB is 2.0. Using $\Delta t = 0.2$ and number of frames to be 125, this configuration produces Fig. 3.1a.

It is important to point out that the trajectory of BB indicated by the red curve in Fig. 3.1b is actually composed of just points. The fact that it looks like a continuous line indicates that the time step we have chosen is sufficient enough to capture the important dynamics.

For compactness and since the calibration process was already explained in great detail in Chapter 2, the static image showing the final positions of all the vortices at the end of the simulation run is scaled down and shown alongside the graph of BB's trajectory over the duration of the simulation.

Figure 3.1b shows a graph of BB's normalized height above the wall versus the normalized time. The captions in this figure indicate that the time taken to reach the $0.1H$ threshold line (horizontal dashed line in magenta color) is infinity, which means that BB never crossed the threshold line in the entire duration of the simulation. Another caption on the figure states that the time spent below the $0.1H$ line is 0.0, which is indeed true since it did not spend any time below the line at all during the time scale of the simulation.

We know that BB and PB are initially 2.0 units apart. With $\Delta t = 0.2$ and the number of frames set to 125, at the end of the simulation run, we expect the separation distance between BB and PB to be nearly the same as at the beginning; the separation distance at the end is calculated to be 2.000102959560376. The associated percentage error is about 0.00515%. This is definitely good to have accuracy up to 3 decimal places.

Strength of 90

Keeping all other parameters the same, if we increase the strength to 90 now, Figs. 3.2a and 3.2b show what the code produces. Here again we can see a nice continuous line in Fig. 3.2b even though the curve is actually composed of just points.

Once more, BB and PB are initially 2.0 units apart. With $\Delta t = 0.2$ and the number of frames set to 125, at the end of the simulation run, the separation distance is calculated to be 2.0082883246796017. The associated percentage error is about 0.414%. The accuracy is reduced somewhat compared to when the strength is 10, but still acceptable.

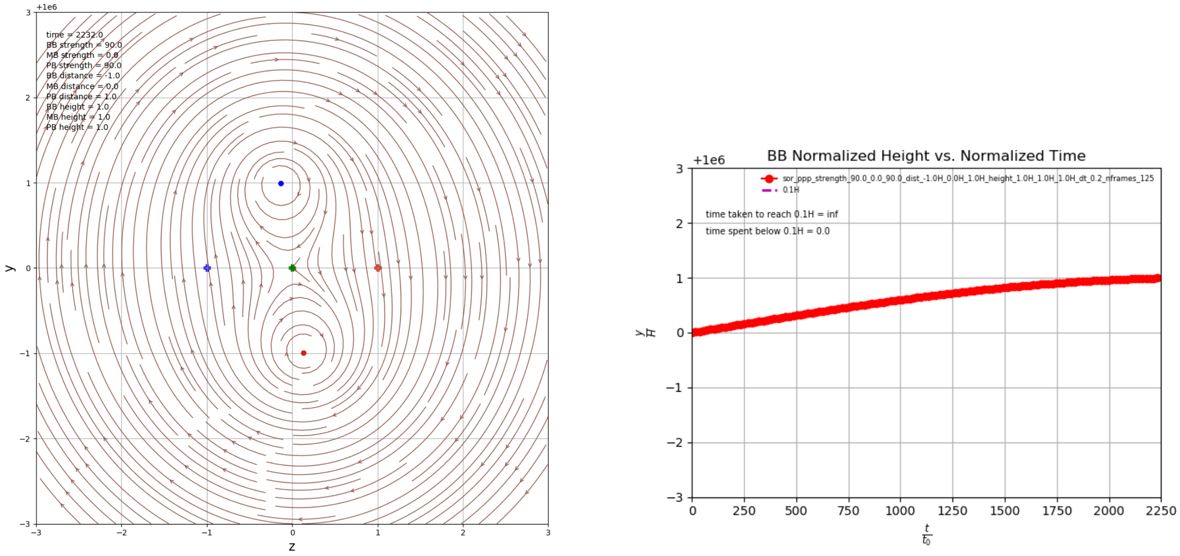

(a) (b)

Figure 3.2: Final calibration test for case of two vortices with same strength of 90. (a) Notice that the BB (blue circle) and PB (red circle) rotate about each other about the central point, which in this case is the location of MB (the green dot). This behavior is exactly what we expect. (b) Graph shows BB's normalized height above the surface versus the normalized time.

3.1.2 Two Vortices of Opposite Strength

Strength of 10

For this test case, BB is assigned a strength of 10, MB is assigned a strength of 0, and PB is assigned a strength of −10. We have set up our usual two active vortices. BB is positioned at $(z, y) = (-1.0, 1.0e6)$, MB at $(0.0, 1.0e6)$, and PB at $(1.0, 1.0e6)$. Thus the separation distance between BB and PB is 2.0. Using $\Delta t = 0.2$ and number of frames to be 125 for this configuration produces Fig. 3.3a.

Figure 3.3ab shows a graph of BB's normalized height above the wall versus the normalized time. We know that BB and PB are initially 2.0 units apart. With $\Delta t = 0.2$ and the

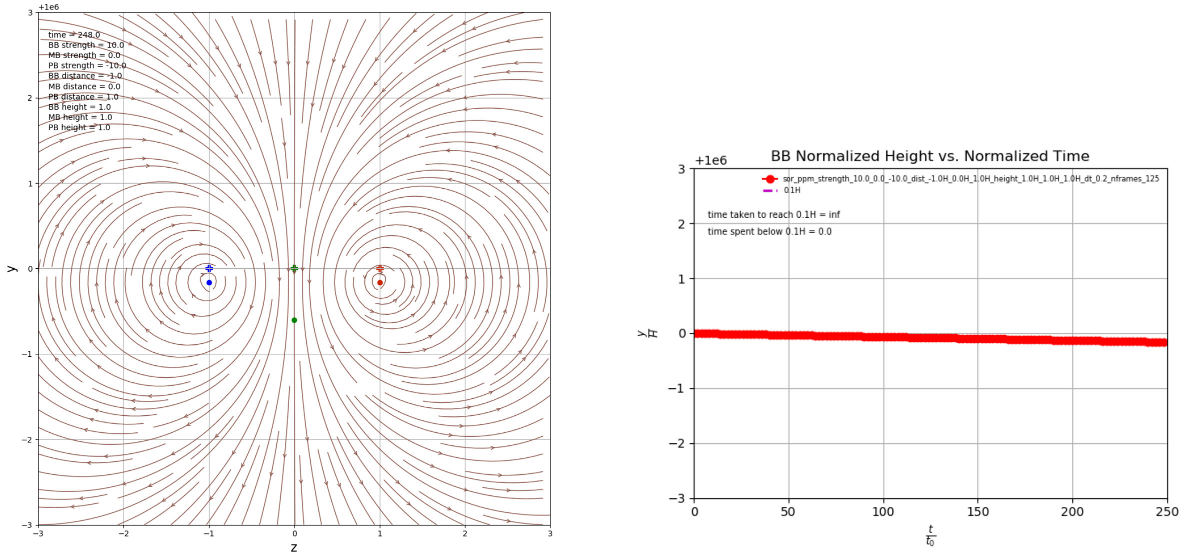

(a)

(b)

Figure 3.3: Final calibration test for case of two vortices with opposite strength of 10. (a) Notice that the BB (blue circle) and PB (red circle) maintain a nearly constant separation as time progresses, exactly as we expect. (b) Graph shows BB's normalized height above the surface versus the normalized time.

number of frames set to 125, at the end of the simulation run, the separation distance is calculated to be 1.9998970514932932. The associated percentage error is about 0.00515%. These calculations are very close to 2.0, a good indication of reliable accuracy.

Strength of 90

Keeping all other parameters the same, if we increase the strength to 90 now, Figs. 3.4a and 3.4b show what the code produces.

Once again, BB and PB are initially 2.0 units apart. With $\Delta t = 0.2$, the number of frames set to 125, and the strength set to 90, at the end of the simulation run, the separation distance is calculated to be 1.9916080760947357. The associated percentage error is about 0.420%.

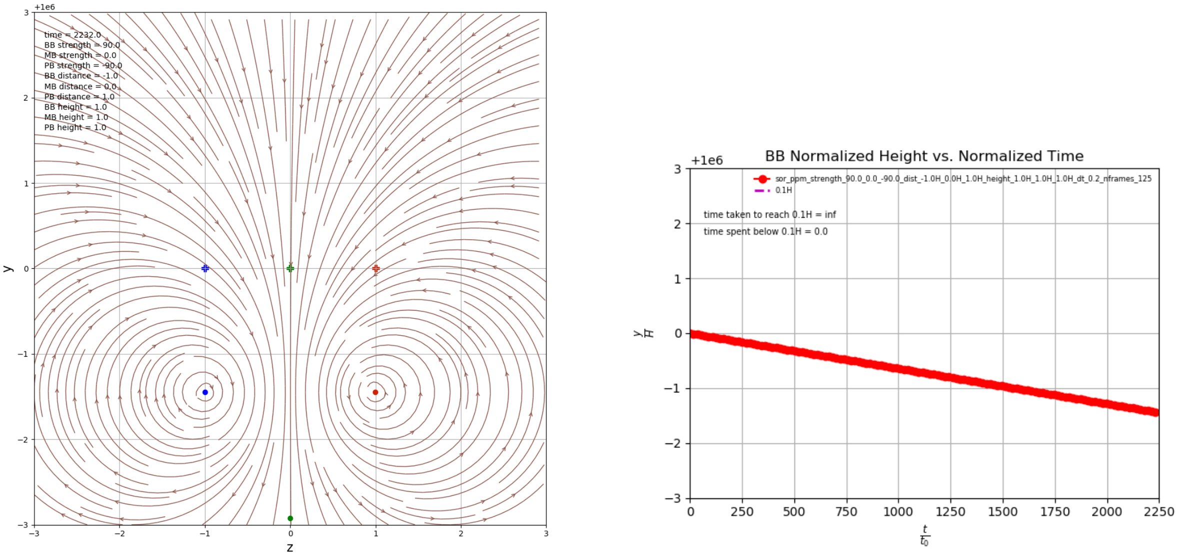

(a) (b)

Figure 3.4: Final calibration test for case of two vortices with opposite strength of 90. (a) Notice that the BB (blue circle) and PB (red circle) maintain a nearly constant separation as time progresses, exactly as we expect. (b) Graph shows BB's normalized height above the surface versus the normalized time.

The accuracy is reduced somewhat compared to when the strength is 10, but still acceptable.

The results from the two test cases of same strength vortices and opposite strength vortices give us confidence that using $\Delta t = 0.2$ and number of frames equal to 125 is good enough for the purpose of this thesis. We are now ready to move forward with one last SOR check.

3.2 One Last SOR Check

In the previous chapter, it was found through coarse simulation runs that using the $(+--)$ combination for SOR of (BB MB PB) is the most effective at sending the weakest vortex closest to the wall in the shortest amount of time. As a final check before nearly 8000 simulations were performed, three simulations were ran comparing the combinations (– –

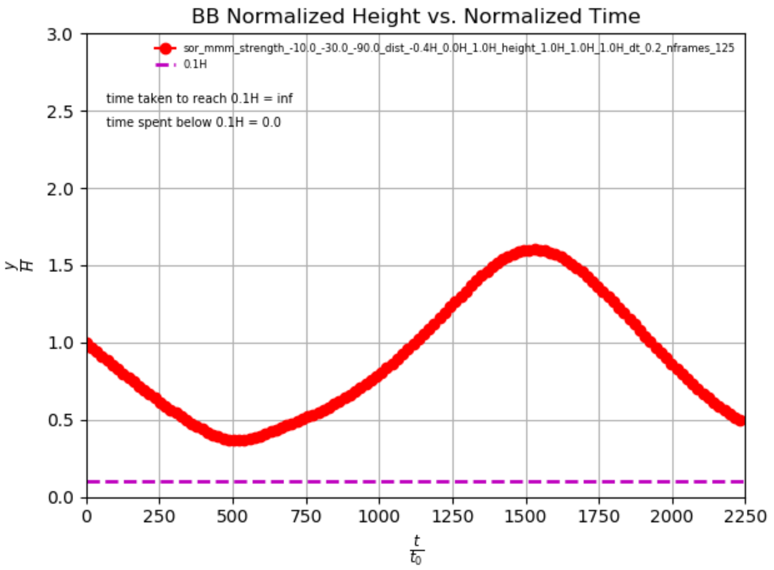

Figure 3.5: BB's normalized height above the surface versus the normalized time for the parameters specified in the annotations. This is a final SOR check before proceeding. The senses of rotation of the vortices are (BB MB PB) = (− − −).

−), (− + −), and (+ − −) using the exact settings for all of the thousands of simulations planned. These combinations were chosen based on the results in Table 2.1 whose outcome was to drive BB downward towards the wall rather than upward. In all three simulations, the vortex strength of BB is 10, MB is 30, and PB is 90. The separation distance between BB and MB, d_1, is set to 0.4. The separation distance between MB and MB, d_2, is set to 1.0. All three vortices are 1.0 above the wall.

Figures 3.5, 3.6, and 3.7 show the trajectory of BB over the time duration of the simulation for the combinations (− − −), (− + −), and (+ − −), respectively. This final check confirms that (+ − −) is the best choice.

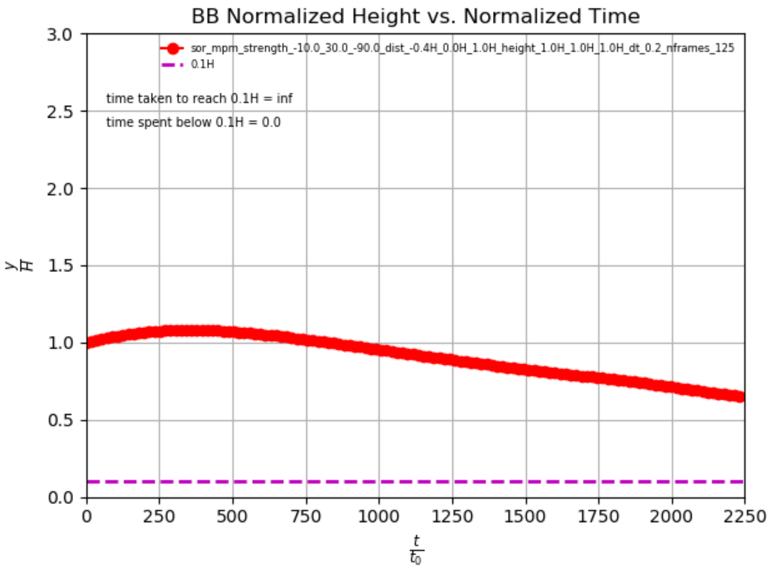

Figure 3.6: BB's normalized height above the surface versus the normalized time for the parameters specified in the annotations. This is a final SOR check before proceeding. The senses of rotation of the vortices are (BB MB PB) = (− + −).

3.3 Results

Recall that the end goals of this thesis included obtaining two types of contour plots. The first contour plot is a plot of BB's minimum height above the wall, with $\frac{d_1}{H}$ on the y-axis (ranging from 0.2 to 2.0) and $\frac{\Gamma_2}{\Gamma_1}$ on the x-axis (ranging from 1.1 to 3.0). The second contour plot is a plot of how long BB stayed below the threshold line after it crosses it, with the same set of axes. This second plot gives us additional information about the configurations, and will help further narrow down the local optimum or optima. These two types of contour plots will ultimately help us crown two champions at the end.

The results of all 7980 simulations synthesized into 42 contour plots can be found in the following pages. The contour plots have been smoothed out, so a 3D scatter plot of a typical simulation is shown in Fig. 3.8 to illustrate the spacing of individual data points. Tables

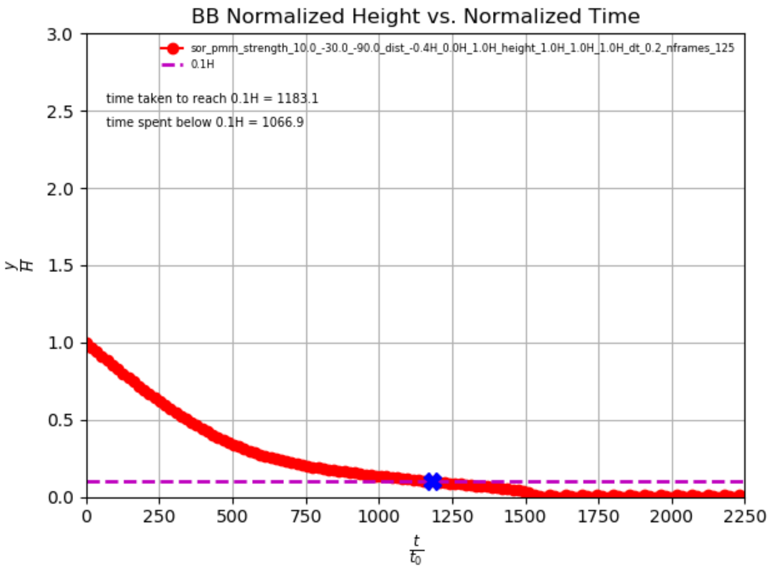

Figure 3.7: BB's normalized height above the surface versus the normalized time for the parameters specified in the annotations. This is a final SOR check before proceeding. The senses of rotation of the vortices are (BB MB PB) = $(+\,-\,-)$.

3.1-3.7 organize the contour plots in pairs of three, one row for a fixed value of $\frac{d_2}{H}$. The contour plots on the left-hand side (LHS) are contours of BB's minimum height above the wall. In these plots, the bluest region(s) (i.e. the lowest values) are the the ones we are most interested in. The contour plots on the right-hand side (RHS) are contours of BB's residence time[1]. In this case, it is the red region(s) (i.e. the largest values) that we care about.

3.4 Discussion

There is a lot of information to take in from all 42 contour plots, so let us take it slow and break things down.

Let us examine Table 3.1 in more detail. Focusing solely on this one table for now will

---

[1] Recall that in this thesis, the term *residence time* is used to refer to the time BB spends below the threshold line.

Nr.	a	b
1	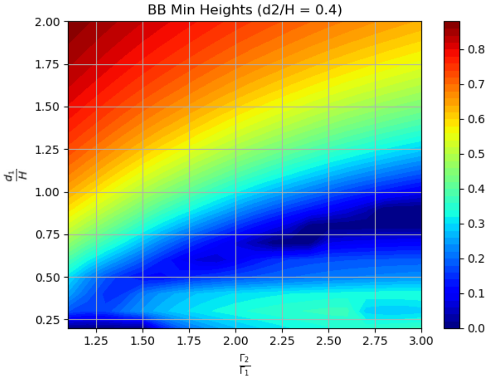 BB Min Heights (d2/H = 0.4) 	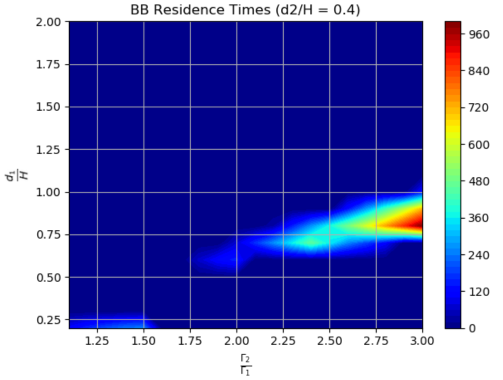 BB Residence Times (d2/H = 0.4)
2	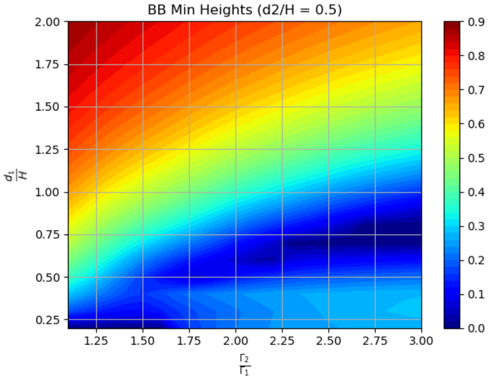 BB Min Heights (d2/H = 0.5) 	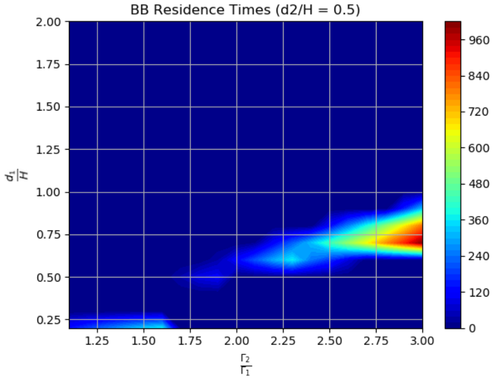 BB Residence Times (d2/H = 0.5)
3	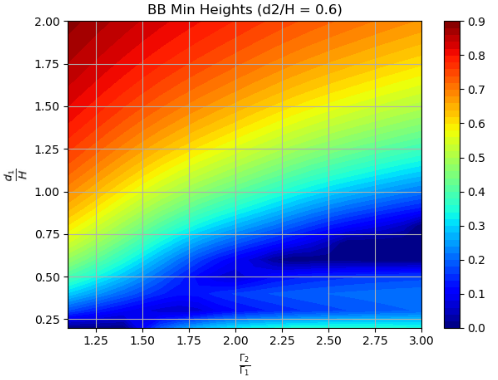 BB Min Heights (d2/H = 0.6) 	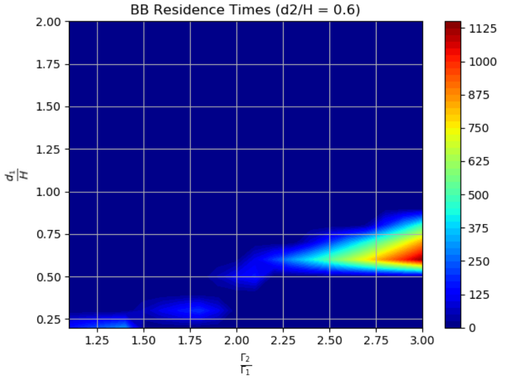 BB Residence Times (d2/H = 0.6)

Table 3.1: Contour plots of BB's minimum height above the wall (LHS) and residence time below the threshold line of $0.1H$ (RHS). This set of plots have been created for the ratios $\frac{d_2}{H}$ = 0.4, 0.5, and 0.6, respectively. SOR is (BB MB PB)=$(+\,-\,-)$.

Nr.	a	b
4	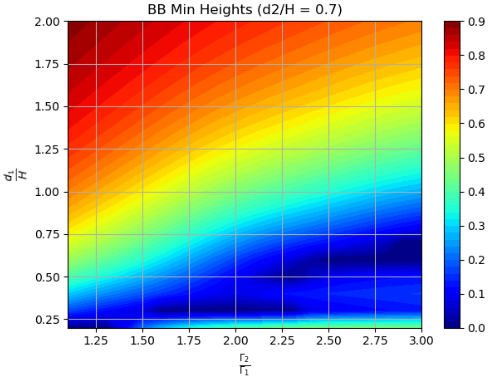	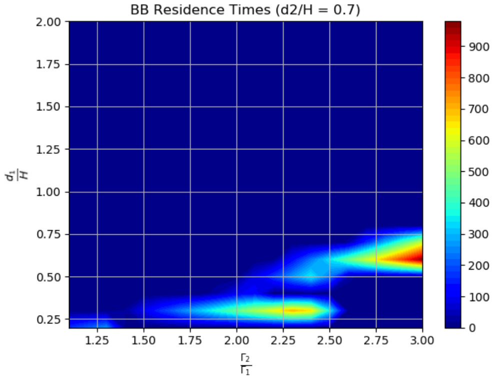
5	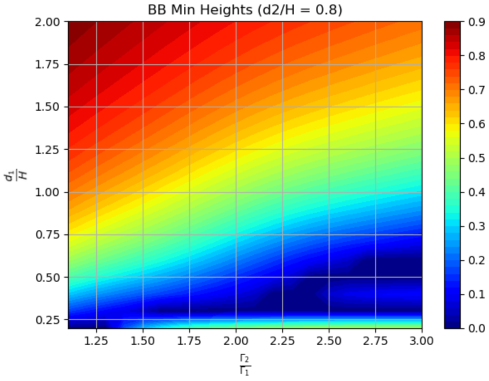	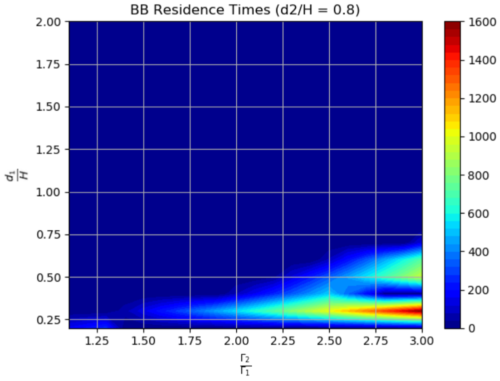
6	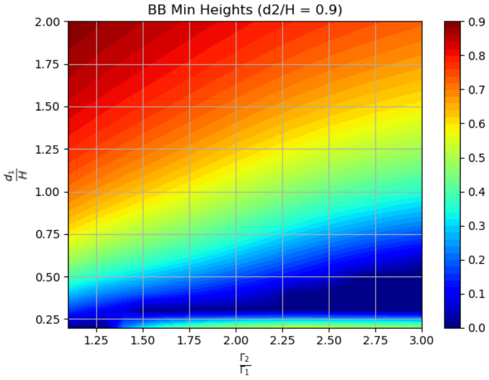	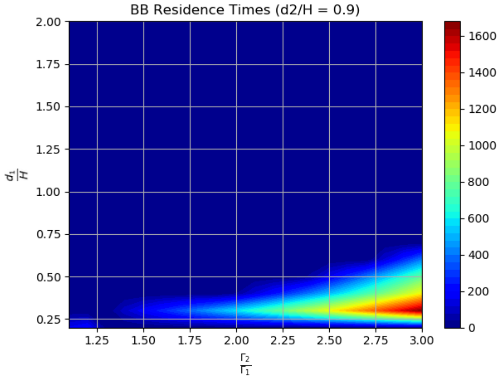

Table 3.2: Contour plots of BB's minimum height above the wall (LHS) and residence time below the threshold line of $0.1H$ (RHS). This set of plots have been created for the ratios $\frac{d_2}{H}$ = 0.7, 0.8, and 0.9, respectively. SOR is (BB MB PB)=($+--$).

Nr.	a	b
7*	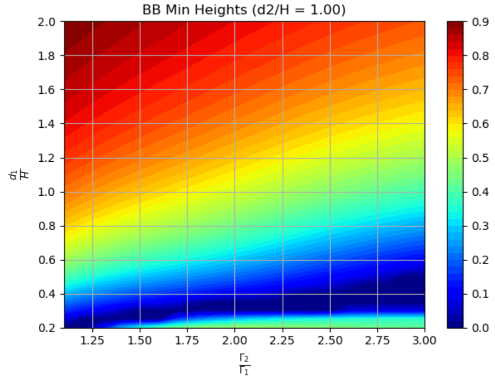	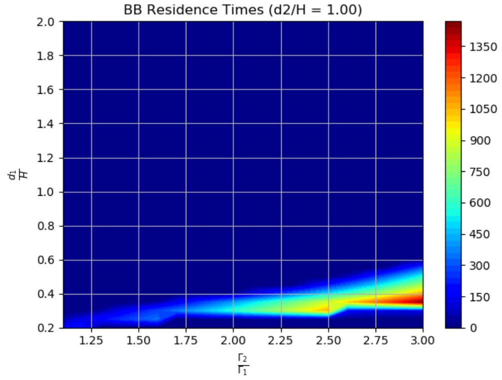
8*	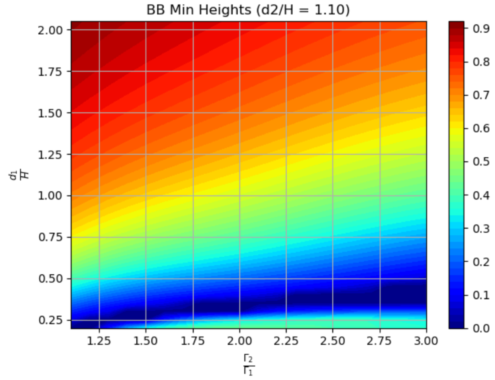	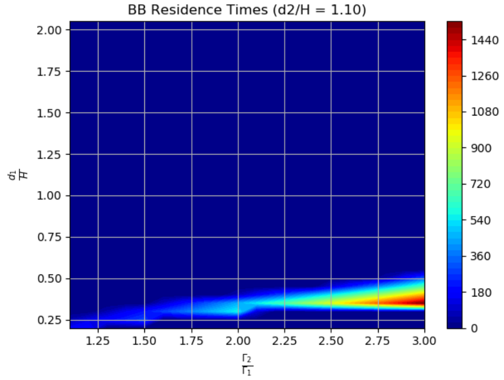
9	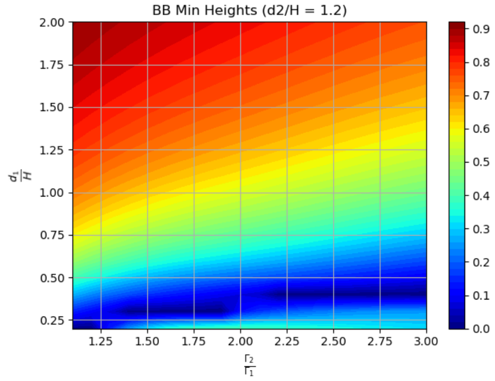	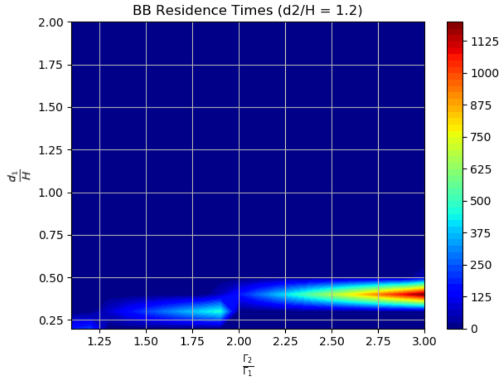

Table 3.3: Contour plots of BB's minimum height above the wall (LHS) and residence time below the threshold line of $0.1H$ (RHS). This set of plots have been created for the ratios $\frac{d_2}{H}$ = 1.0, 1.1, and 1.2, respectively. SOR is (BB MB PB)=(+ − −).

Nr.	a	b
10	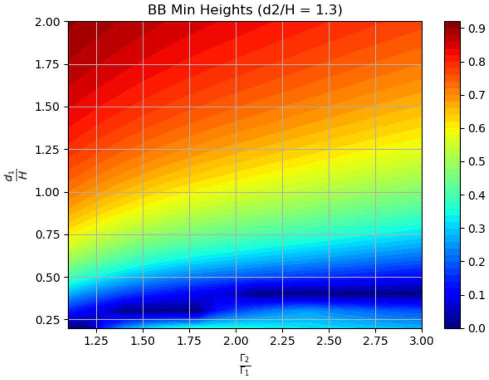	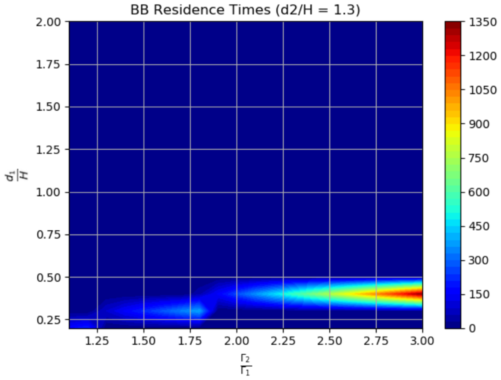
11	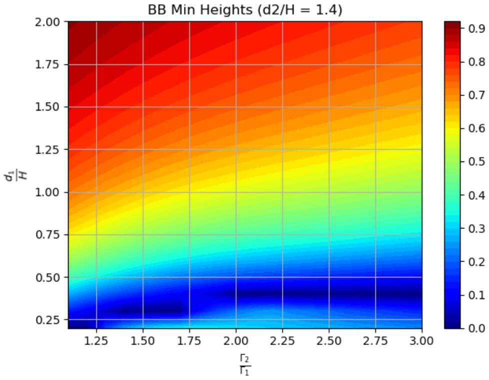	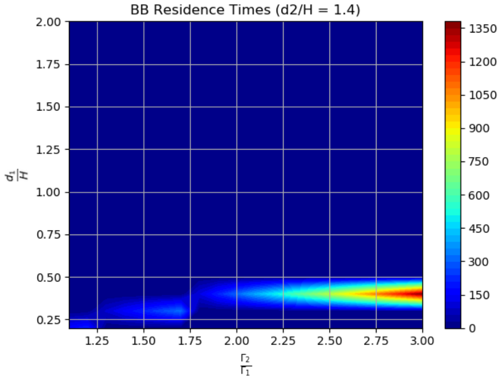
12	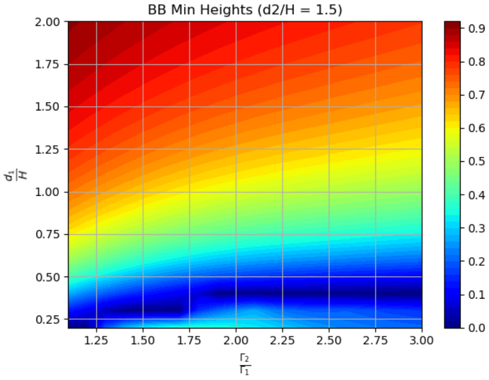	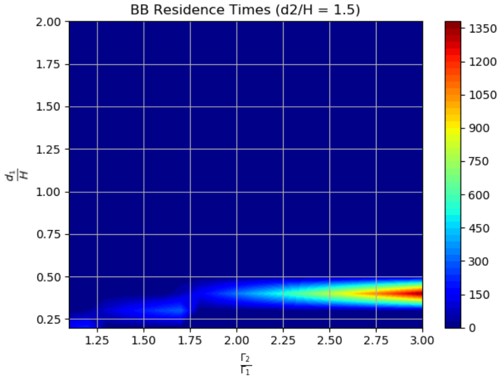

Table 3.4: Contour plots of BB's minimum height above the wall (LHS) and residence time below the threshold line of $0.1H$ (RHS). This set of plots have been created for the ratios $\frac{d_2}{H}$ = 1.3, 1.4, and 1.5, respectively. SOR is (BB MB PB)=($+--$).

Nr.	a	b
13	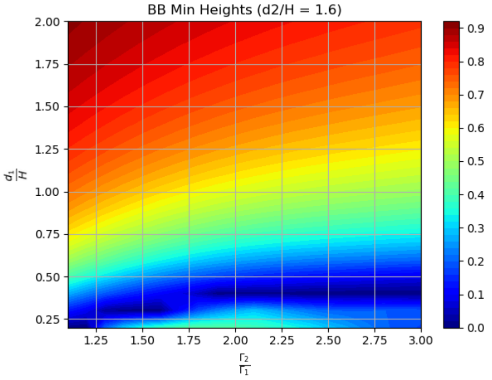	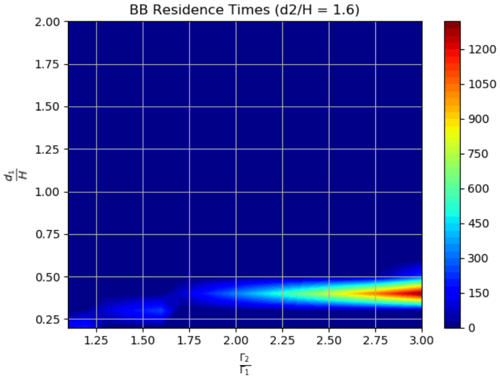
14*	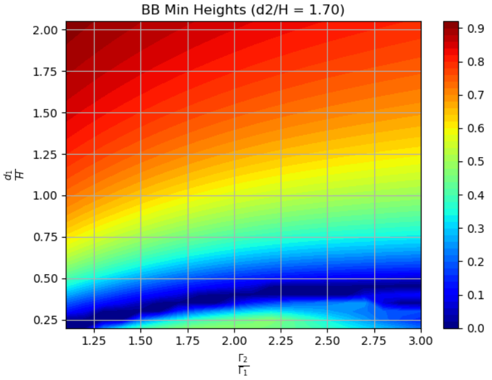	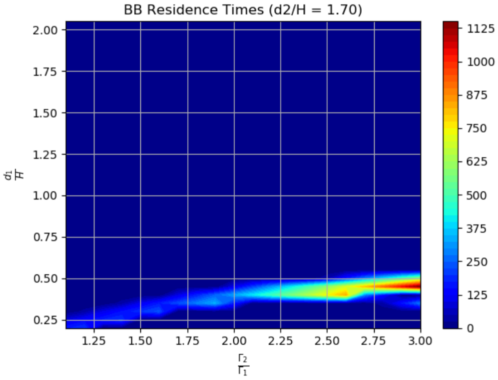
15*	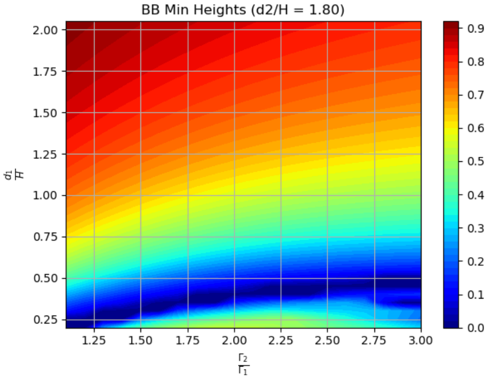	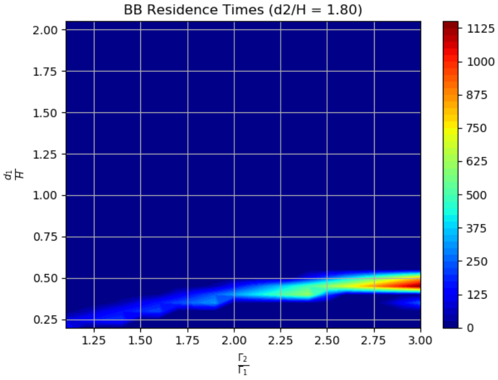

Table 3.5: Contour plots of BB's minimum height above the wall (LHS) and residence time below the threshold line of $0.1H$ (RHS). This set of plots have been created for the ratios $\frac{d_2}{H}$ = 1.6, 1.7, and 1.8, respectively. SOR is (BB MB PB)=($+--$).

Nr.	a	b
16*	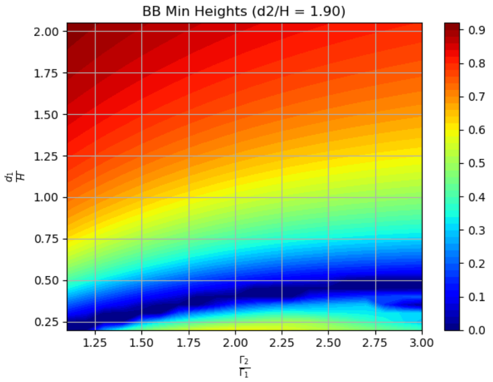	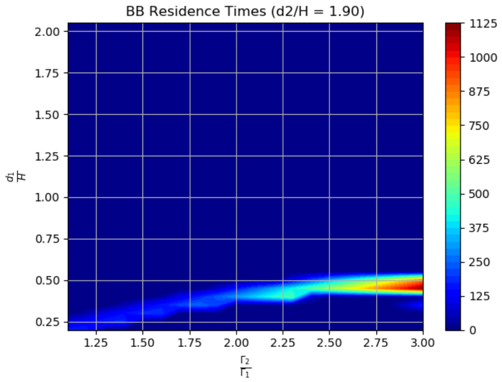
17*	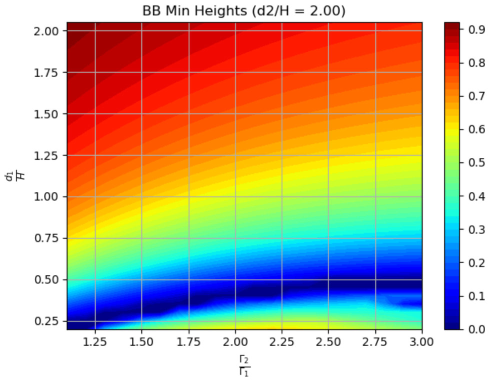	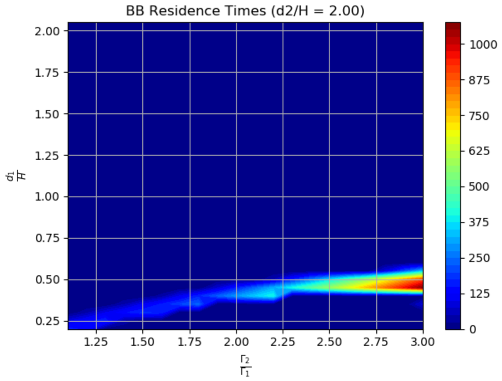
18	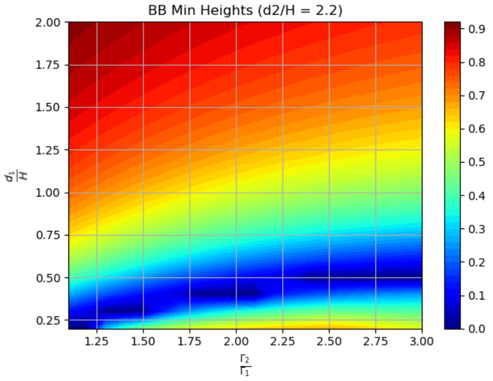	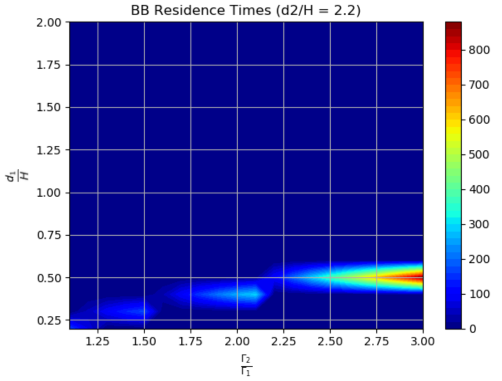

Table 3.6: Contour plots of BB's minimum height above the wall (LHS) and residence time below the threshold line of $0.1H$ (RHS). This set of plots have been created for the ratios $\frac{d_2}{H}$ = 1.9, 2.0, and 2.2, respectively. SOR is (BB MB PB)=($+--$).

Nr.	a	b
19	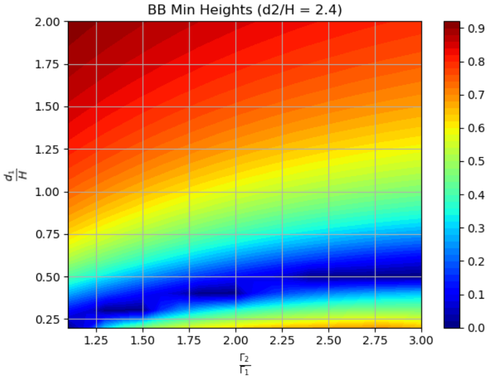 BB Min Heights (d2/H = 2.4)	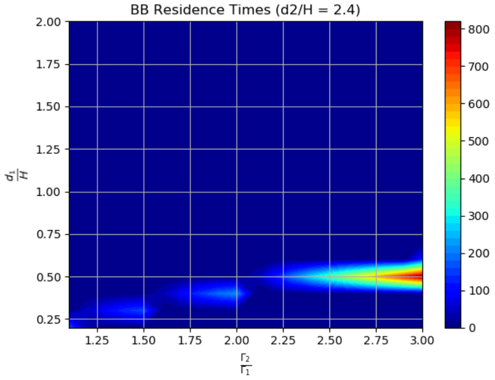 BB Residence Times (d2/H = 2.4)
20	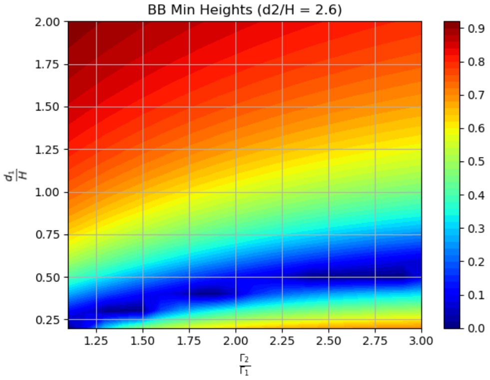 BB Min Heights (d2/H = 2.6)	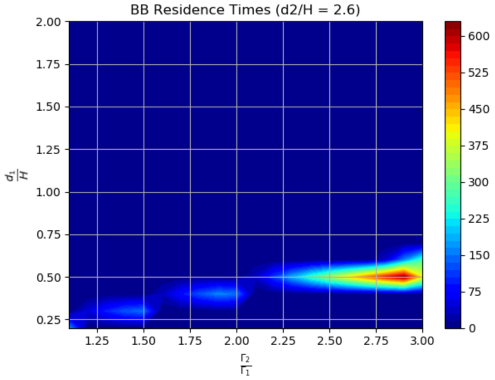 BB Residence Times (d2/H = 2.6)
21	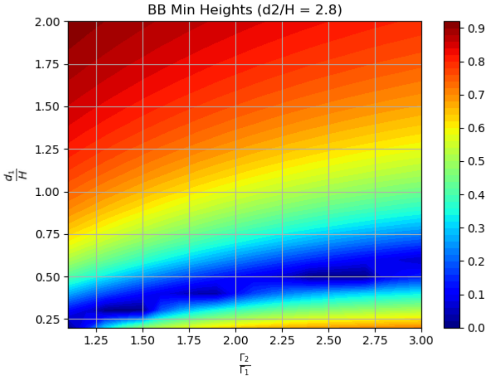 BB Min Heights (d2/H = 2.8)	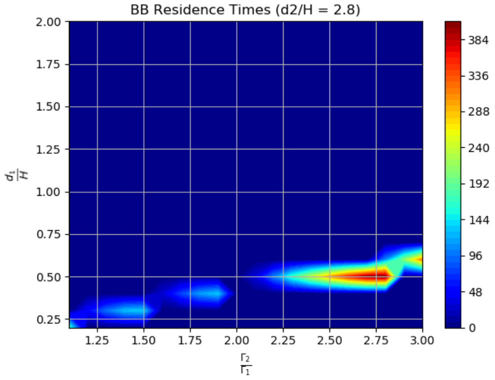 BB Residence Times (d2/H = 2.8)

Table 3.7: Contour plots of BB's minimum height above the wall (LHS) and residence time below the threshold line of $0.1H$ (RHS). This set of plots have been created for the ratios $\frac{d_2}{H}$ = 2.4, 2.6, and 2.8, respectively. SOR is (BB MB PB)=(+ − −).

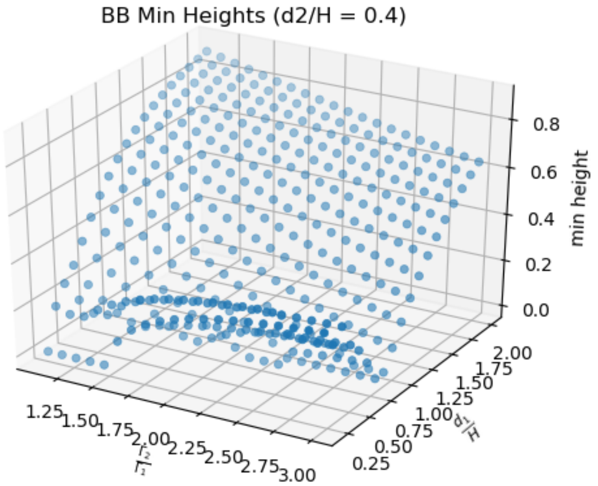

Figure 3.8: 3D scatter plot of BB's minimum height above the surface for $\frac{d_2}{H} = 0.4$. The figure illustrates the spacing of all of the data points. The senses of rotation of the vortices are (BB MB PB) = (+ − −).

serve as a basis for comparison when we move on to the other tables. From a bird's eye view, it is reassuring to see that in the regions of smallest values in all of the contour plots of BB's minimum height, the corresponding contour plot of BB's residence time tells us that those regions also happen to be where we can find BB hanging around close to the surface for the longest time. This observation in and of itself gives us confidence that the code is working properly. Continuing with our examination, if we just look at the contour plots on the left-hand side, we see that the smallest values of BB's minimum height (the blue regions) are achieved when the relative strengths of the vortices are high. This makes sense since a stronger vortex induces a neighboring vortex to move quicker. The greater the vortex strength, the greater its ability to send BB closest to the wall as well as make it stay there for as long as possible. The red regions of the contour plots on the right-hand side showing residence times confirm this. Still looking at the contour plots on the left-hand side, notice that as the value of $\frac{d_2}{H}$ changes, so do the blue regions of minimum heights. This tells us that the local minimum is sensitive to different values of $\frac{d_2}{H}$; depending on how far PB is, the effectiveness of the 2D vortex whip as a whole is affected. The contour plots of residence times on the RHS show this dependence on $\frac{d_2}{H}$ value as well. Finally, both the minimum height and residence times contour plots show that the local minimum is achieved when $\frac{d_1}{H} < 1$. For $\frac{d_2}{H} = 0.5$, for instance, the local minimum is achieved when $\frac{d_1}{H} = 0.75$. The insight we gained from crude simulation runs in the previous chapter which indicated that it was more effective to vary the inter-separation distance between BB and MB (d_1) rather than the inter-separation distance between MB and PB (d_2) is confirmed here once more. Thus it is reasonable to extrapolate that the performance of a vortex whip is more effective when d_1 is less than d_2. This is the first exciting discovery we have uncovered!

Initially, the above comments were made specifically for Table 3.1. If we examine the rest of the tables closely, we realize that the same trends are found throughout all of the tables; the discussion in the previous paragraph is applicable to *all* of the other tables as well. Fortunately, the story does not end here! Having scanned the parameter space of the 2D vortex whip using so many values of $\frac{d_2}{H}$ revealed at least two more new discoveries about how to optimize a vortex whip. If we just examine the contour plots on the RHS now for all of the tables, notice that the region of highest residence times (red regions) shifts downward from $\frac{d_1}{H} = 0.8$ to $\frac{d_1}{H} = 0.6$ in Table 3.1, then from $\frac{d_1}{H} = 0.6$ to $\frac{d_1}{H} = 0.3$ in Table 3.2, as $\frac{d_2}{H}$ varies from 0.4 to 0.9. As $\frac{d_2}{H}$ increases from 1.2 to 1.6, the region of highest residence time appears to stay about constant at $\frac{d_1}{H} = 0.4$. Something interesting happens when $\frac{d_2}{H} = 1.9$: the region of highest residence time moves upward rather than downward this time. From $\frac{d_2}{H} = 1.9$ to $\frac{d_2}{H} = 2.8$, the region of highest residence time appears to stabilize at $\frac{d_1}{H} = 0.5$. So the second discovery we uncovered from examining these trends is that the optimal configuration of a 2D vortex whip *is* sensitive to the inter-separation distance between MB and PB, d_2. This is not surprising, in hindsight, but what is surprising is that the sensitivity to d_2 is not that great. We saw that for a range of $\frac{d_2}{H}$ values, the extremum for BB's minimum height and residence time remained stable until about $\frac{d_2}{H} = 1.7$ where the extrema shifted upwards, but again remained stable afterward.

For most of the contour plots in Tables 3.1-3.7, we see that the extrema regions generally appeared where $\frac{\Gamma_2}{\Gamma_1}$ is the highest. It is reasonable to assume, then, that the greater the strengths of the vortices in a vortex whip, the better it is at sending the weakest vortex closest to the wall for the longest time. Tables 3.8-3.14 show 3D surface plots of BB's minimum height and residence time for all of the corresponding contour plots in this chapter. The main surface plot is displayed in a grey color. The profile of the surface plot is projected onto all three respective coordinate planes to give additional perspective. Extrema points are labeled by either red or blue dots. Red dots indicate highest values and blue points indicate lowest values. These surface plots give us a different perspective of the parameter space.

3.5 *Compilation of Results*

Figure 3.9 compiles the largest residence time from each row of Tables 3.1-3.7 and plots them against the appropriate ratio $\frac{d_2}{H}$. Additional simulations were performed to collect more data points around various peaks, hence the increased density of points in some portions of the graphs but not others. The figure helps point out any trends in the data. For all values of $\frac{d_2}{H}$, the smallest minimum height calculated from each row of Tables 3.1-3.7 is zero.

From Fig. 3.9, we can see that the maximum residence time is located around $\frac{d_2}{H} = 0.9$, where $\frac{d_1}{H} = 0.3$. This result is another significant finding. It tells us that a vortex whip performs much better when d_2—the separation distance between the medium strength and strongest strength vortices—is close to the vortices' initial height above the wall, but not exceeding it.

An astonishing observation regarding Fig. 3.9 is its non-smooth nature; there are noticeable peaks and valleys instead of a smooth curve. Take the peak where $0.5 \leq \frac{d_2}{H} \leq 1.2$, for example. This region of parameter space has interesting wiggles which may or may not be physical for the 3D viscous case. But based on the simulations performed, it looks like these situations are the optimal configurations that have the best chance of future success in real

Nr.	a	b
22	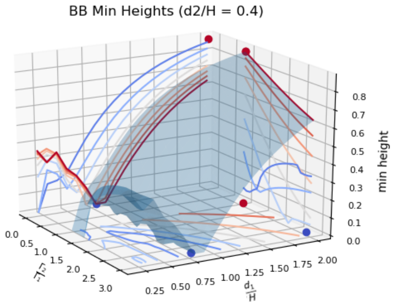 BB Min Heights (d2/H = 0.4)	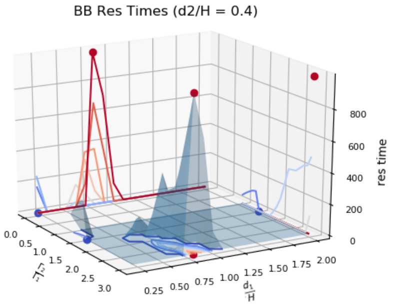 BB Res Times (d2/H = 0.4)
23	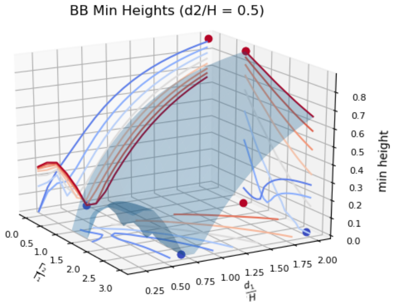 BB Min Heights (d2/H = 0.5)	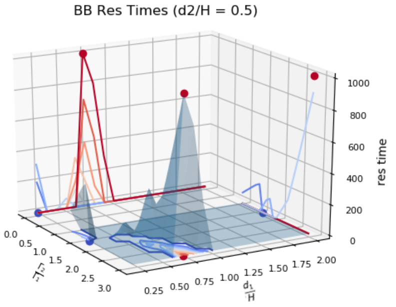 BB Res Times (d2/H = 0.5)
24	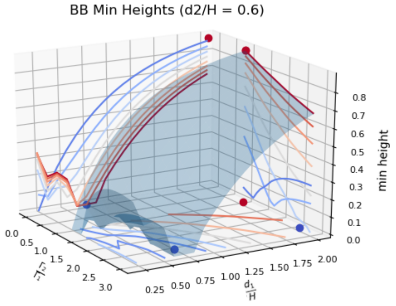 BB Min Heights (d2/H = 0.6)	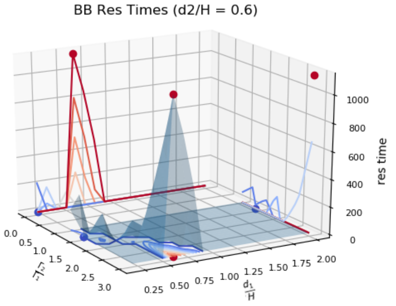 BB Res Times (d2/H = 0.6)

Table 3.8: Three-dimensional surface plots of BB's minimum height above the wall (LHS) and residence time below the threshold line of $0.1H$ (RHS). This set of plots have been created for the ratios $\frac{d_2}{H} = 0.4$, 0.5, and 0.6, respectively. SOR is (BB MB PB)=($+--$).

Nr.	a	b
25	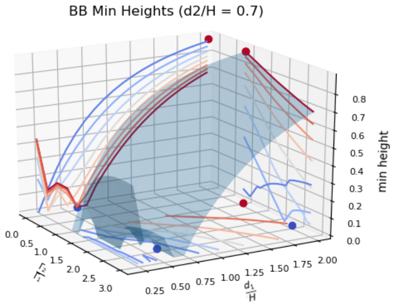 BB Min Heights (d2/H = 0.7)	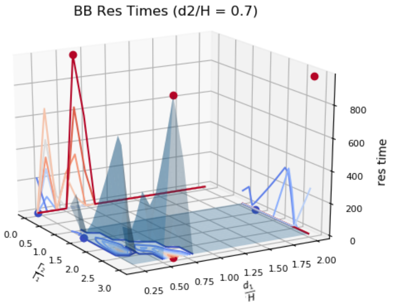 BB Res Times (d2/H = 0.7)
26	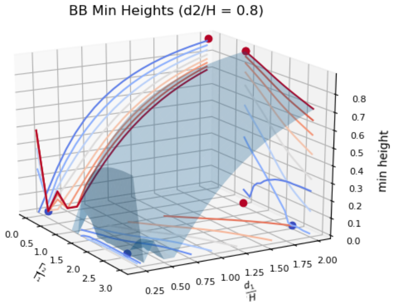 BB Min Heights (d2/H = 0.8)	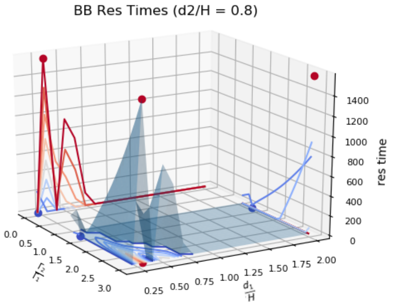 BB Res Times (d2/H = 0.8)
27	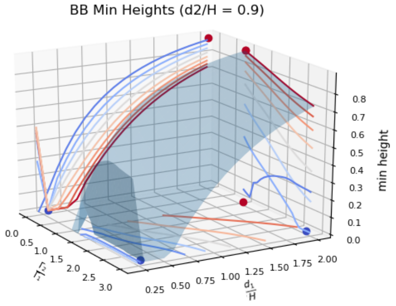 BB Min Heights (d2/H = 0.9)	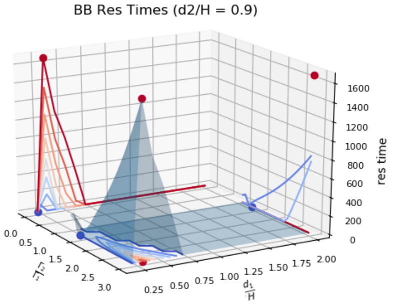 BB Res Times (d2/H = 0.9)

Table 3.9: Three-dimensional surface plots of BB's minimum height above the wall (LHS) and residence time below the threshold line of $0.1H$ (RHS). This set of plots have been created for the ratios $\frac{d_2}{H} = 0.7$, 0.8, and 0.9, respectively. SOR is (BB MB PB)=$(+--)$.

Nr.	a	b
28*	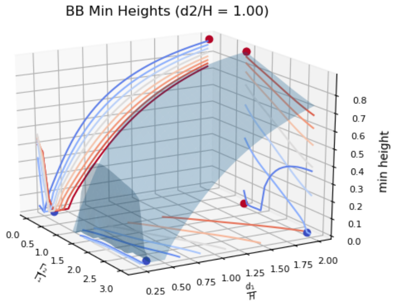 BB Min Heights (d2/H = 1.00)	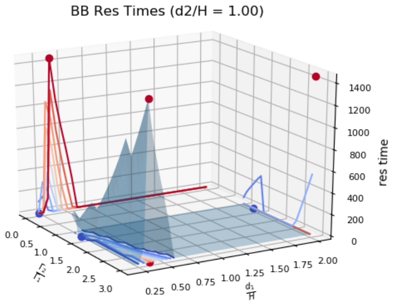 BB Res Times (d2/H = 1.00)
29*	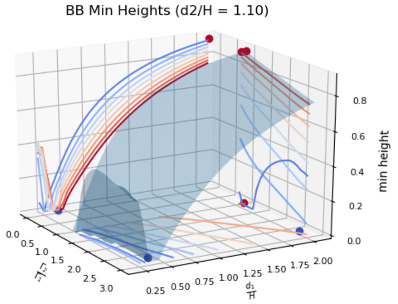 BB Min Heights (d2/H = 1.10)	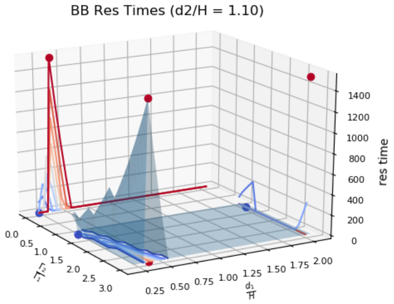 BB Res Times (d2/H = 1.10)
30	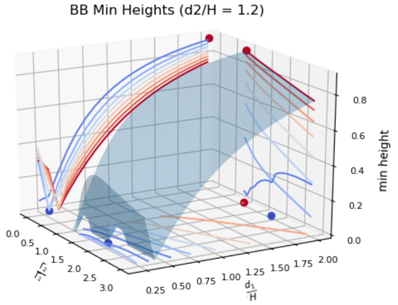 BB Min Heights (d2/H = 1.2)	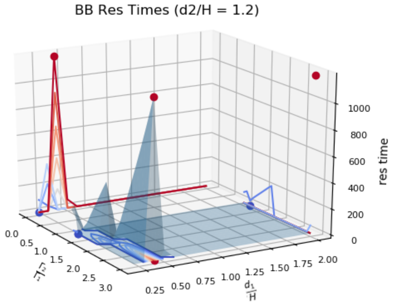 BB Res Times (d2/H = 1.2)

Table 3.10: Three-dimensional surface plots of BB's minimum height above the wall (LHS) and residence time below the threshold line of $0.1H$ (RHS). This set of plots have been created for the ratios $\frac{d_2}{H} = 1.0$, 1.1, and 1.2, respectively. SOR is (BB MB PB)=$(+--)$.

Nr.	a	b
31	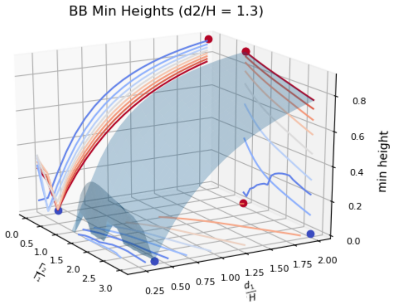	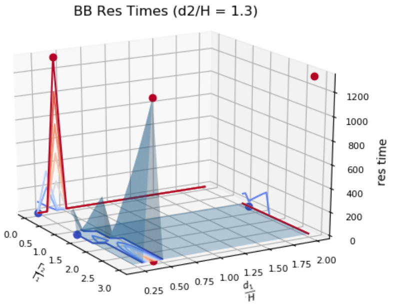
32	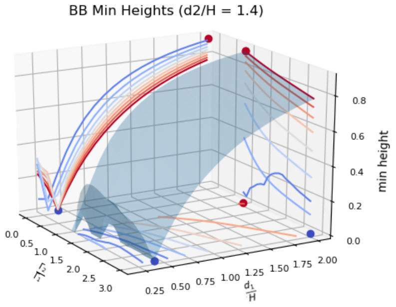	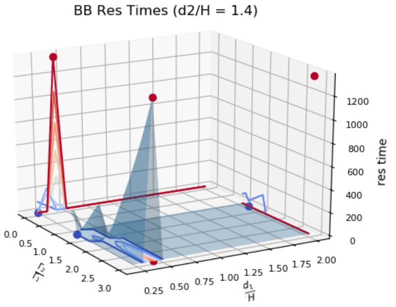
33	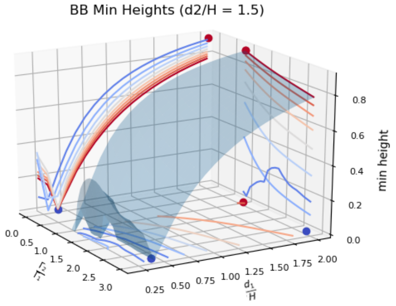	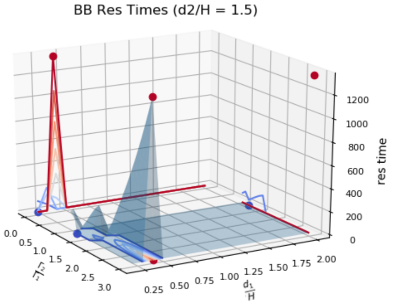

Table 3.11: Three-dimensional surface plots of BB's minimum height above the wall (LHS) and residence time below the threshold line of $0.1H$ (RHS). This set of plots have been created for the ratios $\frac{d_2}{H} = 1.3$, 1.4, and 1.5, respectively. SOR is (BB MB PB)=$(+ - -)$.

Nr.	a	b
34	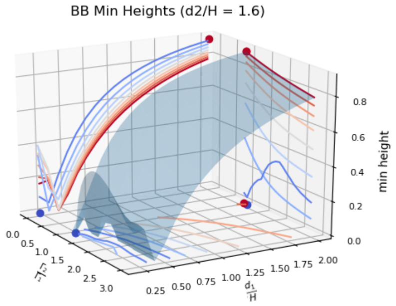 BB Min Heights (d2/H = 1.6) 	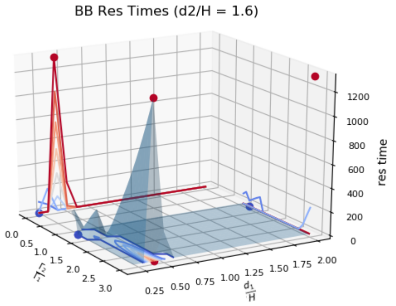 BB Res Times (d2/H = 1.6)
35*	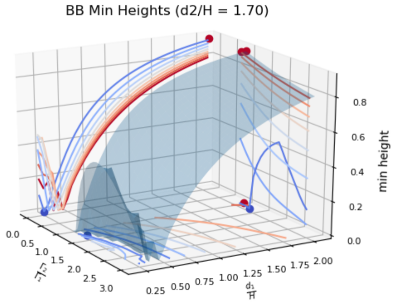 BB Min Heights (d2/H = 1.70) 	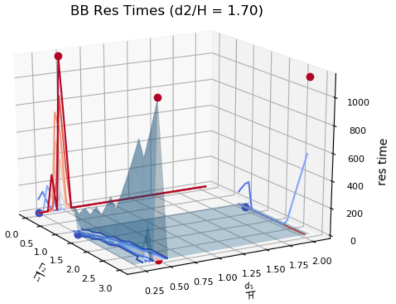 BB Res Times (d2/H = 1.70)
36*	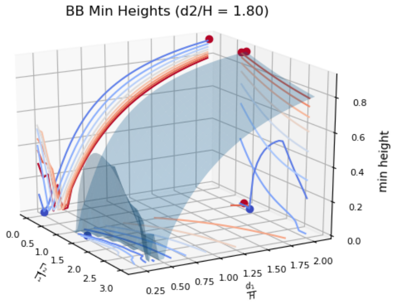 BB Min Heights (d2/H = 1.80) 	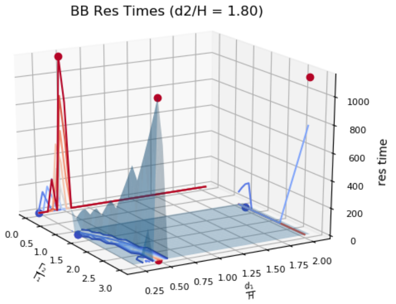 BB Res Times (d2/H = 1.80)

Table 3.12: Three-dimensional surface plots of BB's minimum height above the wall (LHS) and residence time below the threshold line of $0.1H$ (RHS). This set of plots have been created for the ratios $\frac{d_2}{H} = 1.6$, 1.7, and 1.8, respectively. SOR is (BB MB PB)=$(+--)$.

Nr.	a	b
37*	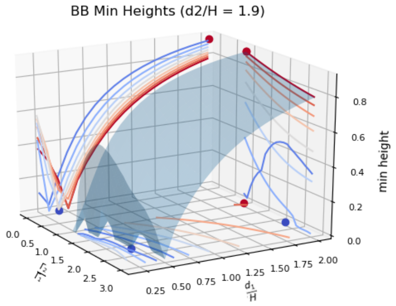	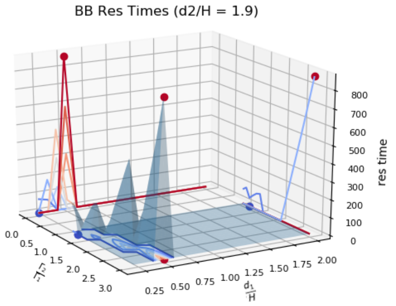
38*	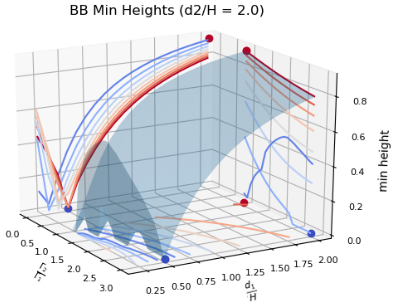	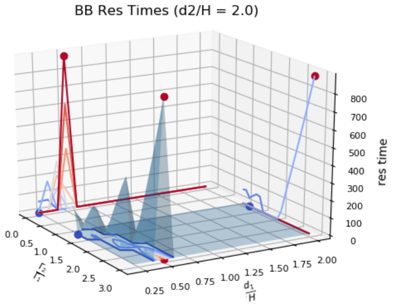
39	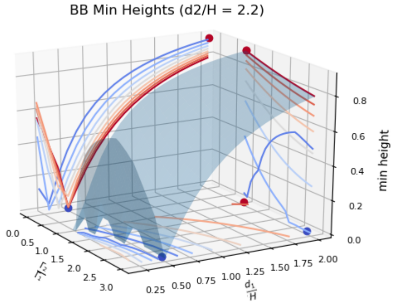	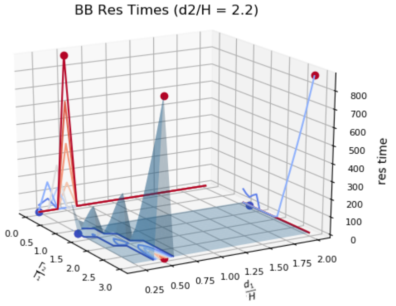

Table 3.13: Three-dimensional surface plots of BB's minimum height above the wall (LHS) and residence time below the threshold line of $0.1H$ (RHS). This set of plots have been created for the ratios $\frac{d_2}{H} = 1.9$, 2.0, and 2.2, respectively. SOR is (BB MB PB)=$(+--)$.

Nr.	a	b
40	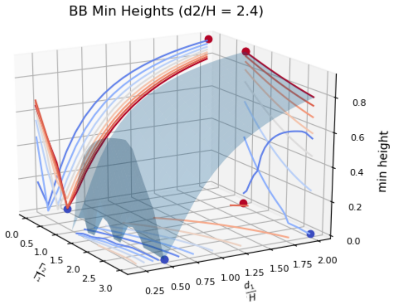 BB Min Heights (d2/H = 2.4)	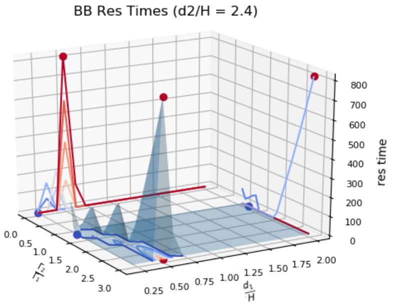 BB Res Times (d2/H = 2.4)
41	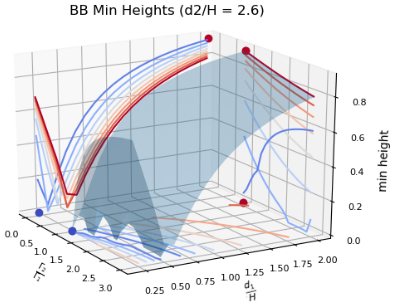 BB Min Heights (d2/H = 2.6)	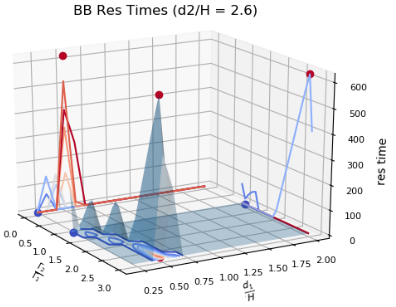 BB Res Times (d2/H = 2.6)
42	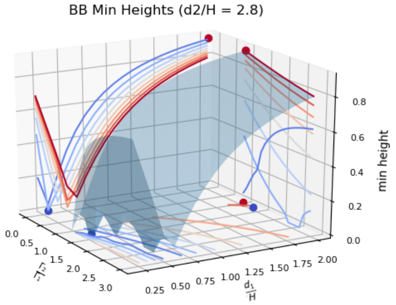 BB Min Heights (d2/H = 2.8)	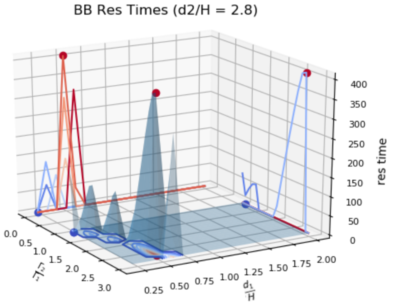 BB Res Times (d2/H = 2.8)

Table 3.14: Three-dimensional surface plots of BB's minimum height above the wall (LHS) and residence time below the threshold line of $0.1H$ (RHS). This set of plots have been created for the ratios $\frac{d_2}{H}$ = 2.4, 2.6, and 2.8, respectively. SOR is (BB MB PB)=($+--$).

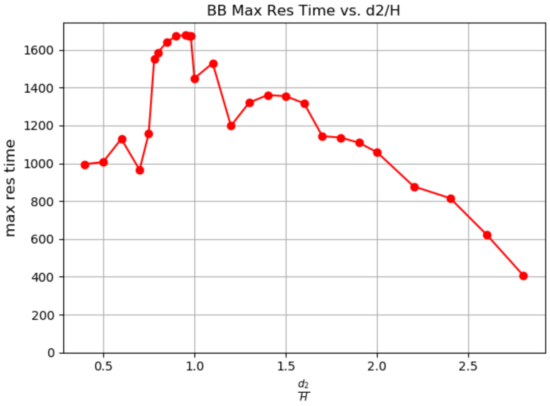

Figure 3.9: Graph of largest residence time from each contour plot from Tables 3.1-3.7 versus $\frac{d_2}{H}$.

life. While conscientious effort was made to obtain more data points for regions such as this, it does not benefit us greatly to continue trying to resolve every wiggle, since the equations of vortex dynamics that we are solving in the 2D problem are not the same equations Mother Nature governs by anyway. It is especially not worthwhile to pursue resolving wiggles that do not look like they are leading to optimum behavior.

The non-smooth nature of the curve in Fig. 3.9 does suggest something about the resolution of our simulations in some regions, however. Take the kink at $\frac{d_2}{H} = 1.7$. This kink seems to suggest that data points nearby it should be raised up higher to produce a smoother falloff for the overall curve. There are other regions of Fig. 3.9 that look like they can benefit from increased resolution to give the overall curve a smoother shape. Despite this, the peak in the current figure is still an outstanding feature that indicates a local maximum.

Every contour plot of BB's minimum height above the wall and BB's residence time below the $0.1H$ threshold line has a minimum and a maximum. Tables 3.15 and 3.16 identify what these extrema points are for each of the contour plots from Tables 3.1-3.7. They supplement Fig. 3.9 with additional information.

$\frac{d_2}{H}$	$\frac{\Gamma_2}{\Gamma_1}$ **min**	$\frac{d_1}{H}$ **min**	**minHeight (min)**	$\frac{\Gamma_2}{\Gamma_1}$ **max**	$\frac{d_1}{H}$ **max**	**minHeight (max)**
0.4	2.9	0.8	0.0	1.1	2.0	0.88
0.5	2.9	0.7	0.0	1.1	2.0	0.88
0.6	2.8	0.75	0.0	1.1	2.0	0.89
0.7	2.5	0.6	0.0	1.1	2.0	0.89
0.75	2.6	0.3	0.0	1.1	2.0	0.89
0.78	2.5	0.3	0.0	1.1	2.0	0.9
0.8	2.5	0.3	0.0	1.1	2.0	0.9
0.85	2.7	0.3	0.0	1.1	2.0	0.9
0.9	2.9	0.3	0.0	1.1	2.0	0.9
0.95	2.7	0.3	0.0	1.1	2.0	0.9
0.97	2.7	0.3	0.0	1.1	2.0	0.9
0.98	2.7	0.4	0.0	1.1	2.0	0.9
1.0	2.9	0.35	0.0	1.1	2.0	0.9
1.1	2.8	0.4	0.0	1.1	2.05	0.91
1.2	1.9	0.3	0.0	1.1	2.0	0.9
1.3	3.0	0.4	0.0	1.1	2.0	0.9
1.4	3.0	0.4	0.0	1.1	2.0	0.9
1.5	2.9	0.4	0.0	1.1	2.0	0.91
1.6	1.2	0.2	0.0	1.1	2.0	0.91
1.7	1.4	0.25	0.0	1.1	2.05	0.91
1.8	1.4	0.25	0.0	1.1	2.05	0.91
1.9	3.0	0.45	0.0	1.1	2.05	0.91
2.0	2.6	0.45	0.0	1.1	2.05	0.91
2.2	2.9	0.5	0.0	1.1	2.0	0.91
2.4	3.0	0.5	0.0	1.1	2.0	0.91
2.6	1.1	0.2	0.0	1.1	2.0	0.91
2.8	1.4	0.3	0.0	1.1	2.0	0.91

Table 3.15: Summary of all the extrema points (minima and maxima) for every contour plot of BB's height above the wall. These results are for the SOR combination (BB MB PB)=(+ – –).

$\frac{d_2}{H}$	$\frac{\Gamma_2}{\Gamma_1}$ **min**	$\frac{d_1}{H}$ **min**	**resTime (min)**	$\frac{\Gamma_2}{\Gamma_1}$ **max**	$\frac{d_1}{H}$ **max**	**resTime (max)**
0.4	1.6	0.2	0.0	3.0	0.8	995.7
0.5	1.7	0.2	0.0	3.0	0.7	1006.67
0.6	1.5	0.2	0.0	3.0	0.6	1129.38
0.7	1.5	0.2	0.0	3.0	0.6	965.06
0.75	1.4	0.2	0.0	2.7	0.3	1157.77
0.78	1.4	0.2	0.0	3.0	0.3	1552.08
0.8	1.4	0.2	0.0	3.0	0.3	1585.91
0.85	1.4	0.2	0.0	3.0	0.3	1642.63
0.9	1.4	0.2	0.0	3.0	0.3	1672.18
0.95	1.4	0.2	0.0	3.0	0.3	1679.35
0.97	1.4	0.2	0.0	3.0	0.3	1675.98
0.98	1.4	0.2	0.0	3.0	0.3	1672.36
1.0	1.4	0.2	0.0	3.0	0.35	1449.54
1.1	1.3	0.2	0.0	3.0	0.35	1529.74
1.2	1.3	0.2	0.0	3.0	0.4	1198.2
1.3	1.3	0.2	0.0	3.0	0.4	1321.28
1.4	1.3	0.2	0.0	3.0	0.4	1360.96
1.5	1.3	0.2	0.0	3.0	0.4	1355.23
1.6	1.3	0.2	0.0	3.0	0.4	1317.77
1.7	1.3	0.2	0.0	3.0	0.45	1143.81
1.8	1.3	0.2	0.0	3.0	0.45	1136.36
1.9	1.3	0.2	0.0	3.0	0.45	1109.0
2.0	1.3	0.2	0.0	3.0	0.45	1058.47
2.2	1.3	0.2	0.0	3.0	0.5	878.02
2.4	1.3	0.2	0.0	3.0	0.5	815.47
2.6	1.2	0.2	0.0	2.9	0.5	622.26
2.8	1.2	0.2	0.0	2.8	0.5	407.18

Table 3.16: Summary of all the extrema points (minima and maxima) for every contour plot of BB's residence time below the $0.1H$ threshold. This table supplements Fig. 3.9 with additional information. These results are for the SOR combination (BB MB PB)=$(+--)$.

3.6 Limitations of Results

As mentioned in the “Vortex Whip” section of the introductory chapter of this thesis, the 2D vortex whip problem paves the way for solving the corresponding 3D problem. However, there are at least three limitations pertaining to the results of the 2D vortex whip problem when one tries to apply them to the 3D case. Firstly, results very close to the wall for the 2D problem are not physical. As explained in the Chapter 1, the no-slip condition does not apply along a wall in potential flow, so the movement of vortices at the wall do not accurately represent what should happen in real experiments. Secondly, recall that we did not include viscosity in our simulations of 2D vortex whip dynamics. Viscosity introduces stress forces into the dynamics, affecting how fluid particles move and interact. When trying to solve the 3D case, viscosity must be accounted for and the results from our work with the 2D case might have less range of applicability. Thirdly, the 2D vortex whip problem did not have to worry about any short- or long-wavelength instabilities in the flow. These types of instabilities are found in the 3D problem, where they can lead to the production of more vortices than initially present. Future researchers should keep these limitations in mind when they continue the work where this thesis ends.

Chapter 4

EXTENSION OF THE RESULTS

In the previous chapter, the results of nearly 8000 simulations of a multitude of configurations of a vortex whip were synthesized and analyzed. Recall that the configurations tested were motivated by a preliminary study performed in Chapter 2 where we varied select parameters individually and observed their effect(s) on a vortex whip's performance. One parameter that was looked at was the vortex strength. In the context of the 2D vortex whip problem, this parameter appears in the condition $\frac{\Gamma_2}{\Gamma_1} = \frac{\Gamma_3}{\Gamma_2}$. It was observed that the greater the strength of a vortex, the faster the weakest vortex gets pulled downward to the surface—as expected from the Biot-Savart law. Testing all possible values of vortex strength ratios is impossible, so it was judiciously decided to narrow the range of investigation to $1.1 \leq \frac{\Gamma_2}{\Gamma_1} = \frac{\Gamma_3}{\Gamma_2} \leq 3.0$. If we review the residence time contour plots from Tables 3.1-3.7, we generally see that the peaks appear at the greatest strength ratio value $\frac{\Gamma_2}{\Gamma_1} = 3.0$. It is natural to ask: what happens to the right, for greater values of $\frac{\Gamma_2}{\Gamma_1}$?

In this chapter, the results of nearly 8000 additional simulations are presented and analyzed. This chapter extends the results of the previous chapter for the range $3.1 \leq \frac{\Gamma_2}{\Gamma_1} = \frac{\Gamma_3}{\Gamma_2} \leq 5.0$. The extent of this range is exactly the same as before so we can compare and contrast any differences and similarities in the plots. All of the simulations were performed using the same time step $\Delta t = 0.2$ and the same number of total iterations, 125. There is no need to perform any additional calibration tests since the only thing we changed is the range of the vortex strength ratio. With these additional results, we will be able to answer the question we posed above.

4.1 Extended Results

The results of an additional 7980 simulations synthesized into 42 contour plots can be found in the following pages. Tables 4.1-4.7 organize the contour plots in pairs of three, one row for a fixed value of $\frac{d_2}{H}$, as in the previous chapter. The contour plots on the left-hand side (LHS) are contours of BB's minimum height above the wall. In these plots, the bluest region(s) (i.e. the lowest values) are the the ones we are most interested in. The contour plots on the right-hand side (RHS) are contours of BB's residence time[1]. As before, it is the red region(s) (i.e. the largest values) that we care about.

4.2 Discussion

Examining all of the contour plots obtained for this round of simulations, similar trends and patterns discussed in Chapter 3 hold true here as well. For brevity, please refer to the "Discussion" section of the previous chapter for a more in-depth exposition of these trends.

There are several outstanding differences for this set of results when compared to the previous set. For every $\frac{d_2}{H}$ value, notice that the peaks of the residence time plots in this case are higher than those peaks found in the corresponding contour plots in Chapter 3. This is expected since all of the vortices in our array have greater relative strength. Another difference is the $\frac{d_2}{H}$ value at which the peak residence time of BB seems to be. Other discrepancies will be discussed later after we compile all of the extrema data from the contour plots in one place to produce Fig. 4.1.

In spite of these differences, it remains true that the local maximum for BB's residence time is found at $\frac{d_1}{d_2} < 1$.

As in the previous chapter, three-dimensional surface plots of BB's minimum height and residence time have also been made to complement the contour plots. These can be found in Tables 4.8-4.14 for all of the corresponding contour plots featured in this chapter. The main

---

[1] Recall that in this thesis, the term *residence time* is used to refer to the time BB spends below the threshold line.

Nr.	a	b
43	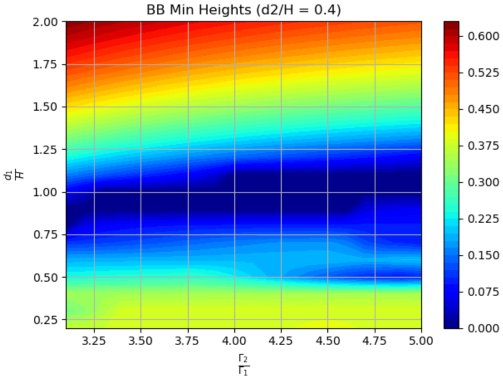	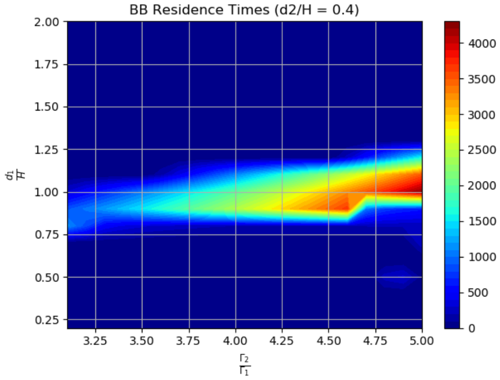
44	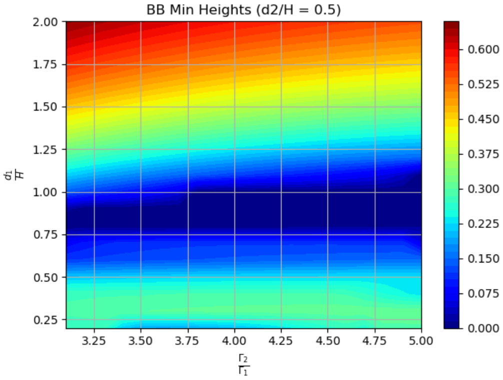	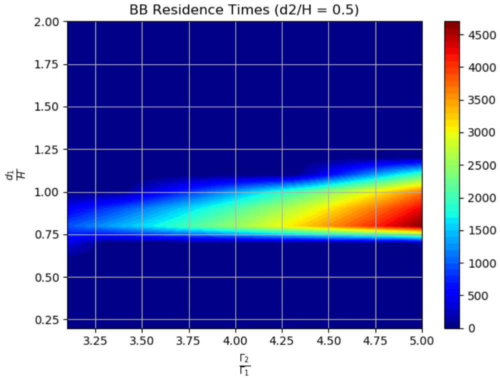
45	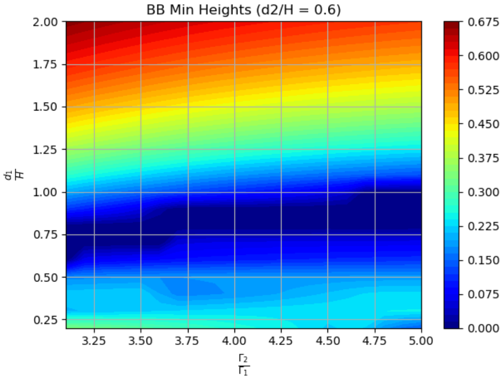	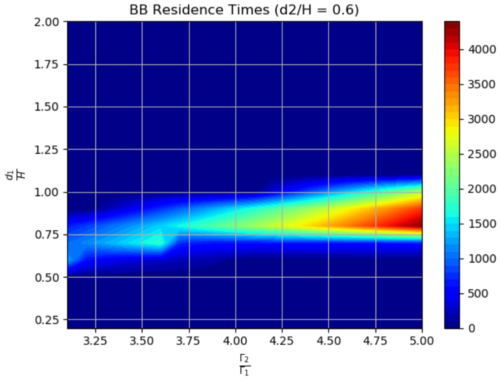

Table 4.1: Contour plots of BB's minimum height above the wall (LHS) and residence time below the threshold line of $0.1H$ (RHS). This set of plots have been created for the ratios $\frac{d_2}{H}$ = 0.4, 0.5, and 0.6, respectively. $\frac{\Gamma_2}{\Gamma_1} = 3.1$ - 5.0. SOR is (BB MB PB)=($+ - -$).

Nr.	a	b
46	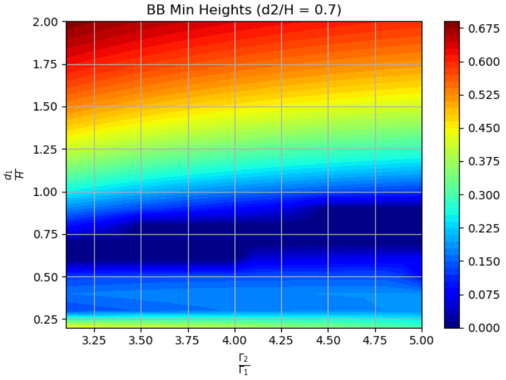 BB Min Heights (d2/H = 0.7)	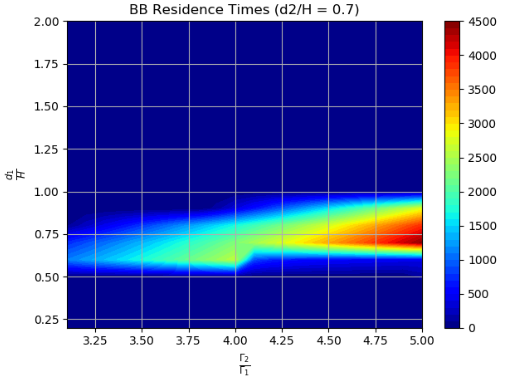 BB Residence Times (d2/H = 0.7)
47	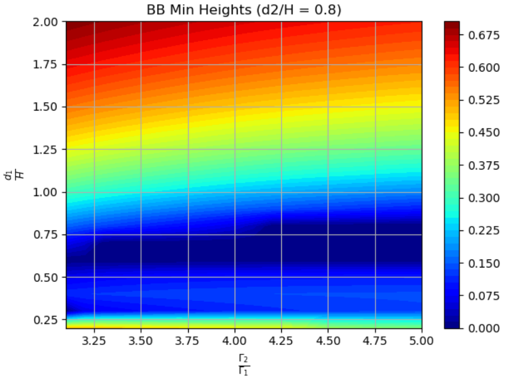 BB Min Heights (d2/H = 0.8)	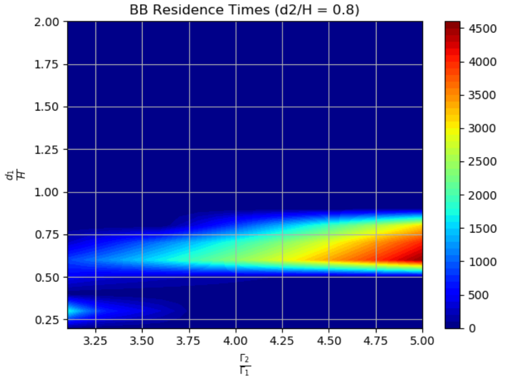 BB Residence Times (d2/H = 0.8)
48	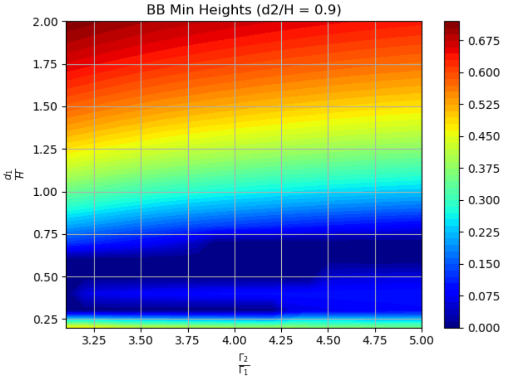 BB Min Heights (d2/H = 0.9)	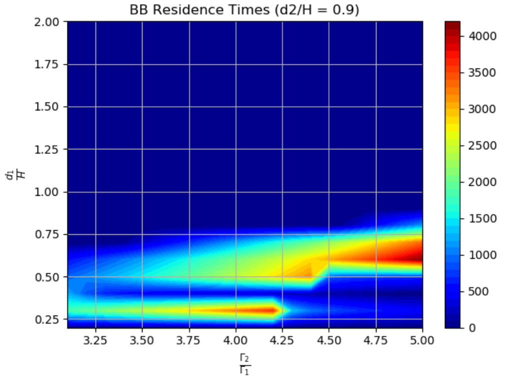 BB Residence Times (d2/H = 0.9)

Table 4.2: Contour plots of BB's minimum height above the wall (LHS) and residence time below the threshold line of $0.1H$ (RHS). This set of plots have been created for the ratios $\frac{d_2}{H}$ = 0.7, 0.8, and 0.9, respectively. $\frac{\Gamma_2}{\Gamma_1} = 3.1$ - 5.0. SOR is (BB MB PB)=$(+ - -)$.

Nr.	a	b
49	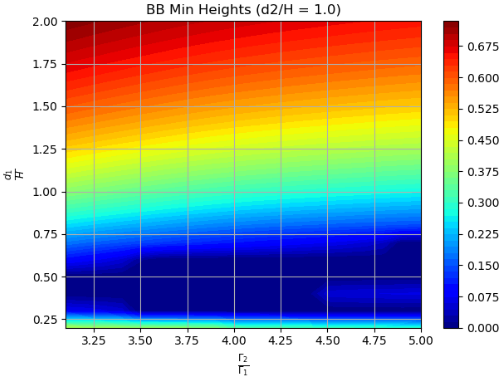 BB Min Heights (d2/H = 1.0)	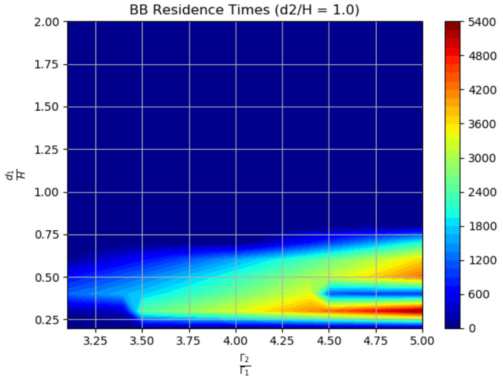 BB Residence Times (d2/H = 1.0)
50	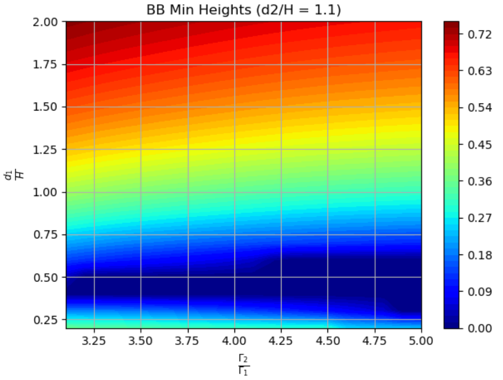 BB Min Heights (d2/H = 1.1)	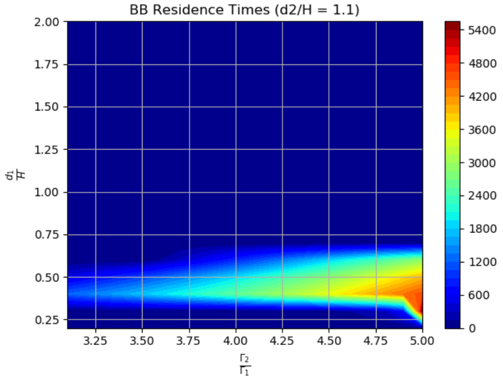 BB Residence Times (d2/H = 1.1)
51	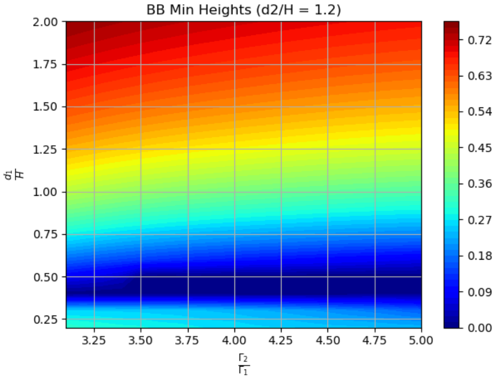 BB Min Heights (d2/H = 1.2)	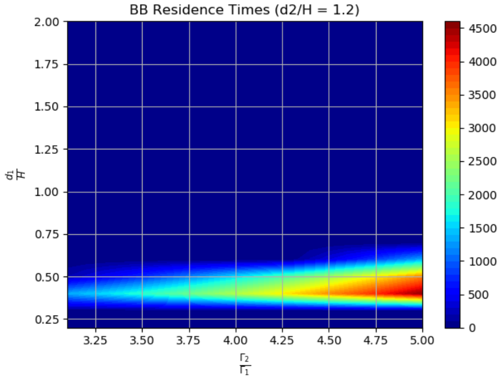 BB Residence Times (d2/H = 1.2)

Table 4.3: Contour plots of BB's minimum height above the wall (LHS) and residence time below the threshold line of $0.1H$ (RHS). This set of plots have been created for the ratios $\frac{d_2}{H}$ = 1.0, 1.1, and 1.2, respectively. $\frac{\Gamma_2}{\Gamma_1} = 3.1$ - 5.0. SOR is (BB MB PB)=(+ − −).

Nr.	a	b
52	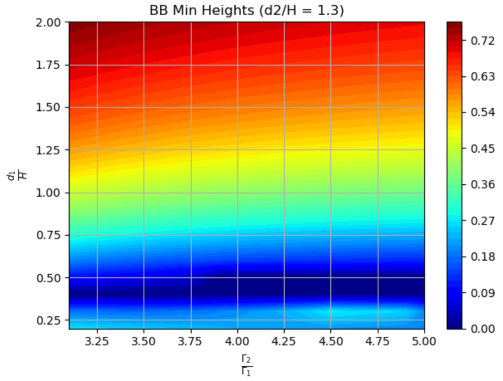	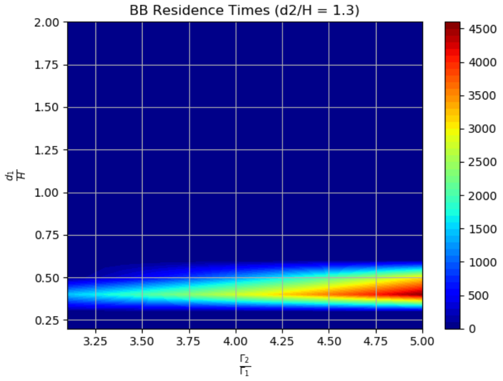
53	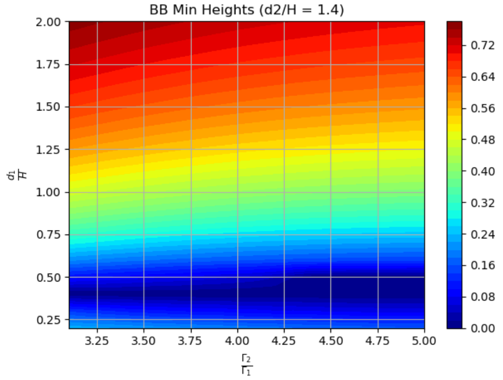	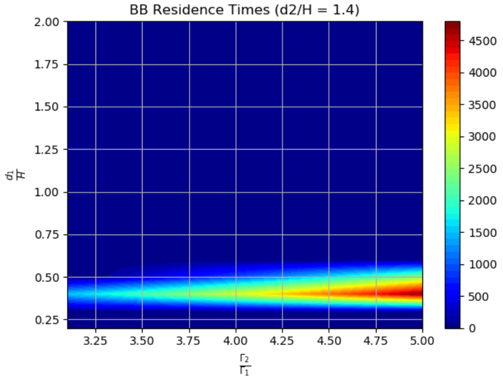
54	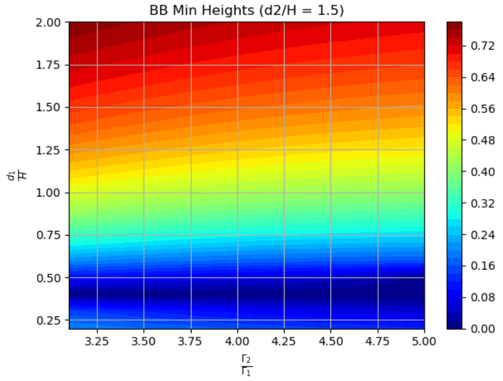	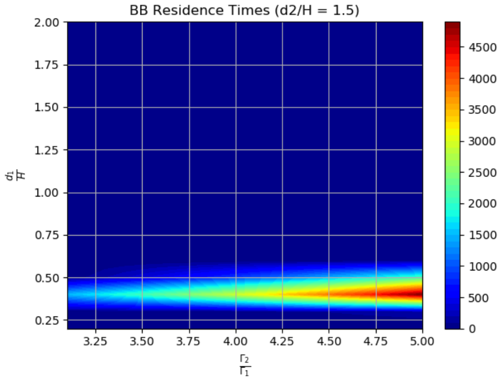

Table 4.4: Contour plots of BB's minimum height above the wall (LHS) and residence time below the threshold line of $0.1H$ (RHS). This set of plots have been created for the ratios $\frac{d_2}{H}$ = 1.3, 1.4, and 1.5, respectively. $\frac{\Gamma_2}{\Gamma_1}$ = 3.1 - 5.0. SOR is (BB MB PB)=(+ − −).

Nr.	a	b
55	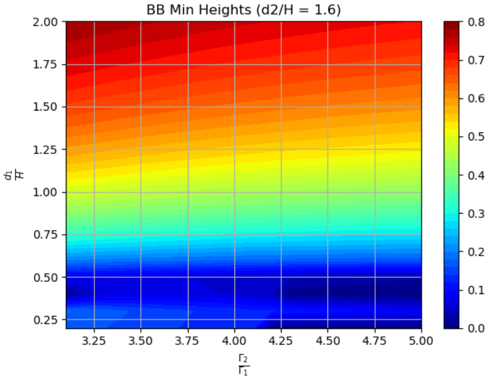 BB Min Heights (d2/H = 1.6)	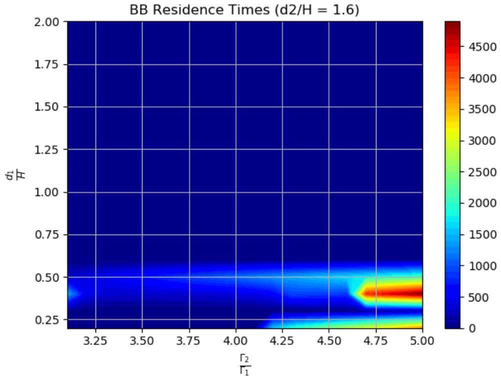 BB Residence Times (d2/H = 1.6)
56	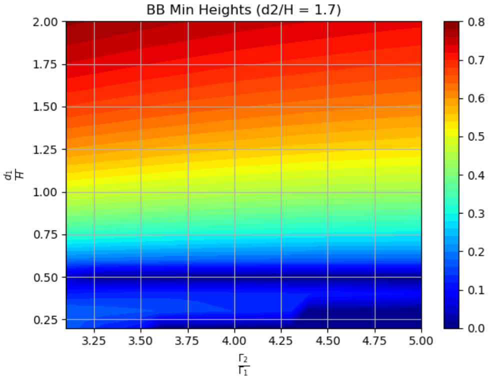 BB Min Heights (d2/H = 1.7)	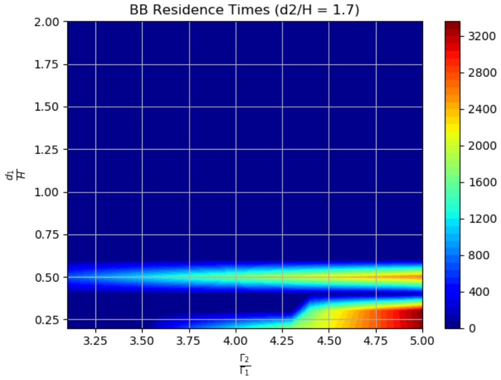 BB Residence Times (d2/H = 1.7)
57	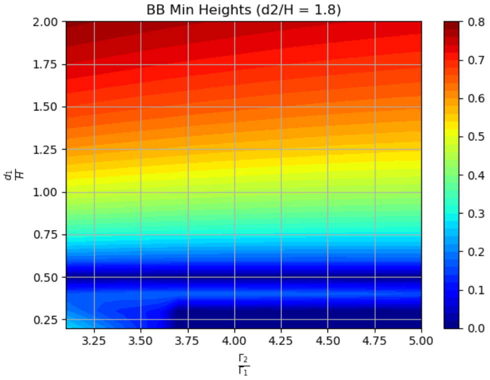 BB Min Heights (d2/H = 1.8)	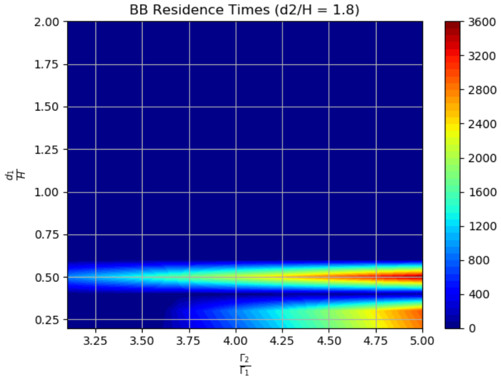 BB Residence Times (d2/H = 1.8)

Table 4.5: Contour plots of BB's minimum height above the wall (LHS) and residence time below the threshold line of $0.1H$ (RHS). This set of plots have been created for the ratios $\frac{d_2}{H}$ = 1.6, 1.7, and 1.8, respectively. $\frac{\Gamma_2}{\Gamma_1}$ = 3.1 - 5.0. SOR is (BB MB PB)=($+--$).

Nr.	a	b
58	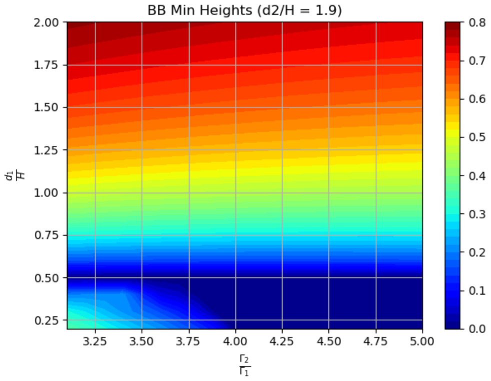 BB Min Heights (d2/H = 1.9) 	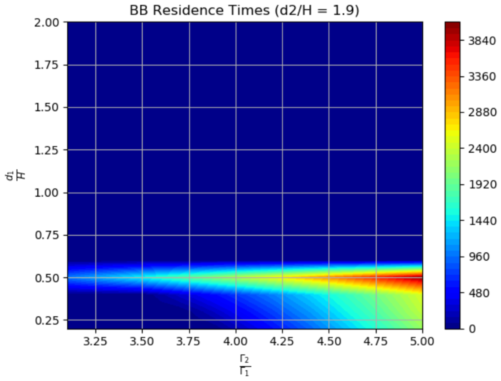 BB Residence Times (d2/H = 1.9)
59	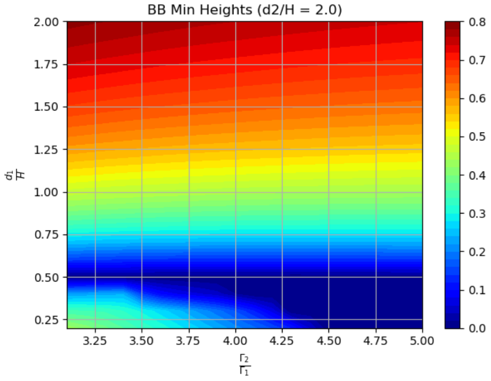 BB Min Heights (d2/H = 2.0) 	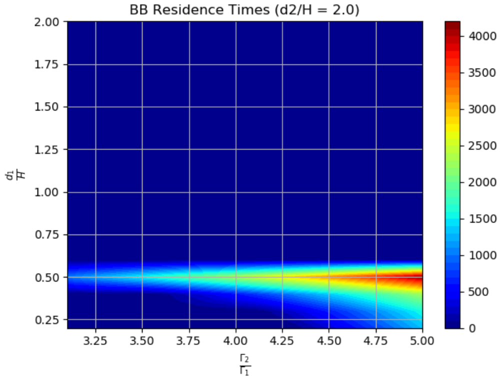 BB Residence Times (d2/H = 2.0)
60	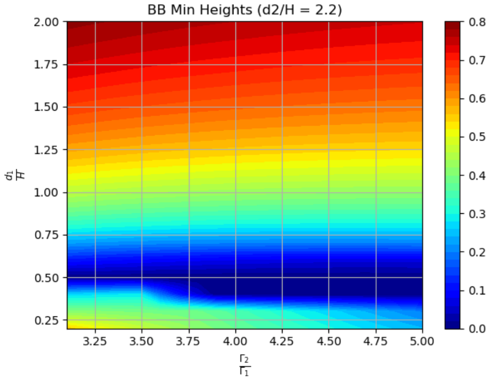 BB Min Heights (d2/H = 2.2) 	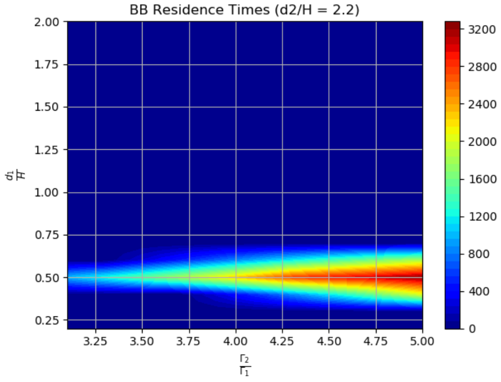 BB Residence Times (d2/H = 2.2)

Table 4.6: Contour plots of BB's minimum height above the wall (LHS) and residence time below the threshold line of $0.1H$ (RHS). This set of plots have been created for the ratios $\frac{d_2}{H}$ = 1.9, 2.0, and 2.2, respectively. $\frac{\Gamma_2}{\Gamma_1}$ = 3.1 - 5.0. SOR is (BB MB PB)=($+--$).

Nr.	a	b
61	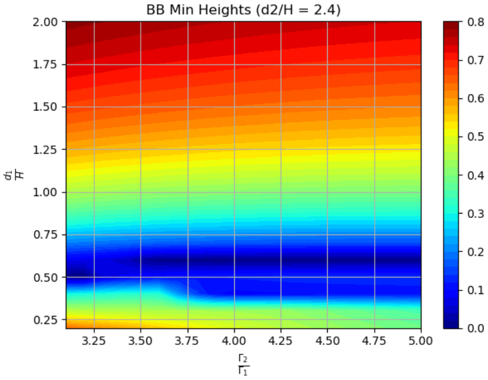 BB Min Heights (d2/H = 2.4)	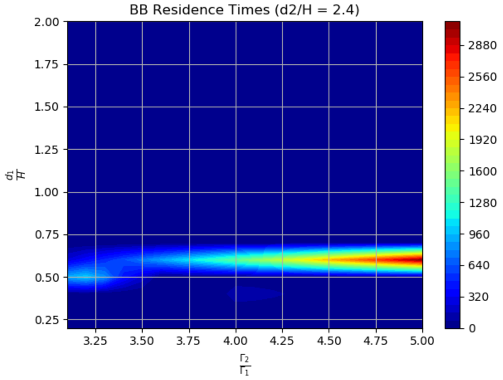 BB Residence Times (d2/H = 2.4)
62	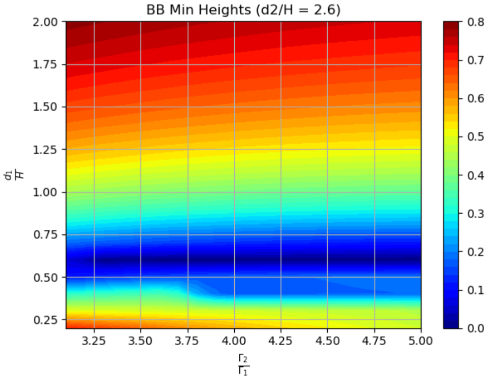 BB Min Heights (d2/H = 2.6)	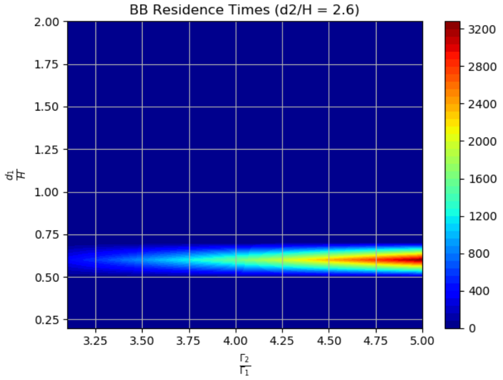 BB Residence Times (d2/H = 2.6)
63	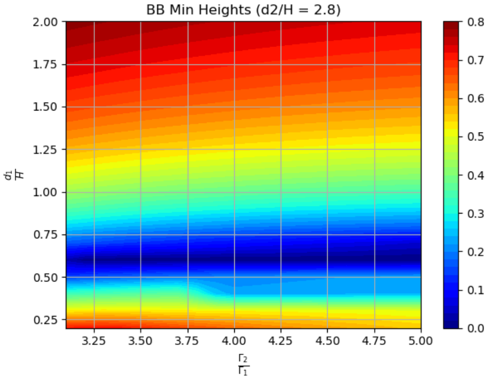 BB Min Heights (d2/H = 2.8)	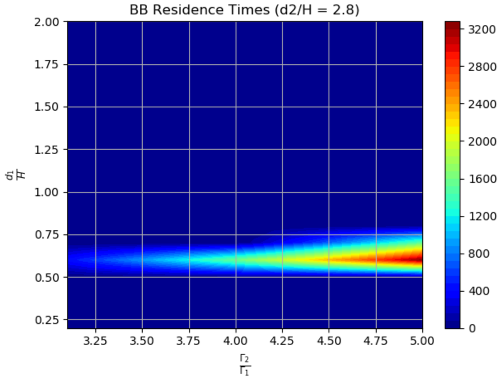 BB Residence Times (d2/H = 2.8)

Table 4.7: Contour plots of BB's minimum height above the wall (LHS) and residence time below the threshold line of $0.1H$ (RHS). This set of plots have been created for the ratios $\frac{d_2}{H}$ = 2.4, 2.6, and 2.8, respectively. $\frac{\Gamma_2}{\Gamma_1}$ = 3.1 - 5.0. SOR is (BB MB PB)=($+--$).

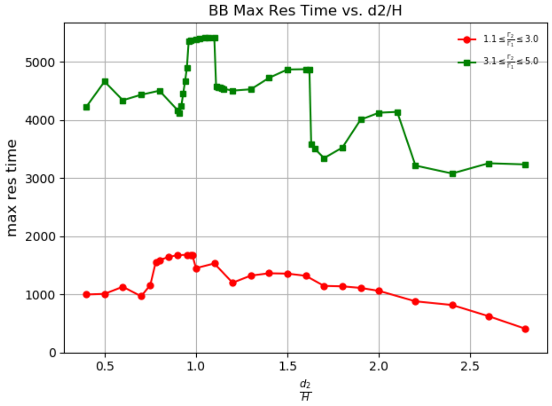

Figure 4.1: Graph of largest residence time from each contour plot from Tables 4.1-4.7 versus $\frac{d_2}{H}$.

surface plot is displayed in a grey color. The profile of the surface plot is projected onto all three respective coordinate planes to give additional perspective. Extrema points are labeled by either red or blue dots. Red dots indicate highest values and blue points indicate lowest values.

4.3 Compilation of Extended Results

As previously done, it is useful to combine all of the important results contained in our contour and surface plots into one so we can determine any emergent patterns. Figure 4.1 compiles the largest residence time from each row of Tables 4.1-4.7 and plots them against the appropriate ratio $\frac{d_2}{H}$. Additional simulations were performed to collect more data points around various peaks, hence the increased density of points in some portions of the graphs but not others. For all values of $\frac{d_2}{H}$, the smallest minimum height calculated from each row of Tables 4.1-4.7 is zero.

From Fig. 4.1, we can see that the maximum residence time is located around $\frac{d_2}{H} = 1.1$, where $\frac{d_1}{H} = 0.3$. This is a novel result! When $1.1 \leq \frac{\Gamma_2}{\Gamma_1} \leq 3.0$, the peak residence time appeared where d_2—the separation distance between the medium strength and strongest

Nr.	a	b
64	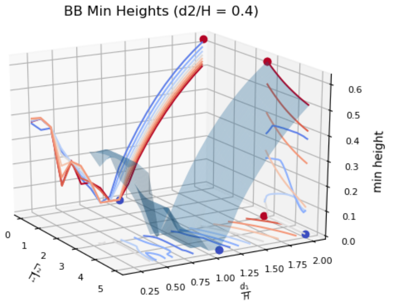	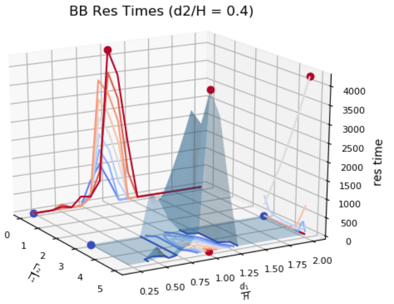
65	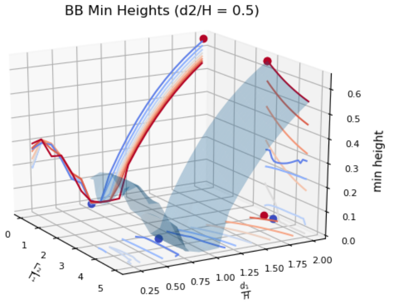	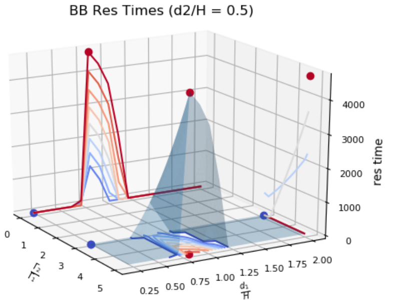
66	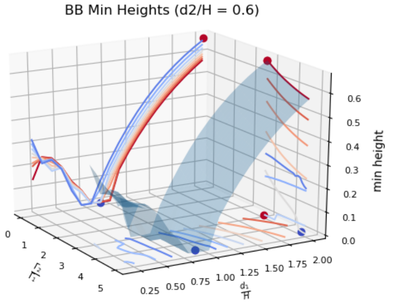	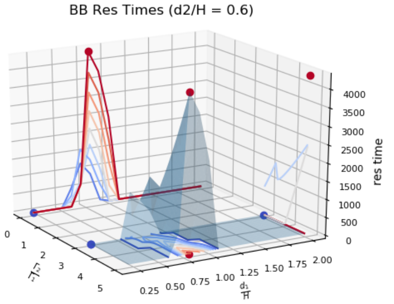

Table 4.8: Three-dimensional surface plots of BB's minimum height above the wall (LHS) and residence time below the threshold line of $0.1H$ (RHS). $\frac{d_2}{H}$ = 0.4, 0.5, and 0.6, respectively. $\frac{\Gamma_2}{\Gamma_1}$ = 3.1 - 5.0. SOR is (BB MB PB)=$(+--)$.

Nr.	a	b
67	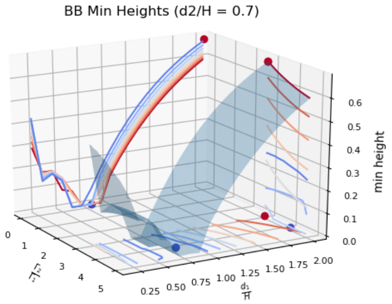 BB Min Heights (d2/H = 0.7)	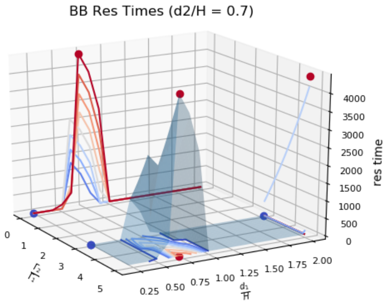 BB Res Times (d2/H = 0.7)
68	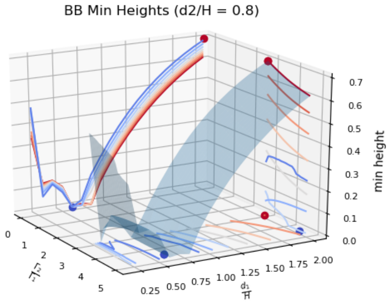 BB Min Heights (d2/H = 0.8)	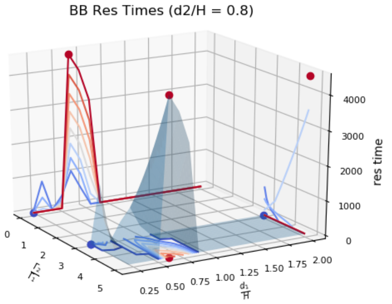 BB Res Times (d2/H = 0.8)
69	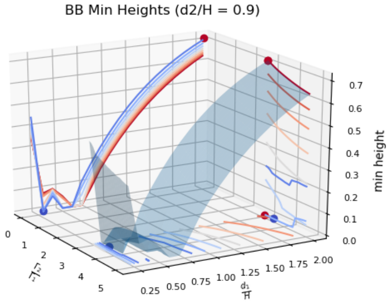 BB Min Heights (d2/H = 0.9)	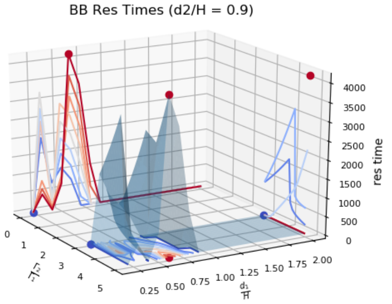 BB Res Times (d2/H = 0.9)

Table 4.9: Three-dimensional surface plots of BB's minimum height above the wall (LHS) and residence time below the threshold line of $0.1H$ (RHS). $\frac{d_2}{H} = 0.7$, 0.8, and 0.9, respectively. $\frac{\Gamma_2}{\Gamma_1} = 3.1$ - 5.0. SOR is (BB MB PB)=$(+--)$.

Nr.	a	b
70	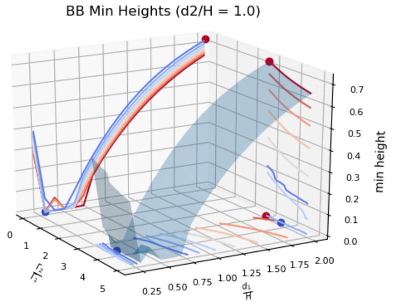	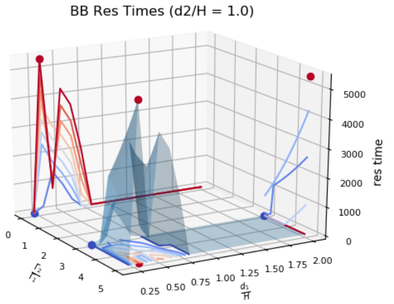
71	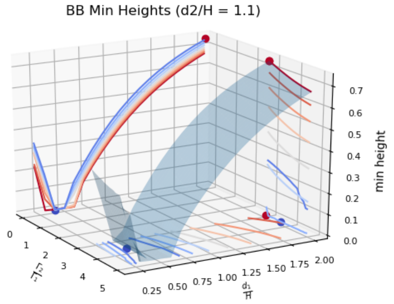	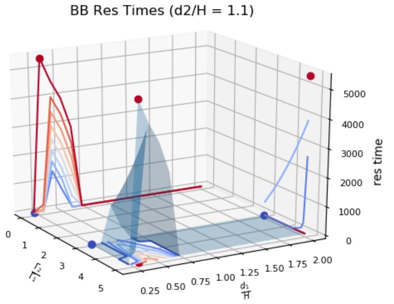
72	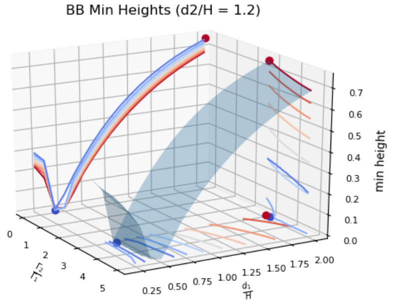	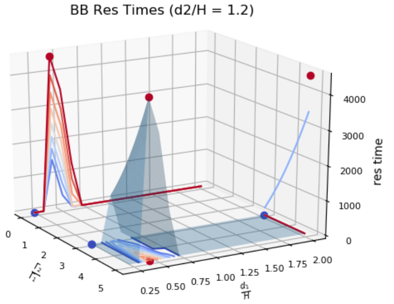

Table 4.10: Three-dimensional surface plots of BB's minimum height above the wall (LHS) and residence time below the threshold line of $0.1H$ (RHS). $\frac{d_2}{H} = 1.0$, 1.1, and 1.2, respectively. $\frac{\Gamma_2}{\Gamma_1} = 3.1$ - 5.0. SOR is (BB MB PB)=($+ - -$).

Nr.	a	b
73	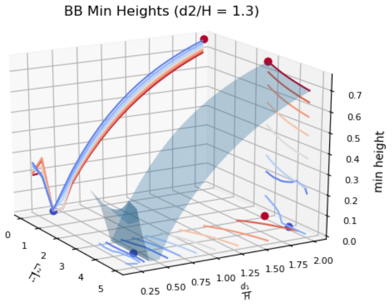 BB Min Heights (d2/H = 1.3)	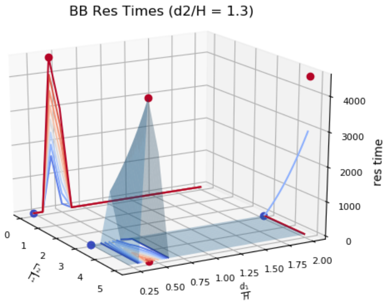 BB Res Times (d2/H = 1.3)
74	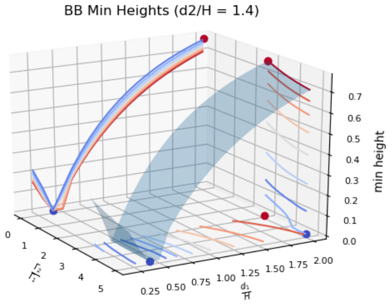 BB Min Heights (d2/H = 1.4)	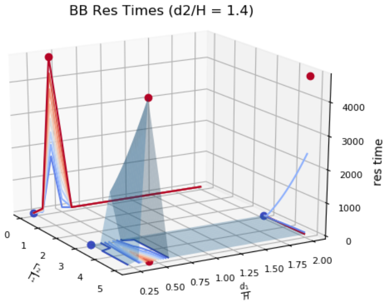 BB Res Times (d2/H = 1.4)
75	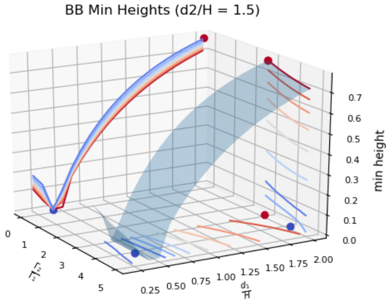 BB Min Heights (d2/H = 1.5)	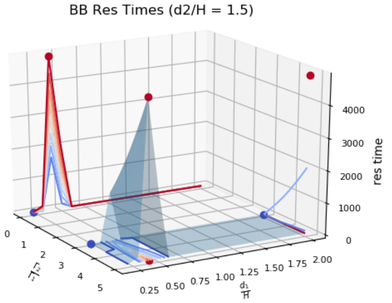 BB Res Times (d2/H = 1.5)

Table 4.11: Three-dimensional surface plots of BB's minimum height above the wall (LHS) and residence time below the threshold line of $0.1H$ (RHS). $\frac{d_2}{H} = 1.3$, 1.4, and 1.5, respectively. $\frac{\Gamma_2}{\Gamma_1} = 3.1$ - 5.0. SOR is (BB MB PB)=$(+--)$.

Nr.	a	b
76	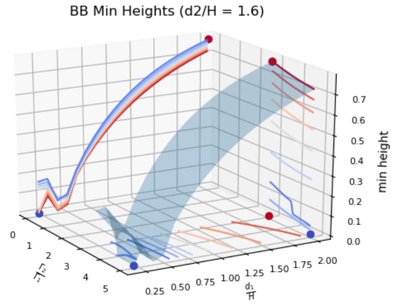	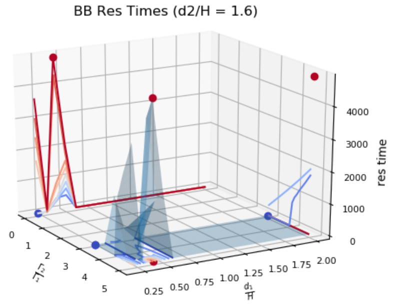
77	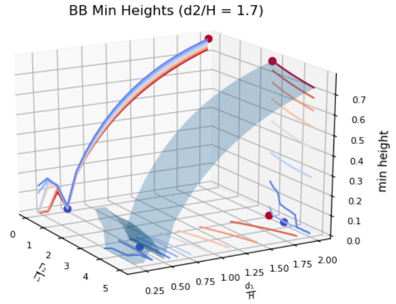	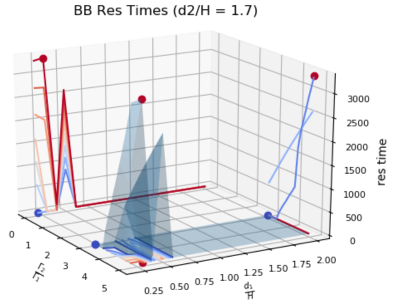
78	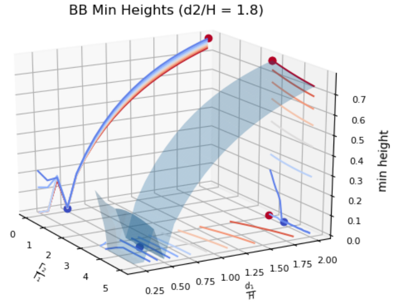	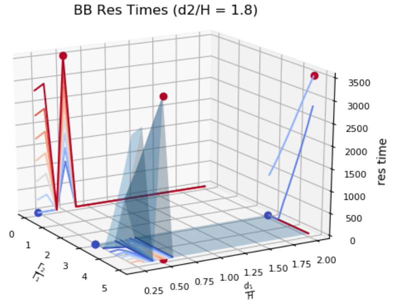

Table 4.12: Three-dimensional surface plots of BB's minimum height above the wall (LHS) and residence time below the threshold line of $0.1H$ (RHS). $\frac{d_2}{H} = 1.6$, 1.7, and 1.8, respectively. $\frac{\Gamma_2}{\Gamma_1} = 3.1$ - 5.0. SOR is (BB MB PB)=$(+--)$.

Nr.	a	b
79	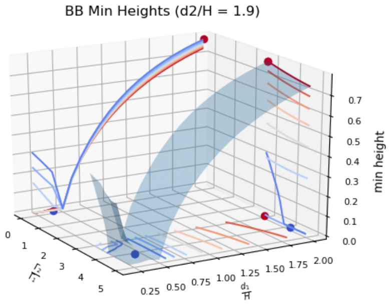 BB Min Heights (d2/H = 1.9)	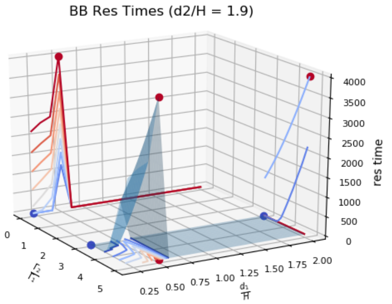 BB Res Times (d2/H = 1.9)
80	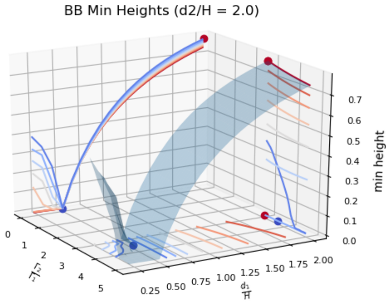 BB Min Heights (d2/H = 2.0)	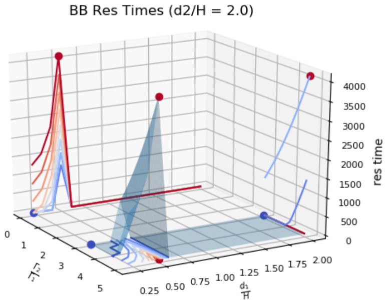 BB Res Times (d2/H = 2.0)
81	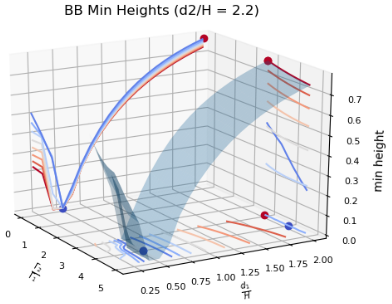 BB Min Heights (d2/H = 2.2)	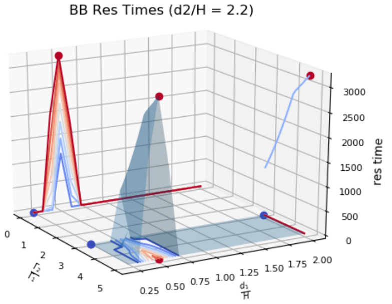 BB Res Times (d2/H = 2.2)

Table 4.13: Three-dimensional surface plots of BB's minimum height above the wall (LHS) and residence time below the threshold line of $0.1H$ (RHS). $\frac{d_2}{H} = 1.9$, 2.0, and 2.2, respectively. $\frac{\Gamma_2}{\Gamma_1} = 3.1$ - 5.0. SOR is (BB MB PB)=$(+--)$.

Nr.	a	b
82	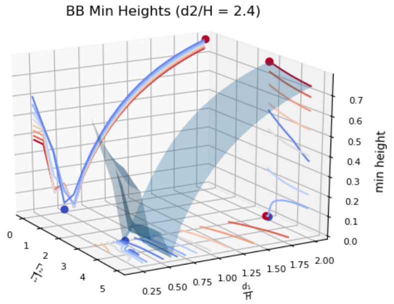 BB Min Heights (d2/H = 2.4)	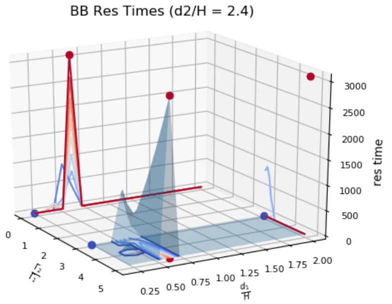 BB Res Times (d2/H = 2.4)
83	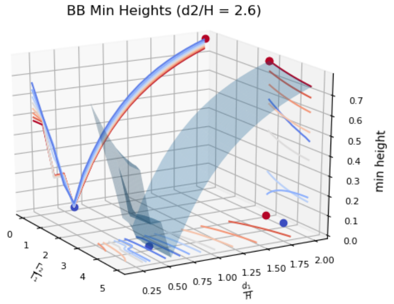 BB Min Heights (d2/H = 2.6)	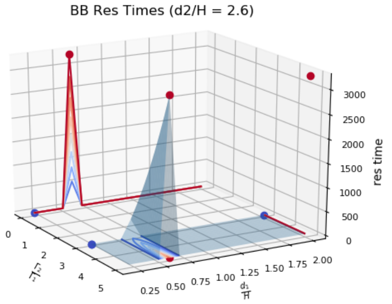 BB Res Times (d2/H = 2.6)
84	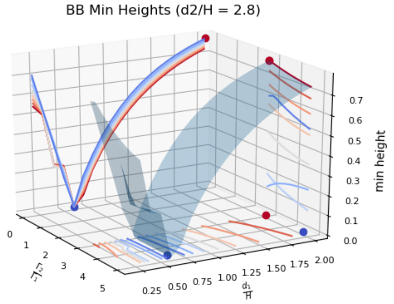 BB Min Heights (d2/H = 2.8)	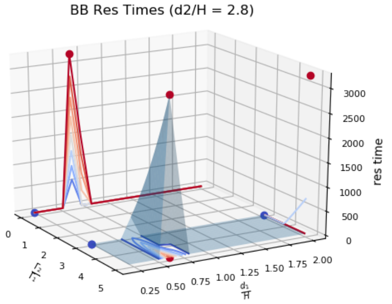 BB Res Times (d2/H = 2.8)

Table 4.14: Three-dimensional surface plots of BB's minimum height above the wall (LHS) and residence time below the threshold line of $0.1H$ (RHS). $\frac{d_2}{H} = 2.4$, 2.6, and 2.8, respectively. $\frac{\Gamma_2}{\Gamma_1} = 3.1$ - 5.0. SOR is (BB MB PB)=$(+--)$.

strength vortices—is close to the vortices' initial height above the wall, but not exceeding it. But as we can see here, increasing the relative strength ratio of the vortices modified the performance of our vortex whip. Now it is found that d_2 should be equal to or a little greater than the vortices' initial height above the wall. The physics of this behavior makes sense. If all of the vortices carry greater energy, they can induce greater changes in velocity on the neighboring vortices. The separation distance between the vortices should increase slightly to offset the increased strength in order to induce just enough velocity change on the weakest vortex—but not too much—so that it moves at the right speed below the $0.1H$ threshold line.

Similar to Fig. 3.9, the green curve in Fig. 4.1 exhibits a non-smooth behavior. Take the peak where $0.7 \leq \frac{d_2}{H} \leq 1.3$, for example. This region of parameter space has interesting wiggles which may or may not be physical for the 3D viscous case. But based on the simulations performed, it looks like these situations are the optimal configurations that have the best chance of future success in real life.

The non-smooth nature of the curve in Fig. 4.1 also suggests something about the resolution of our simulations in some regions. Take the kink at $\frac{d_2}{H} = 1.63$. This kink seems to suggest that data points nearby it should be raised up higher to produce a smoother falloff for the overall curve. There are other regions of Fig. 4.1 that look like they can benefit from increased resolution to give the overall curve a smoother shape. Despite this, the peak in the current figure is still an outstanding feature that indicates a local maximum.

Every contour plot of BB's minimum height above the wall and BB's residence time below the $0.1H$ threshold line has a minimum and a maximum. Tables 4.15 and 4.16 identify what these extrema points are for each of the contour plots from Tables 4.1-4.7. They supplement Fig. 4.1 with additional information.

4.4 Where Do We Go From Here?

Most of the contour plots in Tables 4.1-4.7 indicate once more that the extrema generally appear where $\frac{\Gamma_2}{\Gamma_1}$ has the greatest value. Even though performing 7980 additional simulations

$\frac{d_2}{H}$	$\frac{\Gamma_2}{\Gamma_1}$ **min**	$\frac{d_1}{H}$ **min**	**minHeight (min)**	$\frac{\Gamma_2}{\Gamma_1}$ **max**	$\frac{d_1}{H}$ **max**	**minHeight (max)**
0.4	5.0	1.1	0.0	3.1	2.0	0.63
0.5	3.5	0.8	0.0	3.1	2.0	0.65
0.6	4.8	0.9	0.0	3.1	2.0	0.67
0.7	4.3	0.8	0.0	3.1	2.0	0.69
0.8	4.7	0.6	0.0	3.1	2.0	0.7
0.9	3.5	0.3	0.0	3.1	2.0	0.72
0.91	4.8	0.7	0.0	3.1	2.0	0.72
0.92	3.4	0.5	0.0	3.1	2.0	0.72
0.93	3.3	0.3	0.0	3.1	2.0	0.72
0.94	3.5	0.3	0.0	3.1	2.0	0.72
0.95	3.4	0.4	0.0	3.1	2.0	0.72
0.96	3.6	0.6	0.0	3.1	2.0	0.73
0.97	3.5	0.5	0.0	3.1	2.0	0.73
1.0	3.8	0.3	0.0	3.1	2.0	0.73
1.02	3.9	0.3	0.0	3.1	2.0	0.73
1.05	5.0	0.6	0.0	3.1	2.0	0.74
1.07	4.2	0.5	0.0	3.1	2.0	0.74
1.1	3.8	0.4	0.0	3.1	2.0	0.74
1.11	3.5	0.5	0.0	3.1	2.0	0.74
1.12	4.5	0.5	0.0	3.1	2.0	0.74
1.13	4.8	0.5	0.0	3.1	2.0	0.74
1.14	3.9	0.4	0.0	3.1	2.0	0.75
1.15	4.4	0.4	0.0	3.1	2.0	0.75
1.2	3.3	0.4	0.0	3.1	2.0	0.75
1.3	4.2	0.4	0.0	3.1	2.0	0.76
1.4	5.0	0.4	0.0	3.1	2.0	0.77
1.5	4.3	0.4	0.0	3.1	2.0	0.78
1.6	5.0	0.2	0.0	3.1	2.0	0.78
1.62	4.0	0.2	0.0	3.1	2.0	0.78
1.63	4.8	0.2	0.0	3.1	2.0	0.78
1.65	4.8	0.5	0.0	3.1	2.0	0.78
1.7	3.8	0.5	0.0	3.1	2.0	0.78
1.8	3.8	0.5	0.0	3.1	2.0	0.79
1.9	4.3	0.4	0.0	3.1	2.0	0.79
2.0	3.7	0.5	0.0	3.1	2.0	0.79
2.1	4.3	0.5	0.0	3.1	2.0	0.79
2.2	4.2	0.5	0.0	3.1	2.0	0.79
2.4	3.2	0.5	0.0	3.1	2.0	0.79
2.6	3.9	0.6	0.0	3.1	2.0	0.79
2.8	4.8	0.6	0.0	3.1	2.0	0.79

Table 4.15: Summary of all the extrema points (minima and maxima) for every contour plot of BB's height above the wall. These results are for $\frac{\Gamma_2}{\Gamma_1} = 3.1$ - 5.0.

$\frac{d_2}{H}$	$\frac{\Gamma_2}{\Gamma_1}$ **min**	$\frac{d_1}{H}$ **min**	**resTime (min)**	$\frac{\Gamma_2}{\Gamma_1}$ **max**	$\frac{d_1}{H}$ **max**	**resTime (max)**
0.4	3.1	0.2	0.0	5.0	1.0	4223.4
0.5	3.1	0.2	0.0	5.0	0.8	4659.93
0.6	3.1	0.2	0.0	5.0	0.8	4337.77
0.7	3.1	0.2	0.0	5.0	0.7	4432.15
0.8	3.1	0.2	0.0	5.0	0.6	4502.36
0.9	3.1	0.2	0.0	5.0	0.6	4165.07
0.91	3.1	0.2	0.0	5.0	0.6	4124.44
0.92	3.1	0.2	0.0	4.9	0.5	4242.75
0.93	3.1	0.2	0.0	5.0	0.5	4456.38
0.94	3.1	0.2	0.0	4.7	0.3	4660.24
0.95	3.1	0.2	0.0	4.8	0.3	4889.67
0.96	3.1	0.2	0.0	5.0	0.3	5350.61
0.97	3.1	0.2	0.0	5.0	0.3	5361.4
1.0	3.1	0.2	0.0	5.0	0.3	5390.99
1.02	3.1	0.2	0.0	5.0	0.3	5405.15
1.05	3.1	0.2	0.0	5.0	0.3	5416.47
1.07	3.1	0.2	0.0	5.0	0.3	5418.68
1.1	3.1	0.2	0.0	5.0	0.3	5412.7
1.11	3.1	0.2	0.0	5.0	0.4	4572.4
1.12	3.1	0.2	0.0	5.0	0.4	4562.61
1.13	3.1	0.2	0.0	5.0	0.4	4553.26
1.14	3.1	0.2	0.0	5.0	0.4	4544.23
1.15	3.1	0.2	0.0	5.0	0.4	4535.68
1.2	3.1	0.2	0.0	5.0	0.4	4503.73
1.3	3.1	0.2	0.0	5.0	0.4	4526.28
1.4	3.1	0.2	0.0	5.0	0.4	4724.47
1.5	3.1	0.2	0.0	5.0	0.4	4867.0
1.6	3.1	0.2	0.0	5.0	0.4	4872.19
1.62	3.1	0.2	0.0	5.0	0.4	4862.87
1.63	3.1	0.2	0.0	5.0	0.2	3579.41
1.65	3.1	0.2	0.0	5.0	0.2	3500.97
1.7	3.1	0.2	0.0	5.0	0.3	3342.44
1.8	3.1	0.2	0.0	5.0	0.5	3522.98
1.9	3.1	0.2	0.0	5.0	0.5	4003.46
2.0	3.1	0.2	0.0	5.0	0.5	4123.37
2.1	3.1	0.2	0.0	5.0	0.5	4137.61
2.2	3.1	0.2	0.0	5.0	0.5	3213.79
2.4	3.1	0.2	0.0	5.0	0.6	3077.98
2.6	3.1	0.2	0.0	5.0	0.6	3254.03
2.8	3.1	0.2	0.0	5.0	0.6	3233.94

Table 4.16: Summary of all the extrema points (minima and maxima) for every contour plot of BB's residence time below the $0.1H$ threshold. This table supplements Fig. 4.1 with additional information. These results are for $\frac{\Gamma_2}{\Gamma_1}$ = 3.1 - 5.0.

using $3.1 \leq \frac{\Gamma_2}{\Gamma_1} \leq 5.0$ offered us additional insights into the parameter space of the 2D vortex whip problem, it may seem like we have not done enough and that we could continue to go out into greater values of $\frac{\Gamma_2}{\Gamma_1}$. Of course—in theory—we could! But the ultimate goal is to apply the results of this research to optimize a real, physical array of vortex generators comprising a vortex whip to inhibit boundary layer separation in places like airplane wings. The strength of the vortices a VG creates is proportional to its angle of attack (AOA) relative to the incoming flow[2], and there is a practical limit to what this AOA can be to be effective in applications: 90 degrees. Moreover, the maximum angle at which a VG is placed on an airplane wing to be effective is most likely well shy of 90 degrees. Literature on previous optimal VG arrangements studies typically reported less than 30 degrees for VG placement relative to the free stream [51].

It is also important to note that as the relative strengths of the vortices increase, they possess more energy. If the energy is great enough, the vortices will begin to exhibit chaotic behavior, "ricocheting" from the wall instead of residing over it as desired. Furthermore, extreme values of the circulation ratio are likely to be more rapidly influenced by 3D instabilities, thereby invalidating the 2D approximation. Another way to look at this is that the time scale for 3D instabilities goes like the length scale squared divided by the circulation of the strongest vortex. If we have too strong a vortex for PB in comparison to MB or BB, then the 3D time scale will be shortened and that will more rapidly invalidate any 2D solutions. Keep in mind that what we are looking for in this thesis, especially for early times, are good trajectories for BB—the weakest vortex. All simulation results reported have the best validity towards real life at early times before there is sufficient time for instabilities and viscous effects to kick in. At large times, reality will differ significantly in the real world 3D case from our 2D potential flow idealization, so there is not even a need to put too much weight on the 2D results then. Hence we are justified in not pursuing extreme values of strength ratio.

---

[2] It is possible to achieve a given vortex strength by adjusting the VG chord as well as the angle of attack.

With these considerations in mind, it is reasonable on a practical level to end our investigation at a strength ratio of $\frac{\Gamma_2}{\Gamma_1} = \frac{\Gamma_3}{\Gamma_2} = 5.0$. In an array of three VGs, suppose one VG is placed at 30° (this VG represents Papa Bear and would create the strongest vortices). Imposing the condition that $\Gamma_1 < \Gamma_2 < \Gamma_3$ and $\frac{\Gamma_2}{\Gamma_1} = \frac{\Gamma_3}{\Gamma_2} = 5.0$, it follows that the other two VGs would be placed at 6° and 1.2°, respectively, relative to the free stream. These angles are certainly very practical and lie well within the range of angles that VGs have been customarily used in commercial applications.

4.5 Estimating the Performance of a Vortex Whip

The best way to obtain measurements of how much better a vortex whip performs compared to a standard VG array is to measure relevant quantities of interest (e.g. its drag on a flat plate) in a lab. While this effort is not within the scope of this thesis and is suggested as a potential project for future researchers, we can make a rough estimate of how much better a vortex whip would perform compared to a standard VG array indirectly. Fortunately, Pearcey *et al.* [3] had done some 2D potential flow calculations for systems of counter-rotating vortices. Figure 4.2 shows Pearcey's vortex trajectories on the left and this thesis's Baby Bear trajectory at the optimal configuration found for $3.1 \leq \frac{\Gamma_2}{\Gamma_1} \leq 5.0$ on the right. In Fig. 4.2a, U is the free stream velocity, K is the vortex strength, h is the vortex height, d and D are parameters of the configuration illustrated above the graph, c is chord length, and x is the distance downstream from where the vortex originated. In the same figure, we can see one trajectory (curve B) where the vortex quickly approaches the wall but then quickly springs up. Another trajectory shows a vortex going down more slowly, does not get quite as low, but it stays down longer (curve C). Baby Bear in our simulation gets a lot closer to the wall in our optimal situation than any vortex in Pearcey[3]. In all cases in Pearcey, the vortices go down and then they all ultimately leave the wall because with an array of counter-rotating vortices, sooner or later a vortex would bump up against another vortex

---

[3] On Pearcey's plots, there is no Baby Bear; there is just Papa Bear and Papa Bear's partner.

of opposite sign and they would convect themselves away from the wall. None of Pearcey's vortices get down to $0.1H$. We are beating Pearcey by a lot in this regard. He also did not have any vortices that had a residence time below $0.1H$, whereas we achieved this. We also demonstrated that BB pretty quickly gets to the wall.

The above discussion indirectly shows how much better a vortex whip can perform compared to a standard VG array. The figure of merit for VG performance, however, is how well it inhibits separation. So we have to go from simply quoting the vortex position to some kind of model for how a vortex's position inhibits separation. We can make a rough quantitative estimate of how much better a vortex whip performs over a standard VG array using the velocity profile of a turbulent boundary layer for a flat plate and the Bernoulli equation in differential form,

$$dp = -\rho U dU \tag{4.1}$$

This is the real explanation for why boundary layers separate. For a finite pressure change, we have

$$\Delta p = -\rho U \Delta U \tag{4.2}$$

The mean velocity profile of a turbulent boundary layer for a flat plate, shown previously in Chapter 1, is reproduced here in Fig. 4.3 for convenience. Imagine that it is possible to transport a fluid element from the edge of the boundary layer down to the height that Pearcey achieved. Let us take the lowest vortex height from Fig. 4.2a (curve B), which is about 0.7. If we define ΔU to be the difference between the free stream velocity and the velocity profile of the boundary layer at that height, then according to Fig. 4.3,

$$\Delta U_{\text{Pearcey}} \approx U - 0.9U = 0.1U \tag{4.3}$$

We repeat the calculation again, but this time, let us imagine bringing a fluid element down to the lower height that BB achieved in this work. To be on the side of caution, we take the lowest height of BB to be 0.1. It follows that

$$\Delta U_{\text{Thesis}} \approx U - 0.75U = 0.25U \tag{4.4}$$

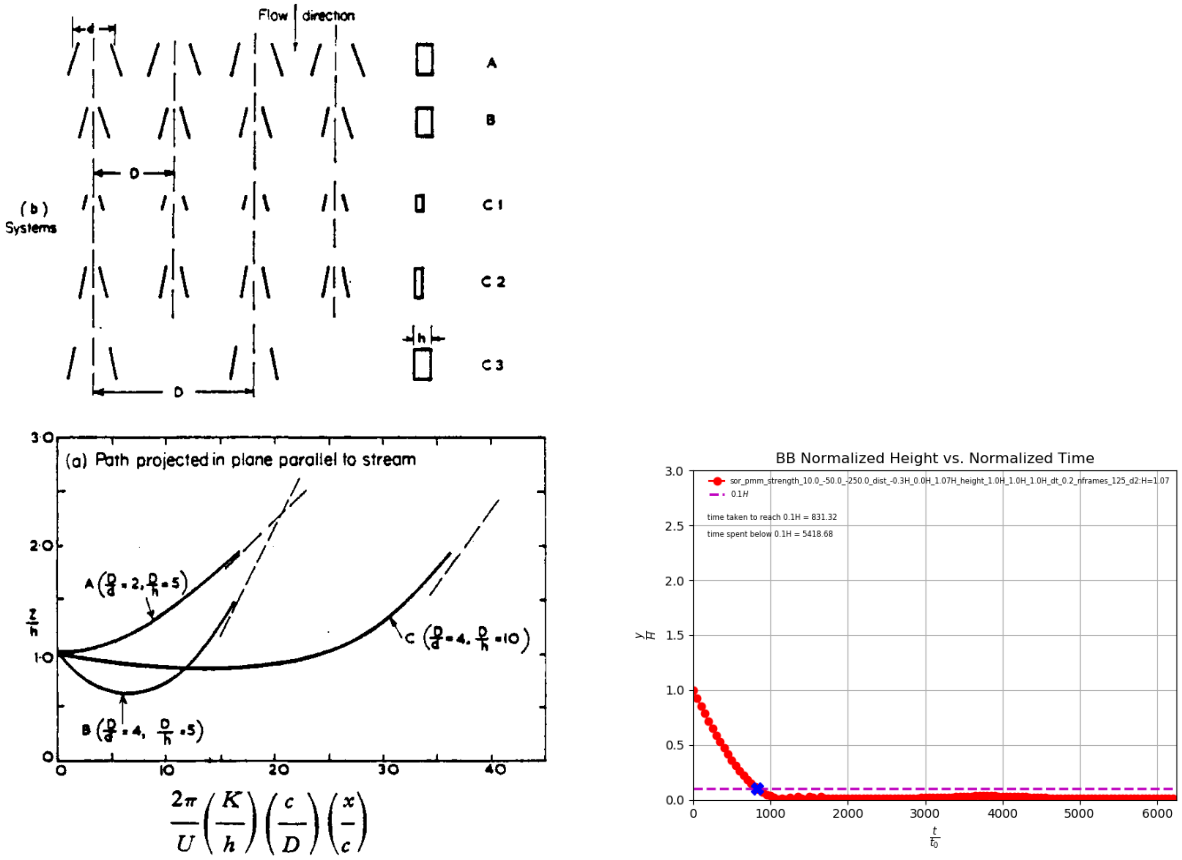

(a) (b)

Figure 4.2: Comparison between Pearcey's vortex trajectories with this thesis's. (a) Path of vortex from counter-rotating systems, projected in plane parallel to stream. See text for description of variables. Image from Pearcey [3]. (b) Path of Baby Bear using the optimal parameters found for $3.1 \leq \frac{\Gamma_2}{\Gamma_1} \leq 5.0$.

Substituting Eqs. (4.3) and (4.4) into the Bernoulli equation respectively, and taking the ratio of the resulting expressions, gives

$$\frac{\Delta p_{\text{Thesis}}}{\Delta p_{\text{Pearcey}}} = \frac{-\rho U * 0.25U}{-\rho U * 0.1U} = 2.5 \tag{4.5}$$

The above is most likely an overestimate, but as an extremely rough estimate, it shows incredible potential for how a vortex whip can change the game over an existing VG array.

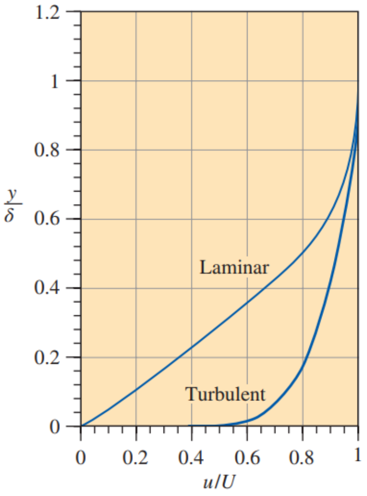

Figure 4.3: Comparison of laminar and turbulent flat plate boundary layer velocity profiles. The vertical axis is nondimensionalized by boundary layer thickness. Image from Cengel [49].

Again, the true test of how vortex whips hold up against standard VG arrays is through experimentation. The 2D simulations conducted in this thesis are really meant to provide guidance all along for solving the viscous, 3D case. If it turns out that the vortex whip strategy works, at least for short times, then our results will be the first real guidance on a geometry for VG devices that may end up on every commercial airliner in the world. Conversely, it may turn out that 3D instabilities and viscous effects drastically change the view of what really happens—we do not currently know. In any event, the basic physics of 2D vortex dynamics and the results of our optimization work currently give us much hope.

4.6 A Sketch of the Vortex Whip

Just what does a vortex whip look like? In this section, a sketch is presented to give concrete visualization of what sort of VG plus flow field arrangement would correspond to our 2D simulations. Figure 4.4 shows an array of three delta-winglet vortex generators on the upper surface of a lifting wing. Each VG in this drawing is characterized by its height h, chord

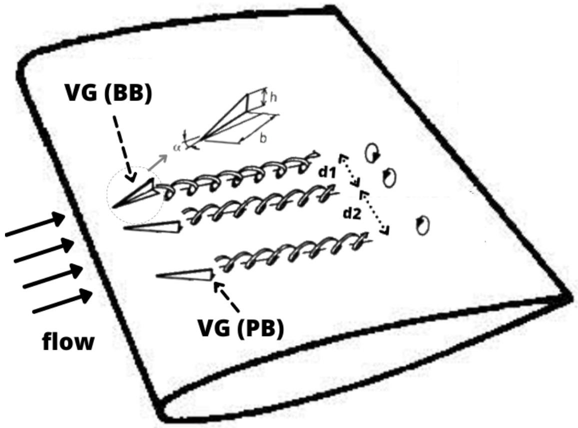

Figure 4.4: A sketch of one possible way to implement a vortex whip with delta-winglet vortex generators on the upper surface of a lifting wing. Not to scale. Image modified from Huisseune [30].

length b, and angle of attack α relative to the incoming flow. Suppose one VG is placed at 30° (this VG represents Papa Bear and would create the strongest vortices)—labeled in the drawing as the VG farthest right. Imposing the condition that $\Gamma_1 < \Gamma_2 < \Gamma_3$ and $\frac{\Gamma_2}{\Gamma_1} = \frac{\Gamma_3}{\Gamma_2} = 5.0$, the other two VGs would be placed at 6° and 1.2°, respectively, relative to the flow. The VG oriented at 1.2° creates Baby Bear, the weakest vortices. d_1 and d_2 in the figure have the same meaning as in our 2D simulations. Please note that Fig. 4.4 shows just one possibility of how we can implement a vortex whip.

Chapter 5

CONCLUSIONS

We have come a long way from where we started in Chapter 2 where we ran preliminary simulations to guide our intensive search of the 2D vortex whip parameter space. It has been a stressful and exhausting journey to get to this point, but truly exhilarating and gratifying nevertheless. After more than 25000 attempts, our persistence rewarded us with several significant contributions to the vortex whip problem as a whole. These findings will help drive future investigations into the vortex whip problem and its applications.

5.1 Summary

In summary, the significant contributions made by this work include:

1. Found the best combination of senses of rotation to use for a 2D vortex whip consisting of three vortices: (BB MB PB) = $(+--)$.

2. Found that it is more effective to vary the inter-separation distance between BB and MB (d_1) rather than the inter-separation distance between MB and PB (d_2). For the range of parameters investigated in this thesis, $\frac{d_1}{d_2} \approx 0.3$ appears to be close to optimal.

3. Found that the optimal configuration of a 2D vortex whip is sensitive to d_2, but the sensitivity is not a high one.

4. Found that for $1.1 \leq \frac{\Gamma_2}{\Gamma_1} = \frac{\Gamma_3}{\Gamma_2} \leq 3.0$, the performance of a vortex whip is optimal when $\frac{d_2}{H} < 1$.

5. Found that for $3.1 \leq \frac{\Gamma_2}{\Gamma_1} = \frac{\Gamma_3}{\Gamma_2} \leq 5.0$, the performance of a vortex whip is optimal when $\frac{d_2}{H} > 1$.

5.2 Future Work

There is still a lot of work that can be done to advance our understanding of how to optimize a vortex whip to help inhibit boundary layer separation. This section offers three suggestions for future work.

Recall that in this thesis, we only performed simulations where $\frac{\Gamma_2}{\Gamma_1} = \frac{\Gamma_3}{\Gamma_2}$. One possible way to extend this work is to consider the more general case $\frac{\Gamma_2}{\Gamma_1} \neq \frac{\Gamma_3}{\Gamma_2}$, while still keeping $\Gamma_1 < \Gamma_2 < \Gamma_3$. Looking into this more general case allows one to explore more of the parameter space, potentially unveiling new useful discoveries.

Another direction for future work is to proceed directly to the 3D vortex whip problem. This more involved problem will require the use of professional CFD software such as Ansys Fluent, Star-CCM+, or OpenFOAM, to name a few. Furthermore, the size of the mesh and computational domain must be fine enough to capture the physics—most likely in the millions for the number of cells required. A mesh of this scale would necessitate the use of a supercomputer to perform the computations. For the 3D case, the researcher considers many different configurations and arrangements of three VGs on a flat plate. The objective of this research is to find a near optimal configuration of vortex generators that will most effectively serve as a vortex whip in order to transfer high-momentum fluid effectively to the bottom of the boundary layer.

Finally, the third suggestion is to design and perform real experiments with an array of VGs placed in a controlled environment. The true test and validation of any numerical simulation is through experimentation, if possible. The significant findings reported in this dissertation can be used as a starting point for these experiments. In turn, these real experiments can confirm whether the results reported here are indeed valid or should be refined.

BIBLIOGRAPHY

[1] Taylor, H. D., "Summary Report on Vortex Generators United Aircraft," Research Department Report, R-05280-9, United Aircraft Corporation (1950).

[2] Schubauer, G.B. and Spangenberg, W. G., "Forced Mixing in Boundary Layers," J. Fluid Mech., Vol. 8, part 1, pp. 10-31 (1960).

[3] Pearcey, H. H., "Shock-Induced Separation and Its Prevention," Boundary Layer and Flow Control, (G.V. Lachmann, ed.) Vol. 2, pp. 1166-1344 (1961).

[4] Brown, Alan C, Nawrocki, H. Franz, and Paley, Peter N. "Subsonic Diffusers Designed Integrally with Vortex Generators." Journal of Aircraft 5, no. 3 (1968): 221-29.

[5] Lan, C. E., and Roskam, J., "Wing Stall," Airplane Aerodynamics and Performance, published by Roskam Aviation and Engineering Corporation, Ottawa, Kansas, 1980.

[6] Bragg, M. B, and Gregorek, G. M. "Experimental Study of Airfoil Performance with Vortex Generators." Journal of Aircraft 24, no. 5 (1987): 305-09.

[7] Rao, Dhanvada, and Kariya, Tsuyoshi. "Boundary Layer Submerged Vortex Generators for Separation Control - an exploratory study." AIAA 1st National Fluid Dynamics Conference, Cincinnati OH, 25 July 1988, AIAA Paper 88-3546.

[8] Lin, John. and Howard, Floyd. "Turbulent Flow Separation Control Through Passive Techniques." 2nd Shear Flow Conference, Tempe AZ, 13-16 March 1989, AIAA Paper 89-0976.

[9] Lin, John, Howard, Floyd, and Bushnell, Dennis. "Investigation of Several Passive and Active Methods for Turbulent Flow Separation Control." AIAA 21st Fluid Dynamics, Plasma Dynamic and Lasers Conference, Seattle WA, 18-20 June 1990, AIAA Paper 90-1598.

[10] Lin, John, Howard, Floyd, and Selby, Gregory. "Small Submerged Vortex Generators for Turbulent Flow Separation Control." Journal of Spacecraft and Rockets 27.5 (1990): 503-507.

[11] Lin, John, Selby, Gregory, and Howard, Floyd. “Exploratory Study of Vortex-Generating Devices for Turbulent Flow Separation Control.” 20th Aerospace Sciences Meeting, 7-10 January 1991, Reno NV, AIAA Paper 91-0042.

[12] Fiebig, Martin, Kallweit, Peter, Mitra, Nimai, and Tiggelbeck, Stefan. “Heat Transfer Enhancement and Drag by Longitudinal Vortex Generators in Channel Flow.” Experimental Thermal and Fluid Science 4, no. 1 (1991): 103-14.

[13] Tiggelbeck, St, Mitra, N.K, and Fiebig, M. “Experimental Investigations of Heat Transfer Enhancement and Flow Losses in a Channel with Double Rows of Longitudinal Vortex Generators.” International Journal of Heat and Mass Transfer 36, no. 9 (1993): 2327-337.

[14] Kerho, M, Hutcherson, S, Blackwelder, R. F, and Liebeck, R. H. “Vortex Generators Used to Control Laminar Separation Bubbles.” Journal of Aircraft 30, no. 3 (1993): 315-19.

[15] Barrett, R. M., “An experimental evaluation of smart tetrahedral vortex generators.” PhD dissertation. University of Kansas, 1993.

[16] Anderson, J. (1994). *Computational fluid dynamics: The basics with applications* (McGraw-Hill series in mechanical engineering). New York: McGraw-Hill.

[17] Lin, John, Robinson, Stephen, McGhee, Robert, and Valarezo, Walter. “Separation Control on High Lift Airfoils via Micro-Vortex Generators.” Journal of Aircraft 31.6 (1994): 1317-1323.

[18] Jacobi, A.M, and Shah, R.K. “Heat Transfer Surface Enhancement through the Use of Longitudinal Vortices: A Review of Recent Progress.” Experimental Thermal and Fluid Science 11, no. 3 (1995): 295-309.

[19] Klausmeyer, S. M, Papadakis, M., and Lin, J. C. A flow physics study of vortex generators on a multi-element airfoil. AIAA Paper 1996–0548.

[20] Lin, John. “Control of Turbulent Boundary-Layer Separation Using Micro-Vortex Generators.” AIAA 30th Fluid Dynamics Conference, Norfolk VA, 28 June - 18 July 1999, AIAA Paper 99-3404.

[21] Gentry, M.C, and Jacobi, A.M. “Heat Transfer Enhancement by Delta-wing Vortex Generators on a Flat Plate: Vortex Interactions with the Boundary Layer.” Experimental Thermal and Fluid Science 14, no. 3 (1997): 231-42.

[22] Fiebig, M. “Vortices, Generators and Heat Transfer.” Chemical Engineering Research & Design 76, no. 2 (1998): 108-23.

[23] Jenkins, Luther, Gorton, Susan, and Anders, Scott. “Flow Control Device Evaluation for An Internal Flow with An Adverse Pressure Gradient.” AIAA 40th Aerospace Sciences Meeting & Exhibit, Reno NV, 14-17 January 2002, AIAA Paper 2002-0266.

[24] Gentry, M. C, and Jacobi, A. M. “Heat Transfer Enhancement by Delta-Wing-Generated Tip Vortices in Flat-Plate and Developing Channel Flows.” Journal of Heat Transfer 124, no. 6 (2002): 1158-168.

[25] Godard, G, and Stanislas, M. “Control of a Decelerating Boundary Layer. Part 1: Optimization of Passive Vortex Generators.” Aerospace Science and Technology 10, no. 3 (2006): 181-91.

[26] Anderson, John D. *Fundamentals of Aerodynamics.* 4th ed. McGraw-Hill Series in Aeronautical and Aerospace Engineering. Boston: McGraw-Hill Higher Education, 2007.

[27] Ma, H. D. and Cui, E. J. “Drag prediction and reduction for civil transportation.” Mechanics in Engineering. 2007, 29(2): 1–8.

[28] Sohankar, A. “Heat Transfer Augmentation in a Rectangular Channel with a Vee-shaped Vortex Generator.” The International Journal of Heat and Fluid Flow 28, no. 2 (2007): 306-17.

[29] He, J, Liu, L, and Jacobi, A. M. “Air-Side Heat-Transfer Enhancement by a New Winglet-Type Vortex Generator Array in a Plain-Fin Round-Tube Heat Exchanger.” Journal of Heat Transfer 132, no. 7 (2010): 071801.

[30] Huisseune, Henk, C. T’joen, P. D. Jaeger, Bernd Ameel, S. D. Schampheleire and M. D. Paepe. “Influence of the geometry on the thermohydraulics of a compound heat exchanger consisting of louvered fins and delta winglets.” (2012).

[31] Abdollahi, Azita, and Shams, Mehrzad. “Optimization of Shape and Angle of Attack of Winglet Vortex Generator in a Rectangular Channel for Heat Transfer Enhancement.” Applied Thermal Engineering 81 (2015): 376-87.

[32] Salviano, Leandro O, Dezan, Daniel J, and Yanagihara, Jurandir I. “Optimization of Winglet-type Vortex Generator Positions and Angles in Plate-fin Compact Heat Exchanger: Response Surface Methodology and Direct Optimization.” International Journal of Heat and Mass Transfer 82 (2015): 373-87.

[33] Jiménez, Javier, and Moin, Parviz. “The Minimal Flow Unit in Near-wall Turbulence.” Journal of Fluid Mechanics 225 (1991): 213-40.

[34] Ashilf, P. R., Fulker, J. L., and Hackett, K. C. Research at DERA on sub boundary layer vortex generators (SBVGs). AIAA Paper 2001–0887.

[35] Marshall, J.S. “Cross-Stream Vorticity Field Induced by Streamwise Vortices in Unbounded and Wall-Bounded Shear Flows.” Theoretical and Computational Fluid Dynamics 16, no. 3 (2003): 231-47.

[36] Wendt, Bruce J. “Parametric Study of Vortices Shed from Airfoil Vortex Generators.” AIAA Journal 42, no. 11 (2004): 2185-195.

[37] Scott, Jeff. “Nacelle Vortex Generator.” *Aerospaceweb.org*, 18 December 2005, http://www.aerospaceweb.org/question/aerodynamics/q0255.shtml.

[38] Gardarin, Benoit, Jacquin, Laurent, and Geffroy, Philippe. (2008). “Flow Separation Control With Vortex Generators.” 4th AIAA Flow Control Conference.

[39] Chen, Y. C., Liu, H., Zhang, B. Q., and Zhu, Z. Q. “A review on drag reduction study and application for large aircraft.” The Application and Development of CFD in Large Civil Aircraft, Shanghai Jiao Tong University Press, 2009, 32–47.

[40] Seshagiri, Amith, Cooper, Evan, and Traub, Lance W. “Effects of Vortex Generators on an Airfoil at Low Reynolds Numbers.” Journal of Aircraft 46, no. 1 (2009): 116-22.

[41] Fox, R., & McDonald, Alan T. (2011). *Introduction to fluid mechanics (8th ed.)*. New York: J. Wiley.

[42] Lu, Frank K, Li, Qin, and Liu, Chaoqun. “Microvortex Generators in High-speed Flow.” Progress in Aerospace Sciences 53 (2012): 30-45.

[43] Serakawi, A. R, and Ahmad, K. A. “Experimental Study of Half-Delta Wing Vortex Generator for Flow Separation Control.” Journal of Aircraft 49, no. 1 (2012): 76-81.

[44] Ahmed, H.E, Mohammed, H.A, and Yusoff, M.Z. “An Overview on Heat Transfer Augmentation Using Vortex Generators and Nanofluids: Approaches and Applications.” Renewable & Sustainable Energy Reviews 16, no. 8 (2012): 5951-993.

[45] Jukes, Timothy N, and Choi, Kwing-So. “On the Formation of Streamwise Vortices by Plasma Vortex Generators.” Journal of Fluid Mechanics 733 (2013): 370-93.

[46] Juniper, Matthew. "Delaying Boundary Layer Separation." *LearnFluidMechanics.org*, May 2015, http://learnfluidmechanics.org.

[47] Leweke, Thomas, Le Dizes, Stephane, and Williamson, Charles H.K. "Dynamics and Instabilities of Vortex Pairs." Annual Review of Fluid Mechanics 48, no. 1 (2016): 507-41.

[48] Skullong, Sompol, Promvonge, Pongjet, Thianpong, Chinaruk, and Jayranaiwachira, Nuthvipa. "Thermal Behaviors in a round Tube Equipped with Quadruple Perforated-delta-winglet Pairs." Applied Thermal Engineering 115 (2017): 229-43.

[49] Cengel, Yunus A., and Cimbala, John M. *Fluid Mechanics: Fundamentals and Applications.* Fourth ed. New York, NY: McGraw-Hill Education, 2018.

[50] Barba, Lorena A., Mesnard, Olivier (2019). Aero Python: classical aerodynamics of potential flow using Python. Journal of Open Source Education, 2(15), 45, https://doi.org/10.21105/jose.00045

[51] Wang, J., & Feng, Lihao. (2019). *Flow control techniques and applications* (Cambridge aerospace series ; 46). Cambridge, United Kingdom ; New York, NY, USA: Cambridge University Press.